Spring 2023

Additive Manufacturing for Phase Change Thermal Energy Storage and Management

Thomas B. Freeman
Embry-Riddle Aeronautical University, freemat1@my.erau.edu

Additive Manufacturing for Phase Change Thermal Energy Storage and Management

by

Thomas B. Freeman

A Dissertation Submitted to the College of Engineering Department of Mechanical Engineering in Partial Fulfillment of the Requirements for the Degree of Doctor of Philosophy in Mechanical Engineering

Embry-Riddle Aeronautical University

Daytona Beach, Florida

May 2023

Additive Manufacturing for Phase Change Thermal Energy Storage and Management

by

Thomas B. Freeman

This dissertation was prepared under the direction of the candidate's Dissertation Committee Chair, Dr. Sandra K.S. Boetcher, Professor, Daytona Beach Campus, and Dissertation Committee Members Dr. Rafael M. Rodriguez, Professor, Daytona Beach Campus, Dr. Mark A. Ricklick, Professor, Daytona Beach Campus, Dr. Eduardo A. Divo, Professor, Daytona Beach Campus, and Dr. Patrick N. Currier, Professor, Daytona Beach Campus, and has been approved by the Dissertation Committee. It was submitted to the Department of Mechanical Engineering in partial fulfillment of the requirements for the degree of Doctor of Philosophy in Mechanical Engineering

Dissertation Review Committee:

_____

Sandra Boetcher, Ph.D.
Committee Chair

_____ _____

Rafael Rodriguez, Ph.D.
Committee Member

Mark Ricklick, Ph.D.
Committee Member

_____ _____

Eduardo Divo, Ph.D.
Committee Member

Patrick Currier, Ph.D.
Committee Member

_____ _____

Eric Coyle, Ph.D.
Ph.D. Program Chair,
Mechanical Engineering

Patrick Currier, Ph.D.
Department Chair,
Mechanical Engineering

_____ _____

James Gregory, Ph.D.
Dean, College of Engineering

Lon Moeller, J.D.
Senior Vice President for Academic Affairs and Provost

ABSTRACT

Researcher: Thomas B. Freeman

Title: Additive Manufacturing for Phase Change Thermal Energy Storage and Management

Institution: Embry-Riddle Aeronautical University

Degree: Doctor of Philosophy in Mechanical Engineering

Year: 2023

Phase change materials can enhance the performance of energy systems by time shifting or reducing peak thermal loads. Certain electronic devices such as batteries, laser systems, or electric vehicle power electronics are highly transient and require pulse heat dissipation. Heat sinks, or thermal management devices made of a phase change material can absorb large heat spikes while maintaining a constant temperature. Additive manufacturing techniques hold tremendous potential to enable co-optimization of material properties and device geometry, while potentially reducing material waste and manufacturing time. Recently, a few efforts have emerged that employ additive manufacturing techniques to integrate a phase change material thermal energy storage into geometrically complex designs for advanced thermal management. This work contributes to the emerging field of research by reporting on the production of composite thermoplastic/phase change material filaments for fused filament fabrication 3D-printing, and their subsequent use to 3D-print advanced heat exchange topologies with intricate geometric features.

TABLE OF CONTENTS

LIST OF FIGURES

LIST OF TABLES

NOMENCLATURE

$\bar{c_p}$	Average Specific Heat [J/kgK]
$\bar{k}$	Average Thermal Conductivity [W/mK]
$\bar{Nu}$	Average Nusselt Number
$\dot{m}$	Mass Flow Rate [kg/sec]
$\dot{Q}$	Power [W]
ρ	Density [kg/m^3]
c_p	Specific Heat [J/kgK]
D_h	Hydraulic Diameter [m]
H	Height [m]
h	Enthalpy [J/kg]
h_{sl}	Latent Heat of Fusion [J/kg]
h_{sl}	Latent Heat of Fusion [kJ/kg]
htc	Heat Transfer Coefficient [W/m^{2}K]
k	Thermal Conductivity [W/mK]
k	Thermal Conductivity [W/mK]
L	Length [m]
Nu	Nusselt Number
P	Pressure [Pa]
q''	Heat Flux [W/m^2]

R Resistance [K/W]

T Temperature [K]

t Thickness [m]

v Velocity [m/s]

W Width [m]

1 Introduction

There is an urgent need to decarbonize our energy systems to mitigate the effects of climate change [1]. Doing so will require the rapid deployment of clean energy generation such as solar and wind [2]. However, the inherent intermittency of such sources requires co-deployment of scalable, affordable, and sustainable energy storage technologies [3]. Over the years, several methods to store large quantities of energy have been developed, each at its own level of readiness, and set of advantages and drawbacks [4–7]. Of these options, thermal energy storage (TES) systems are of particular interest due to their potential for low cost and long lifetime. As shown in Figure 1.1, materials used for TES can be classified into three categories: materials that store heat sensibly, materials that store heat via a latent phase transformation, and materials that store heat via a thermochemical reaction. Many authors have presented comparisons as well as advantages and disadvantages of sensible [8], latent [9, 10], and thermochemical energy storage [11–13].

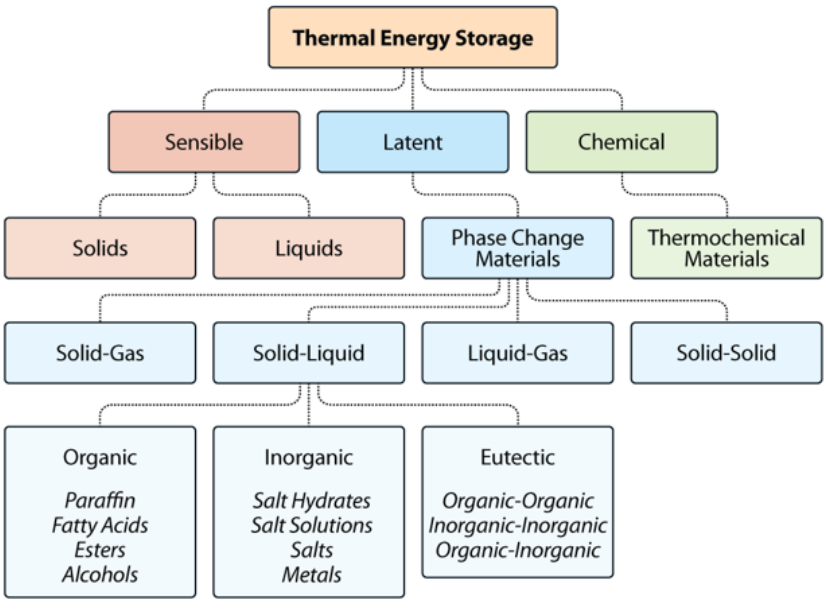

Figure 1.1 Characterization of thermal energy storage materials.

Latent heat storage materials, also known as phase-change materials (PCMs)

are a class of TES materials that have great potential for a variety of thermal management applications because of their ability to store latent heat over a near constant temperature [14]. In these materials, heat can be stored using a variety of phase transitions, including gas-liquid, solid-gas, solid-solid, and solid-liquid. PCMs involving a gas phase are generally not of great interest to the thermal energy storage community, as they suffer from very low energy density because the gaseous phase occupying a large volume[15]. Similarly, solid-solid phase transitions typically occur as a material undergoes a transition from one crystalline phase (polymorph) to another, or from a crystalline to amorphous phase, and consequently are also limited in energy density [16]. As such, solid-liquid PCMs are most compelling in terms of energy density and will be the primary focus of this review.

The effectiveness of a PCM is defined by its energy and power density—the total available storage capacity (kWh) and how fast it can be accessed (kW). These are influenced by both material properties and device geometry; however, prior efforts have primarily focused on improving material properties, namely, maximizing latent heat of fusion and increasing thermal conductivity [17–19]. The latter is often at the expense of the former, as most efforts attempt to improve thermal conductivity by combining a thermally conductive material with the PCM to create a composite. The thermally conductive material does not participate in phase change, and thus displaces PCM volume. Advanced manufacturing techniques hold tremendous potential to enable co-optimization of material properties and device geometry, while potentially reducing material waste and manufacturing time. There is an emerging body of research focused on additive manufacturing of PCM composites and devices for TES. The state-of-the art of solid-liquid PCMs with transition temperature between -50 °C to 400 °C, spanning a wide range of potential applications from refrigeration to concentrated solar power plants. Various classes of PCMs, their material properties, advantages/disadvantages are reviewed, and an

overview of the application field of use for these materials is presented. Secondly, a comprehensive review of recent additive manufacturing (AM) enabled advances in latent heat TES, which has the potential to transform the field by enabling co-optimization of material properties and device geometry. Lastly, a forward-looking perspective on potential future directions of advanced materials and manufacturing of PCM composites for TES and thermal management is provided.

1.1 Review of Relevant Literature

1.1.1 Fundamentals of PCMs

Solid-liquid PCMs are either organic, inorganic, or a eutectic (combination) of two organic or inorganic PCMs. Organic PCMs include paraffins [20], sugar alcohols [21], and fatty acids along with their alcohol and ester derivatives [22]. Inorganic PCMs include salts [23], salt hydrates [24], and metals [25]. Eutectics are typically combinations of two or more organic and/or inorganic PCMs [26, 27]. Inorganic PCMs generally have higher energy density/specific energy, higher thermal conductivity, lower cost (except for metals), and are naturally occurring (except for metals). However, they are often corrosive, and tend to suffer from materials challenges such as supercooling [28, 29] and phase separation [29], which limit reliability in end-use. Except for sugar alcohols, organic PCMs do not supercool. They are also usually single-component materials which are not prone to phase separation. However, they are often petroleum or bio-derived which leads to higher costs and not bio-friendly. They typically have lower energy density/specific energy and are often flammable. In general, organic PCMs are easier to incorporate into AM workflows because they are easier to microencapsulate, are stable at higher temperatures (which is required by some AM processes), are not corrosive to metals, and do not run a risk of phase separating during AM processing. Some advantages and disadvantages of organic versus inorganic PCMs are shown in Table 1.1. For many applications, the PCM transition temperature may be the first/most important PCM

selection criteria as some PCM types do not have a wide range of available transition temperatures. Salt hydrates, for example, are typically not available above transition temperatures of 100 °C. Sugar alcohols are typically not available below transition temperatures of 80 °C.

Table 1.1 Advantages and disadvantages of organic and inorganic PCMs

	Organic	Inorganic
Advantages	- Not corrosive - Little-to-no supercooling - Chemically and thermally stable - Wide range of transition temperature	- High energy density - Higher thermal conductivity - Lower cost - Non-flammable - Naturally occurring
Disadvantages	- Low energy density - Low thermal conductivity - Often flammable - Often petroleum based	- Prone to supercooling - Prone to phase separation - Often corrosive

1.1.2 Organic PCMs

This section covers a brief overview of the various organic PCMs within paraffins and non-paraffins (esters, sugar alcohols, fatty acids, etc.). The most common characteristics of each of these groups will be discussed, along with a comprehensive list of the phase transition temperatures, latent heats, and energy densities of the specific materials. Organic PCMs lend themselves well to processing via AM because they are available in microencapsulated forms, are stable at higher temperatures relative to salt-hydrates and salt-water solutions, and do not phase separate.

Paraffins

Paraffin waxes consist of a mixture of linear n-alkanes [CH3-(CH2)n-CH3] and are commonly defined by the number of carbon atoms in a single straight chain. The melt temperature and latent heat typically increase as the length of the chain increases. Paraffins are a popular choice for TES due to the wide range of transition temperatures in this sub-category. Other benefits of paraffins include predictable and repeatable phase transition, non-corrosiveness, congruent melting, and

Table 1.2 Paraffin PCMs for TES applications

Name	Molecular Formula	Melt Temperature [°C]	Latent Heat of Fusion [kJ/kg]	Energy Density [kWh/m3]	Ref
n-Tetradecane	$C_{14}H_{30}$	5.5	228	48.13	[33, 34]
n-Pentadecane	$C_{15}H_{32}$	10	205	43.79	[34]
n-Hexadecane	$C_{16}H_{34}$	16.7	237	50.89	[34, 35]
n-Heptadecane	$C_{17}H_{36}$	21.7	213	46.03	[36]
n-Octadecane	$C_{18}H_{38}$	28.0	244	52.66	[35, 36]
n-Nonadecane	$C_{19}H_{40}$	32.0	159	34.72	[37]
n-Eicosane	$C_{20}H_{42}$	36.7	246	53.92	[35]
n-Henicosane	$C_{21}H_{44}$	40.2	200	44.00	[38]
n-Docosane	$C_{22}H_{46}$	44.0	249	54.92	[39, 40]
n-Tricosane	$C_{23}H_{48}$	47.5	232	50.20	[41]
n-Tetracosane	$C_{24}H_{50}$	50.6	255	56.60	[42, 43]
n-Pentacosane	$C_{25}H_{52}$	49.4	238	52.96	[44]
n-Hexacosane	$C_{26}H_{54}$	56.3	256	55.32	[39, 45, 46]
n-Heptacosane	$C_{27}H_{56}$	58.8	236	51.13	[47]
n-Octacosane	$C_{28}H_{58}$	61.6	253	56.64	[38, 48, 49]
n-Dotriacontane	$C_{32}H_{66}$	69.5	170	38.34	[50]
n-Tritriacontane	$C_{33}H_{68}$	73.9	268	61.04	[51, 52]

strong nucleating properties. Downsides of paraffins include low thermal conductivity, incompatibility with some types of plastic containers, high volume change during phase transition, volatility, and flammability [30–32]. A list of commonly used paraffins is shown in Table 1.2.

Non-Paraffins

Non-paraffins are a broad category of organic phase change materials that do not inherently share the same properties, unlike the paraffin waxes. Non-paraffins consist of various materials including esters, alcohols, glycols, and fatty acids. Non-paraffins are known for their sharp phase transitions, reliable and repeatable melting and freezing, low supercooling (except for sugar alcohols), and high latent heats of fusion. Downsides of non-paraffins include low thermal conductivity, low flash points, instability at high temperatures, high flammability, toxicity, mild corrosiveness, and high cost [53–55]. A list of commonly used organic non-paraffin PCMs can be seen in Table 1.3.

Table 1.3 Organic Non-Paraffins for TES applications

Name	Molecular Formula	Melt Temperature [°C]	Latent Heat of Fusion [kJ/kg]	Energy Density [kWh/m^3]	Ref
Alcohols					
Glycerin	C3H8O3	17.9	198	69.30	[56]
Lauryl Alcohol	C12H26O	24	215	49.63	[57–60]
Myristyl Alcohol	C14H30O	38	151	34.56	[61]
Cetyl Alcohol	C16H34O	49.3	141	31.76	[60, 62–64]
Sugar Alcohols					
Xylitol	HO(CHOH)3OH	92	233	98.38	[21]
Sorbitol	C6H14O6	95.6	167	69.12	[21]
Erythritol	HO(CHOH)2OH	118.7	333	134.17	[21]
Mannitol	C6H14O6	165.6	284	119.56	[21]
Dulcitol	C6H14O6	187.2	330	121.33	[21]
Inositol	C6H12O6	224	249	134.72	[21]
Polyethylene Glycols					
PEG 400	H(OC2H4)nOH	6	84	26.32	[54, 65–67]
PEG 600	H(OC2H4)nOH	21	120	37.67	[67]
PEG 1,000	H(OC2H4)nOH	39	152	50.67	[67]
PEG 2,000	H(OC2H4)nOH	51	165	55.46	[68]
PEG 10,000	H(OC2H4)nOH	67	197	65.67	[69]
Esters					
Methyl Palmitate	C17H34O2	29	205	48.52	[70–72]
Tristearin	(C17H35COO)3C3H5	56	191	45.73	[73]
Fatty Acids					
Formic Acid	HCOOH	7.8	247	83.71	[74]
Acetic Acid	CH3COOH	16.7	184	53.67	[75]
Caprylic Acid	CH(CH)COOH	16.3	149	37.66	[57, 62]
Capric Acid	CH3(CH2)8·COOH	23	152	37.70	[64, 76, 77]
Lauric Acid	CH3(CH2)10·COOH	49	178	43.51	[41, 59, 61, 70, 77–79]
Myristic Acid	CH3(CH2)12·COOH	58	199	47.65	[59, 76–78]
Palmitic Acid	CH3(CH2)14·COOH	55	163	38.62	[41, 59, 80–82]
Stearic Acid	CH3(CH2)16·COOH	69.4	199	52.02	[77, 79, 83–86]
Others					
Phenol	C6H5OH	41	120	35.67	[87]
Camphene	C10H16	50	238	55.67	[80, 83]
Naphthalene	C10H8	56.7	103	32.62	[88, 89]
Bees Wax	C15H31COOC30H61	61.8	177	47.45	[90]
Glycolic Acid	HOCH2CO2H	63	109	45.11	[91]
Azobenzene	C12H10N2	67.1	121	36.64	[92]
Acrylic Acid	C3H4O2	68	115	33.54	[91]
Phenylacetic Acid	C8H8O2	76.7	102	30.60	[93]
Acetamide	CH3CONH2	81	241	77.66	[94, 95]
Glutaric Acid	C5H8O4	97.5	156	61.92	[96]
Acetanilide	C8H9NO	118.9	222	75.23	[84, 97, 98]
Benzoic Acid	C7H6O2	121.7	143	50.45	[88, 97]
Stilbene	C14H12	124	167	45.04	[92]
Benzamide	C7H7NO	127	169	62.91	[86, 99]

1.1.3 Inorganic PCMs

This section provides an overview of inorganic PCMs, including salts, salt hydrates, salt-water solutions, and metals. The commonly known characteristics of each group will be discussed, along with a comprehensive list of the phase transition temperatures, latent heats, and energy densities of the specific materials. With the exception of metallic PCMs, inorganic PCMs are challenging to incorporate into AM workflows for several reasons. Salt based PCMs are corrosive to many metals and can damage AM processing equipment. Also, many AM approaches require processing at elevated temperatures, which is incompatible with salt-hydrate and salt-water PCMs, as elevated temperatures can cause some of the water in the PCMs to evaporate, altering the PCM composition and increasing the risk of phase separation. Inorganic PCMs are also challenging to microencapsulate. At the time of writing, the authors are not aware of any efforts in the literature where inorganic PCMs are processed using AM techniques.

Salts

Salts such as nitrates and chlorides are being widely investigated for their use in high temperature thermal energy storage applications (>250 °C). In terms of usable PCMs at high temperatures, salts and metals are the few that can be used reliably. Some of the benefits of salts include being cost-effective and having a very high latent heat of fusion. The disadvantages of salts are their corrosiveness, supercooling , low thermal conductivity, and poor thermal stability [100]. Research is being focused on improving salts as a thermal energy storage material, since with high temperature applications the amount of PCMs that are stable becomes limited to only salts [101–104]. A list of salts used for thermal energy storage applications (<400 °C) can be seen in Table 1.4.

Table 1.4 Salts for TES applications

Name	Molecular Formula	Melt Temperature [°C]	Latent Heat of Fusion [kJ/kg]	Energy Density [kWh/m^3]	Ref
Aluminum Chloride	AlCl3	192	280	192.89	[105]
Lithium Nitrate	LiNO3	250	370	244.61	[105]
Sodium Nitrate	NaNO3	307	172	107.98	[105]
Potassium Nitrate	KNO3	333	266	155.91	[105]
Sodium Peroxide	Na2O2	360	314	244.22	[105]
Potassium Hydroxide	KOH	380	150	88.33	[105]

Salt Hydrates

Salt hydrates are inorganic compounds containing salt and water molecules in an explicit ratio to form a defined crystal structure [29]. Salt hydrates are a popular PCM for a wide range of thermal energy storage applications. The actual phase change transition for salt hydrates is not a traditional solid-liquid transition. A salt hydrate goes between a hydrated and dehydrated state of the salt, but this process resembles a melting and freezing process thermodynamically. During a melting/freezing process, the salt will release stored water molecules becoming a salt hydrate with fewer moles of water,

$AB \cdot nH_2O \leftrightarrow AB \cdot mH_2O + (n-m)H_2O$

or in the anhydrous form of the salt

$AB \cdot nH_2O \leftrightarrow AB + nH_2O$

Salt hydrates generally suffer from poor nucleation properties, resulting in supercooling (or subcooling) [24]. This means that upon cooling to release stored thermal energy, a salt hydrate may not nucleate and crystallize until it is supercooled well below its phase change temperature, which causes problems in practical applications. The fundamentals of the kinetics of crystal nucleation are well described in prior literature [106–108]. Phase segregation is another phenomenon plaguing salt hydrate PCMs where salt and water can separate after melt/freeze cycling, gravity acts on density differences and causes the two phases to physically separate, rendering the PCM ineffective[109–112]. Whether a given salt hydrate will suffer from

Table 1.5 Salts hydrates for TES applications

Name	Molecular Formula	Melt Temperature [°C]	Latent Heat of Fusion [kJ/kg]	Energy Density [kWh/m^3]	Ref
Lithium Chlorate Trihydrate	LiClO3·3H2O	8	253	129.31	[113]
Potassium Fluoride Tetrahydrate	KF·4H2O	19	231	93.04	[114, 115]
Manganese (II) Nitrate Hexahydrate	Mn(NO3)2·6H2O	25.3	126	56.00	[116]
Calcium Chloride Hexahydrate	CaCl2·6H2O	28-30	190-200	97.50	[114–116]
Lithium Nitrate Trihydrate	LiNO3·3H2O	30	256	104.04	[116]
Sodium Sulfate Decahydrate	Na2SO4·10H2O	34	256	105.96	[116]
Sodium Carbonate Decahydrate	Na2CO3·10H2O	33	247	98.80	[113]
Sodium Acetate Trihydrate	NaCH3COO·3H2O	55.6-56.5	237-243	96.67	[117]
Calcium Bromide Hexahydrate	CaBr2·6H2O	34	116	48.98	[115]
Disodium Hydrogen Phosphate Dodecahydrate	Na2HPO4·12H2O	35-45	280	118.22	[115]
Zinc Nitrate Tetrahydrate	Zn(NO3)2·4H2O	45.5			[107]
Zinc Nitrate Dihydrate	Zn(NO3)2·2H2O	54			[107]
Sodium Thiosulfate Pentahydrate	Na2S2O3·5H2O	48-55	201	97.15	[115]
Cadmium Nitrate Tetrahydrate	Cd(NO3)2·4H2O	59.5			[113]
Sodium Tetraborate Decahydrate	Na2B4O7·10H2O	68.1			[113]
Sodium Phosphate Dodecahydrate	NaPO4·12H2O	69			[113]
Barium Hydroxide Octahydrate	Ba(OH)2·8H2O	78	266	161.08	[113]
Magnesium Nitrate Hexahydrate	Mg(NO3)2·6H2O	89.3	150	68.17	[113]

phase segregation depends on its phase diagram and whether it melts congruently, semi-congruently, or incongruently. This is explained in detail in [107]. Despite these downsides, salt hydrates have several advantages including high energy density (energy per unit volume), higher thermal conductivity (almost double that of organic PCMs), lower cost (relative to organic PCMs), non-flammability, and small volume changes during melt/freezing. A table of commonly used salt hydrates can be seen in Table 1.5.

Salt-Water Solutions

Salt-water solutions are a mixture of salt and water that results in a PCM with phase transition temperatures below 0 °C, which makes them a prime candidate for refrigeration applications [30, 118]. Salt-water solutions are inherently similar to salt-hydrates and share many advantages and disadvantages. The advantages include the high energy density, lower cost, and non-flammability. The disadvantages include phase separation, subcooling, and high corrosiveness [118]. A list of salt-water solutions can be found in Table 1.6.

Metals

Low-temperature metals (<400 °C) and metal alloys can be used as PCMs; however, they are not a popular choice for thermal storage applications due to two

Table 1.6 Salt-water solutions for low temperature TES application

Name	Molecular Formula	Melt Temperature [°C]	Latent Heat of Fusion [kJ/kg]	Energy Density [kWh/m^3]	Ref
Aluminum Nitrate + H2O	30.5% Al(NO3)3 + 69.5% H2O	-30.6	131.5	44.55	[119, 120]
Ammonium Fluoride + H2O	32.3% NH4F + 67.7% H2O	-28.1	199.1	55.48	[119]
Potassium Fluoride + H2O	21.5% KF + 78.5% H2O	-21.6	225.2	82.46	[119]
Sodium Chloride + H2O	22.4% NaCl + 77.6% H2O	-21.2	222	77.69	[120]
Ammonium Chloride + H2O	21.5% NH4Cl + 78.5% H2O	-16	289	89.43	[120]
Ammonium Sulfate + H2O	39.7% (NH4)SO4 + 60.3% H2O	-18.5	269	97.56	[119]
Dipotassium phosphate + H2O	36.8% K2HPO4 + 63.2% H2O	-13.5	189	80.32	[119]
Barium Chloride + H2O	22.1% BaCl2 + 77.9% H2O	-7.7	102	46.24	[120]
Zinc Sulfate + H2O	27.2% ZnSO4 + 72.8% H2O	-6.5	208	97.7	[120]
Magnesium Sulfate + H2O	18.63% MgSO4 + 81.37% H2O	-4.8	84.96	30.9	[120]
Sodium Fluoride + H2O	3.9% NaF + 96.1% H2O	-3.5	309.2	91.11	[120]
Sodium Carbonate + H2O	5.9% Na2CO3 + 94.1% H2O	-2.1	281	85.15	[119]
Potassium Sulfate + H2O	6.49% K2SO4 + 93.51% H2O	-1.55	268.8	82.71	[120]

main reasons: low latent heat of fusion [121] and high cost. This means that any device having the same thermal capacity will be considerably heavier and more expensive when compared to other popular PCMs (paraffins and salt hydrates). If weight is not a concern, metal PCMs leverage their much higher densities to have a competitive energy density (energy per unit volume). Metal PCMs also have a naturally high thermal conductivity compared to alternative materials. A list of metal PCMs and metal alloys can be seen in Table 1.7.

1.1.4 Eutectic Mixtures

Eutectics involve the homogenous mixing of multiple PCMs that melts and solidifies at a single temperature that is lower than the melting point of the base constituents [26, 100, 129, 130]. This combining of PCMs requires precise control of the relative concentration of each constituent PCM to achieve congruent melting of a proper eutectic. Without proper mixing ratios, the mixture will segregate during cycling and fall out of eutectic [9, 53]. Eutectic mixtures have been explored for organic-organic, inorganic-inorganic, and in some cases inorganic-organic PCMs [131]. A list of various organic-organic and inorganic-inorganic eutectic mixtures can be seen in Table 1.8 and Table 1.9, respectively.

1.1.5 Summary of PCM Types

Figure 1.2 shows the volumetric energy density and latent heat of the PCMs reported in Tables 2-9 plotted against their transition temperature. Salts have high

Table 1.7 Metlas/Metal alloys for TES applications

Metal/Metal Alloy	Melt Temperature [°C]	Latent Heat of Fusion [kJ/kg]	Energy Density [kWh/m^3]	Ref
73.5% Ga – 15.4% In – 11.1% Sn	10.6	69	119.5	[121, 122]
78.4% Ga – 14.9% In – 6.7% Sn	10.9	71.2	121.98	[121, 122]
83.5% Ga – 16.5% In	15	71.7	121.34	[121, 122]
91.6% Ga – 8.4% Sn	19.8	78.3	131.02	[121, 122]
95% Ga – 5% Sn	19.9	79.2	131.49	[121, 122]
97.9% Ga – 2.1% Al	26.5	82.6	133.99	[121, 122]
Cesium (Cs)	28.7	16.4	8.18	[121, 123]
Gallium (Ga)	29.8	80.2	131.59	[121, 123]
Rubidium (Rb)	38.9	25.7	10.49	[121, 123]
44.7% Bi – 22.6% Pb – 19.1% In – 8.3% Sn – 5.3% Cd	47	36.8	93.64	[121, 123]
35.5% Bi – 64.5% In	54.1	30.8	68.53	[121, 122]
49% Bi – 21% In – 18% Pb – 12% Sn	58	28.9	72.33	[121, 123]
38.7% Bi – 16.7% Sn – 14.4% Pb – 30.2% In	58.3	29	70.54	[121, 122]
32% Bi – 51.2% In – 16.8% Sn	60.8	25.4	56.15	[121, 124]
41.8% Bi – 58.2% In	61.4	29.9	67.97	[121, 124]
Potassium (K)	63.2	59.6	10.99	[121, 123]
50% Bi – 26.7% Pb – 13.3% Sn – 10% Cd	70	39.8	105.91	[121, 123]
41.6% Bi – 19.4% Sn – 23.2% Pb – 15.8% Cd	71.7	24.5	64.48	[121, 122]
21.8% Bi – 78.2% In	73.1	22.5	47.7	[121, 122]
38.5% Bi – 22.2% Sn – 25.3% Pb – 14% In	75	25.4	65.13	[121, 122]
40.5% Bi – 28.5% Sn – 16.3% Pb – 14.7% In	75.7	21.7	53.76	[121, 122]
53.8% Bi – 27% In – 19.2% Sn	76.6	32.6	77.58	[121, 125]
42.5% Bi – 35.2% In – 22.3% Sn	79.2	36.9	84.7	[121, 122]
9.5% Sn – 56% Bi – 34.5% Pb	90.8	19.5	54.55	[121, 126]
71.2% Bi – 28.8% Pb	94.9	29	82.34	[121, 122]
52% Bi – 30% Pb – 18% Sn	96	34.7	92.53	[121, 123]
Sodium (Na)	97.8	113.2	29.15	[121, 123]
55% Bi – 43% Pb – 2% Zn	127	20.4	58.83	[121, 126]
48% Sn – 50% Bi – 2% Zn	135	47.6	112.94	[121, 126]
58% Bi – 42% Sn	138	44.8	106.52	[121, 123]
Indium (In)	157	28.6	55.85	[121, 123]
73.5% Sn – 22% Pb – 4.5% Zn	172	59.8	135.72	[121, 126]
Lithium (Li)	186	433.8	62.06	[121, 123]
91% Sn – 9% Zn	199	32.5	65.63	[121, 123]
Tin (Sn)	232	60.5	122.68	[121, 123]
Bismuth (Bi)	271	53.3	144.95	[121, 123]
Lead (Pb)	327	23	68.11	[127]
Cadmium (Cd)	321	55.2	122.61	[128]

Table 1.8 Organic-Organic eutectic mixtures for TES applications

Name	Mixture Formula	Melt Temperature [°C]	Latent Heat of Fusion [kJ/kg]	Energy Density [kWh/m^3]	Ref
85% Caprylic Acid – 15% Cetyl Alcohol	85% CH(CH)COH – 15% CH3(CH2)15OH	10	154	38.29	[62]
60% Camphene – 40% Stearic Acid	60% C10H16 – 40% CH3(CH2)16·COOH	3.5	156	38.2	[83]
54.9% Erythritol – 45.1% Urea	54.9% C4H10O4 – 45.1% CO(NH2)2	81.1	248	95.85	[132]
50% Camphene – 50% Palmitic Acid	50% C10H16 – 50% CH3(CH2)14·COOH	70.9	210	49.44	[80]
66% Lauric Acid – 34% Myristic Acid	66% CH3(CH2)10·COOH – 34% CH3(CH2)12·COOH	34.2	167	40.54	[78]
29% Lauric Acid – 71% Lauryl Alcohol	29% CH3(CH2)10·COOH – 71% C12H26O	17	175	41.09	[59]
17% Myristic Acid – 83% Lauryl Alcohol	17% CH3(CH2)12·COOH – 83% C12H26O	18.4	181	42.05	[59]
10% Palmitic Acid – 90% Lauryl Alcohol	10% CH3(CH2)14·COOH – 90% C12H26O	20.1	191	44.21	[59]
75.7% Stearic Acid – 24.3% Benzamide	75.7% CH3(CH2)16·COOH – 24.3% C7H7NO	65.9	200	57.66	[86]
46.2% Stearic Acid – 53.8% Hexanamide	46.2% CH3(CH2)16·COOH – 53.8% C6H13NO	58	177	45.18	[85]
81% Stearic Acid – 19% Acetanilide	81% CH3(CH2)16·COOH – 19% C8H9NO	69.3	220	60.75	[84]
70% Benzoic Acid – 30% Acetanilide	70% C7H6O2 – 30% C8H9NO	75.6	194	67.63	[97]
40% Lauric Acid – 60% Methyl Palmitate	40% CH3(CH2)10·COOH – 60% CH(CH)COOH	25.6	205	49.09	[70]
70% Capric Acid – 30% Cetyl Alcohol	70% CH3(CH2)8·COOH – 30% CH3(CH2)15OH	22.9	145	34.98	[64]
67% Capric Acid – 33% Lauric Acid	67% CH3(CH2)8·COOH – 33% CH3(CH2)10·COOH	22.8	154	38.02	[77]
72% Capric Acid – 28% Myristic Acid	72% CH3(CH2)8·COOH – 28% CH3(CH2)12·COOH	25.4	139	34.14	[77]
77% Capric Acid – 23% Stearic Acid	77% CH3(CH2)8·COOH – 23% CH3(CH2)16·COOH	27.8	123	30.89	[77]
58% Lauric Acid – 42% Myristic Acid	58% CH3(CH2)10·COOH – 42% CH3(CH2)12·COOH	35.2	162	39.26	[77]
70% Caprylic Acid – 30% Lauryl Alcohol	70% CH(CH)COH – 30% C12H26O	6.5	171	42.1	[57]
40% Lauric Acid – 60% Myristyl Alcohol	40% CH3(CH2)10·COOH – 60% C14H30O	24.3	161	38.82	[61]

Table 1.9 Inorganic-Inorganic eutectic mixtures for TES applications

Name	Mixture Formula	Melt Temperature [°C]	Latent Heat of Fusion [kJ/kg]	Energy Density [kWh/m^3]	Ref
45% Calcium Chloride Hexahydrate - 55% Calcium Bromide Hexahydrate	45% CaCl2·6H2O - 55% CaBr2·6H2O	14.7	140	101.64	[53]
66.6% Calcium Chloride Hexahydrate – 33.3% Magnesium Chloride Hexahydrate	66.6% CaCl2·6H2O - 33.3% MgCl2·6H2O	25	127	58.5	[133]
50% Calcium Chloride – 50% Magnesium Chloride Hexahydrate	50% CaCl2 - 50% MgCl2·6H2O	25	95	48.95	[53]
47% Calcium Nitrate Tetrahydrate – 53% Magnesium Nitrate Hexahydrate	47% Ca(NO3)2·4H2O - 53% Mg(NO3)2·6H2O	30	136	61.55	[53]
61.5% Magnesium Nitrate + 38.5% Ammonium Nitrate	61.5% Mg(NO3)2·6H2O - 38.5% NH4NO3	52	125	54.17	[53]
58.7% Magnesium Nitrate Hexahydrate – 41.3% Magnesium Chloride Hexahydrate	58.7% Mg(NO3)2·6H2O - 41.3% MgCl2·6H2O	59	132	55.05	[53]
53% Magnesium Nitrate Hexahydrate – 47% Aluminum Nitrate Nonahydrate	53% Mg(NO3)2·6H2O - 47% Al(NO3)2·9H2O	61	148	58.88	[53]
59% Magnesium Nitrate Hexahydrate – 41% Magnesium Bromide Hexahydrate	59% Mg(NO3)2·6H2O - 41% MgBr2·6H2O	66	168	78.47	[53]
14% Lithium Nitrate – 86% Magnesium Nitrate Hexahydrate	14% LiNO3 - 86% Mg(NO3)2·6H2O	72	180	79.44	[133]

energy density and latent heat but are only available at high transition temperatures. Metallic PCMs span a broad range of transition temperatures, however, their latent heat of fusion is low, making them unsuitable for weight constrained applications. They are also cost prohibitive for many applications. Salt/water solutions have mid-to-high latent heat, but moderate energy density, and are only suitable for applications requiring subzero transition temperature. The other PCM types are clustered around the 0 °C to 100 °C transition temperature range, with moderate energy density and latent heat.

Figure 1.3 depicts a comparison of the properties of different PCM types based on their material properties: latent heat by volume, latent heat by mass, cyclability, thermal conductivity, density, corrosiveness, and nucleation ability (i.e., susceptibility to supercooling). The comparison is relative, meaning the PCM type having the best performance for a given property is scored at 100% (exterior of circle), while the PCM type having the worst relative performance for that property is scored lower and towards the interior of the circle. For example, metallic PCMs have very

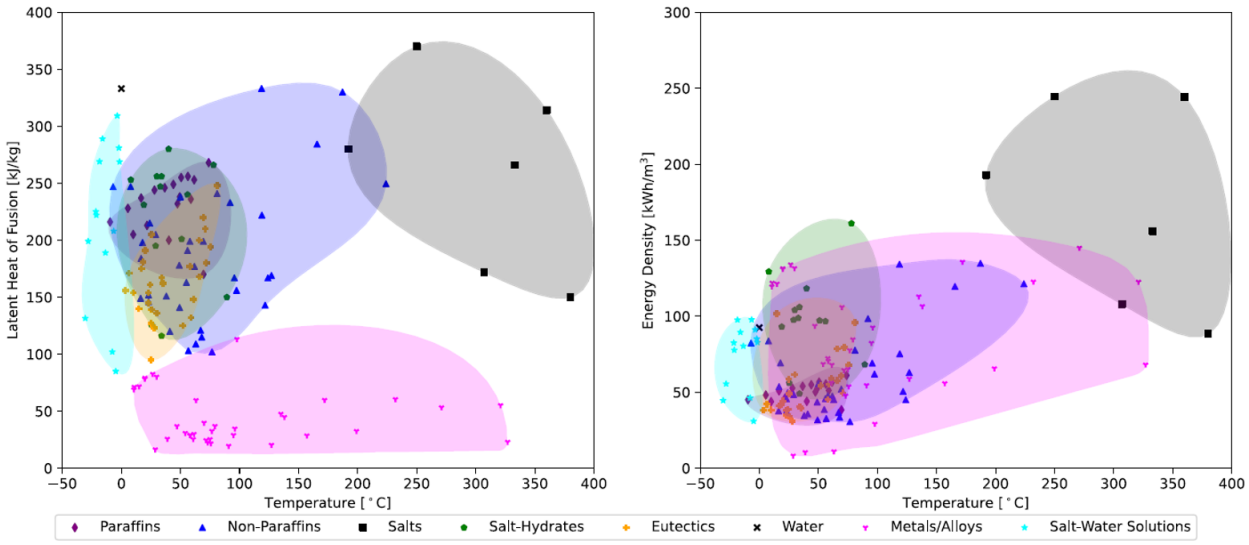

Figure 1.2 Latent heat of fusion and energy density versus phase transition temperature for the various PCM categories.

high thermal conductivity, while the other PCMs have lower thermal conductivity, with salt-hydrates being moderate, followed by salt/water solutions, salts, and then organic PCMs (paraffins and non-paraffins). Metals as PCMs do not supercool or corrode, have high density and thermal conductivity and high cycle life. However, their latent heat is typically quite low. Organic PCMs (paraffins and non-paraffins) also have strong nucleating ability (do not supercool), have high cycle life, and decent latent heat of fusion by mass. However, they have low thermal conductivity, density, and volumetric latent heat. Salt based PCMs typically have high latent heat (by mass and volume), density, and higher thermal conductivity than organic PCMs. However, they are corrosive, prone to supercooling, and can have poor cycle life due to phase separation.

1.2 Applications of PCMS

Thermal energy plays a central role in many engineering applications, from generating power to conditioning living spaces. Any application that involves generating or transferring thermal energy is a potential application for PCMs. Depending on the application, implementation of PCMs can result in one or more benefits,

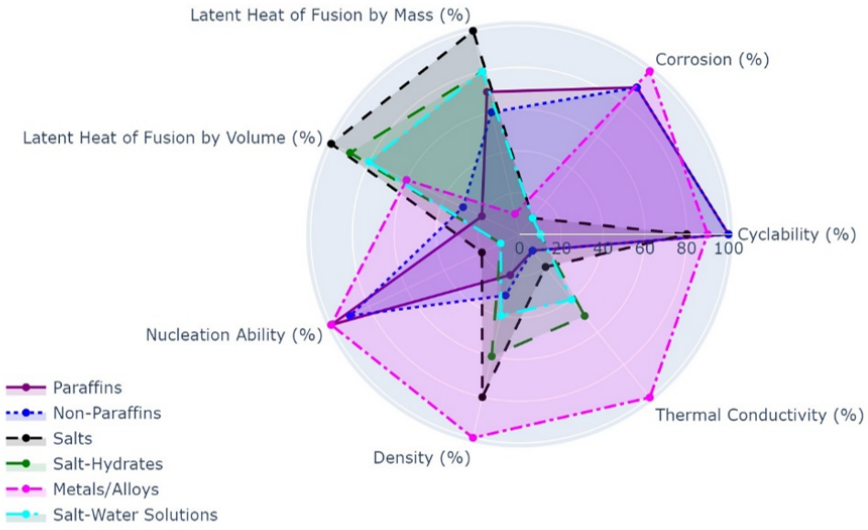

Figure 1.3 Comparison of PCM properties.

including energy efficiency (EE), emissions reduction (ER), load shaving/shifting (LS/S), and thermal management (TM), where TM is the ability of the PCM to prevent operation outside a system's safe or comfortable operating temperature range. Figure 1.4 lists common applications in the temperature range between –50 °C to 400 °C as well as a measure of the potential of PCMs to provide EE, ER, LS/S, and TM benefits for each of the listed applications. For example, incorporating PCMs in building air-conditioning systems provides a LS/S benefit and could potentially provide EE and ER benefits depending on system configuration and climate [3], but would not provide a TM benefit. Whereas incorporating PCMs into textiles or cooling fabrics worn by humans provides comfort thermal management and could potentially LS/S building loads if worn by enough occupants but is unlikely to provide EE or ER benefits. To further organize these applications, we have identified three major groupings: Building Applications, Thermal Management, and Power Systems and Industrial Processes.

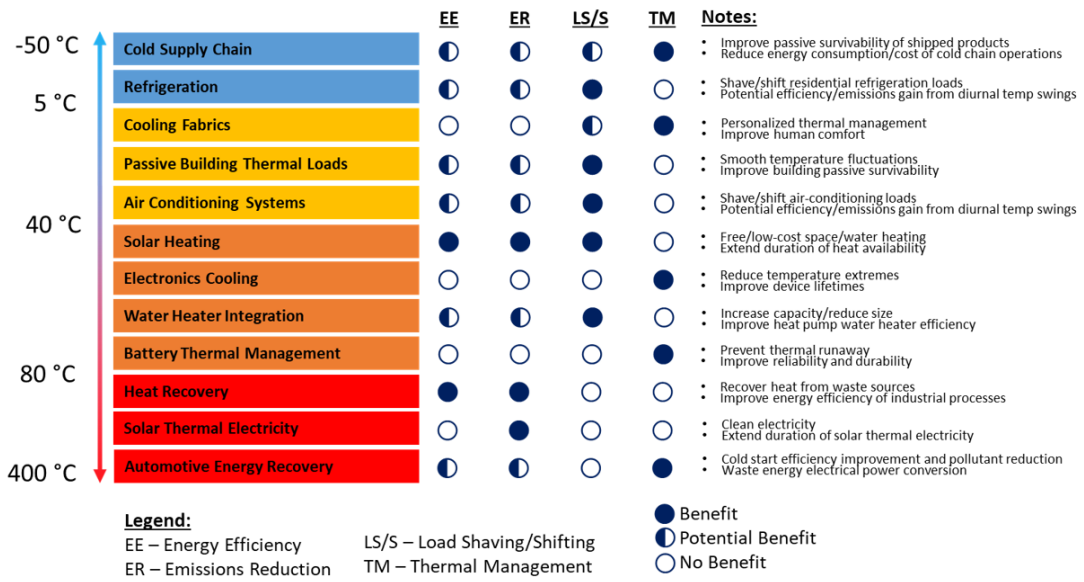

Figure 1.4 Common applications for PCMs across the temperature range of interest and the ability of PCMs to provide benefits to said applications.

1.2.1 Building Applications

As depicted in Figure 1.5, integration of PCMs into buildings appears in a variety of methods, that can be organized into two primary categories, passive and active [134–136]. Passive applications typically involve the addition of PCM to existing building materials or structures to increase thermal mass [137, 138]. The most common method for this is adding a PCM layer in the building wall [139]. When incorporated into a building structure, PCMs are typically included in macro-encapsulated layers, plaster/paste composites, or shape stabilized composites [137, 138, 140]. There are potential synergies with the growth of additive manufacturing concrete structures and materials research integrating PCMs in cement [141, 142]. PCMs have also been added to solar chimneys, a building feature that helps induce natural ventilation by utilizing solar radiation to heat the air. The addition of PCM helps reduce performance fluctuation by offsetting intermittency of solar radiation [143]. This implementation is also used in solar heating applications [144]. In another implementation, researchers found that the use of a PCM layer with solar

photovoltaic panels on roofs helped reduce overall building thermal loads [145].

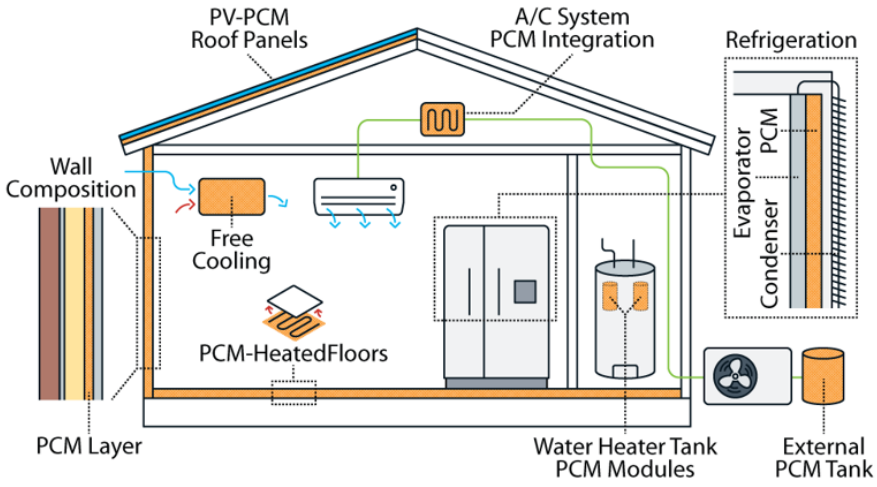

Figure 1.5 Potential implementations of TES within building applications.

Active applications typically use PCMs in a dynamic way where the PCM is combined with an air-side or fluid-side heat exchanger and integrated into electric-driven thermal equipment or appliances. A common active application is the use of campus-scale cold storage, typically using large chillers with water as the PCM. For cold storage in smaller systems, different PCMs with warmer melting temperatures are required due to equipment restrictions. This implementation has been investigated and tested for single-building HVAC systems [146–150]. Studies have often identified the power density (charge/discharge rate) and the heat exchanger as key limitations. Heat exchangers in HVAC applications have been a growing area of research for additive manufacturing, utilizing traditional advantages of polymer heat exchangers such as low-cost and corrosion resistance combined with the optimized designs enabled by AM [151]. PCM integration has been studied for other building thermal loads such as refrigeration and heating [152, 153]. PCMs have also been added to refrigeration systems both in container walls to provide additional thermal mass and integrated with the evaporator coil [154]. These methods help shave/shift electricity consumption, smooth out fluctuations in cooling load, and increase coeffi-

cient of performance, thereby reducing electricity consumption.

Active heating systems integrated with PCM have been investigated in two major forms, building integrated heating and domestic hot water heating [155]. Building integrated heating is similar to passive PCM integration, utilizing added thermal mass to condition a space with additional control of using active heating systems such as hot water or electric heating to charge the TES [156–158]. Domestic hot water uses macro-encapsulated PCM containers within the water heater tank either fixed at the top or floating with water level to help reduce thermal stratification [159–161]. Some systems have also investigated dedicated TES heat exchangers to heat the water using just PCMs as an alternative to large hot water tanks [162–164]. This use of TES as a separate storage device has been specifically coupled with heat pump systems, both for space heating and water heating, showing large potential electricity savings [149, 150, 165].

1.2.2 Thermal Management

Many products and systems such as vaccines or electronics must stay below a maximum allowable temperature. PCMs have been proposed in these applications as a passive form of thermal management. One of the most studied applications of PCMs for thermal management is for electronics [166]. The lifetime, reliability, and performance of electronic devices and packages are dependent on maintaining safe operating temperatures. PCMs are suitable for this task, especially for high-power electronics, photovoltaics, and battery thermal management, due to the high energy capacity and passive nature of PCM-based solutions [167–170]. Spacecraft systems are also a suitable application due to the need for low or no moving parts [171]. Batteries, photovoltaics, and space systems are suitable for PCMs due to the periodic nature of the loads, allowing for natural time for PCM to be recharged [166, 172]. Implementation in these cases typically includes either some thermal spreader such as heat pipes or a heat sink, or thermal conductivity enhancement in

the PCM. Most PCMs have low thermal conductivity and are dependent on natural convection to absorb heat. The addition of thermal conductivity enhancement or extended surfaces helps ensure adequate heat transfer between the heat source and the PCM. This has been an area of research for additive manufacturing, which excel at creating optimized extended surfaces for both traditional and PCM based heat sinks [173, 174].

The cold chain also utilizes PCMs in containers for temperature sensitive goods such as vaccines allowing for more flexibility in transportation [175, 176]. Similarly, PCM has been added to packaging for temperature-sensitive foods [177, 178]. Biomedical applications overlap heavily with cold chain for products such as vaccines and medicines, but they also include thermotherapy and medical dressings [179]. Here, PCM packaged with hot/cold pads or wound into different fabrics with microencapsulated composites are used to maintain temperature [180]. Integration into textiles also has a variety of uses for human comfort such as sportswear or bedding materials [181].

1.2.3 Power Systems and Industrial Processes

High transition temperature PCMs can be used in power systems and industrial processes. One area of opportunity is waste heat recovery for industrial process heat. One study found that heat recovery utilizing PCM thermal energy storage resulted in 50-70% energy savings related to heating an industrial batch process [182]. The importance of high storage discharge rates was a notable requirement and the lack of commercially available PCMs in the 120 °C to 200 °C transition range was noted as well. High heat transfer rates are of importance in many industrial processes and are a driving factor for development of AM heat exchanger designs [183]. There have also been studies exploring use of PCM TES to transport waste heat from industrial sources to demand locations such as hospitals [184]. Vehicle systems can benefit from the use of PCMs for thermal management also,

allowing for buffering of peak thermal loads and for energy storage to improve cold start performance [185–187]. Concentrated solar power (CSP) plants can make use of PCM as an energy storage media for thermal electricity generation, typically utilizing PCMs with transition temperature greater than 300 °C, however, some studies have investigated temperatures as low as 120 °C for CSP applications [188, 189]. Another power intensive process that can be improved with the use of PCMs is water desalination. The addition of PCM into the basin of solar desalination devices can improve yield and overall efficiency [190].

1.3 Advanced Manufacturing with Phase Change Materials

The effectiveness of a PCM device is defined by its energy and power density—the total available storage capacity (kWh) and how fast it can be accessed (i.e., heat transfer rate) (kW). Although many PCMs have high latent heats of fusion, which provides high storage capacity, most have low thermal conductivity, which can potentially limit how quickly and effectively the latent heat in the PCM can be accessed. This presents an issue when attempting to disperse heat through large blocks of PCM. To mitigate this issue, researchers have turned to either (a) increasing the thermal conductivity of the PCM through additives such as expanded graphite [191], carbon fibers [192], and/or metallic particles [193] or (b) utilizing metal fin structures [194] and/or metallic foams [195] to diffuse heat more effectively. However, adding material, either through additional thermal-conductivity-enhancing particles or metal structures, displaces PCM which reduces the available thermal energy storage density.

The Ragone plot, originally developed to analyze the performance of batteries, can be applied to thermal energy storage heat exchangers [196–198]. Ragone plots quantify the energy (kWh) versus power (kW) for PCM heat exchangers. A typical Ragone plot is shown in Figure 1.6(a). The general goal of TES heat exchanger design is to maximize available energy (energy storage) and power (rate of heat trans-

fer). In a Ragone plot these goals push the knee in the curve in Figure 1.6(a) further up and to the right. High energy and power densities requires low thermal resistances between the heat source or sink and the PCM phase front. Additive manufactured TES heat exchangers can achieve this in two ways – by increasing the effective thermal conductivity of the PCM with conductive scaffolding or by modifying the geometry to increase surface area and reduce heat transfer length scales. Examples of how conductivity and geometry impact Ragone curves is shown in Figure 1.6(a-b). These results were obtained using a 2-D discretized model of a PCM heat exchanger, assuming all heat flow through the PCM is governed by conduction [198]. Increasing thermal conductivity lowers the resistance, which can increase the achievable power density from the baseline pure PCM curve (black) to the red curves that contain 2.5, 5 and 10% of a thermally conductive additive by volume. However, conductivity enhancements come at the cost of reducing the volumetric storage capacity since any scaffolding material displaces some of the active PCM. These effects must be considered together to achieve the optimal energy density for the desired charge or discharge rate (power), as shown in Figure 1.6(c). The optimal point will be a function of the application, which is discussed in more detail in Section 3. For example, a cold chain or building application may require relatively low power densities, meaning the PCM will discharge over a log period (4 or more hours). For these situations, only a relatively small increase in thermal conductivity may be enough. Conversely, thermal management applications often call for high power densities (discharge rates on the order of minutes or seconds). In these cases, there are significant benefits to increasing the thermal conductivity, as shown in the third panel of Figure 1.6(c).

Additive manufacturing can also leverage novel geometries to pass fluid through a PCM heat exchanger in intricate flow paths. This can decrease the heat transfer length scale and increase the surface area, which both reduce internal resis-

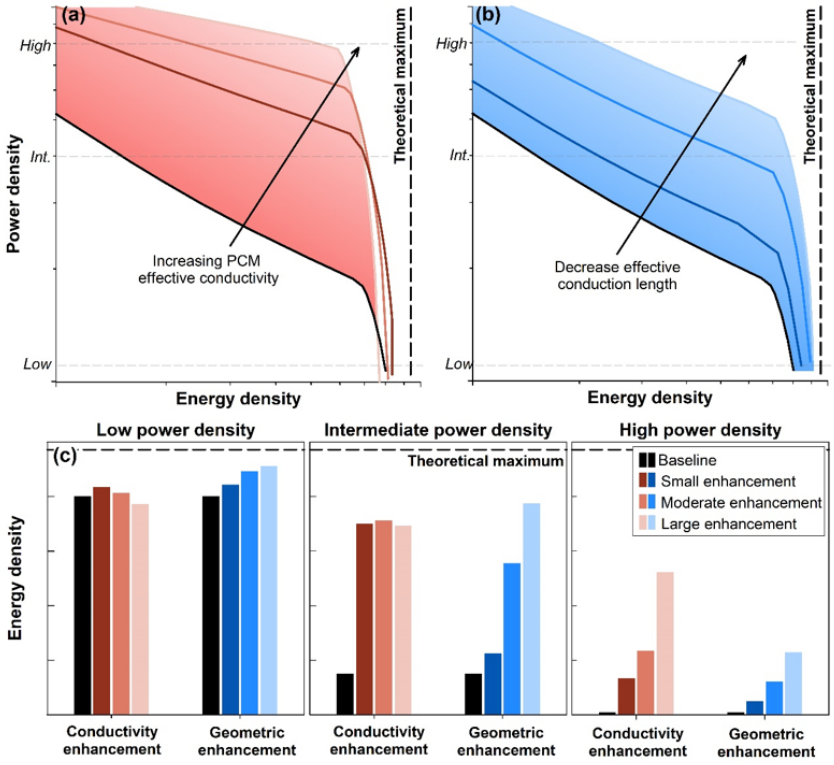

Figure 1.6 The performance of a thermal energy storage component in terms of energy and power density with different levels of enhancement, attainable using additive manufacturing. Panels (a) and (b) show Ragone plots for a round tube surrounded by PCM. The black curve shows the baseline case with a pure PCM, and the (a) red and (b) blue curves show different levels of conductivity and geometric enhancement, respectively. The energy density at three different power density levels (shown on the y-axis in (a) and (b)) is plotted for different enhancement schemes in (c). Note – the energy density is shown on the x-axis in the Ragone plots and on the y-axis in (c). The dashed black line in all three plots represents the maximum possible energy density, which is simply the energy storage capacity of the material alone with no flow channels or conductive additives.

tances. An example of how geometry can impact the Ragone curve is shown in Figure 1.6(b). These results specifically look at reducing the diameter of the fluid channel and increasing the total length, simulating a case where the fluid channels serpentine through the PCM. Although the geometry isn't optimized, in Figure 1.6(c) the results show that modifying the geometry can improve performance at all power levels. It is expected that topology optimized TES heat exchangers will

make large gains to improve overall charge and discharge efficiencies.

Ideally, with the advent of additive manufacturing for TES heat exchangers, both the energy density and the power density can be co-maximized. AM allows for creation of ultra-compact high-surface-area-to-volume heat exchangers that reduce overall weight while maximizing PCM volume and heat transfer surface area on both the PCM side and fluid side. AM can also enable thinner walls, further reducing thermal resistance [199]. These geometry-enabled advancements are not possible with traditional manufacturing techniques. Furthermore, as discussed later in this article, recent research has shown the ability to directly 3D-print functional composite filament with PCM directly incorporated into the structural wall material [200–205].

1.4 Review of PCMs and Composites used in Additive Manufacturing

1.4.1 PCMs and Matrix Materials Used in AM

All AM PCM components contain two key elements – the PCM itself and a matrix to contain and potentially enhance the properties of the PCM. The nature of the matrix material selected is directly related to the AM method in which it is processed. These matrix materials are used to develop (1) filaments, (2) resins, (3) inks, and (4) powders shown schematically in Figure 1.7 that are then assembled in a layer-by-layer fashion using thermal, evaporative, and light-based processing. As the AM PCM field has evolved, so has the relationship between the matrix and the PCM. In the most common efforts, a device is fabricated via AM and backfilled with a PCM. Increasingly, material and printing advancements have enabled direct incorporation of PCMs into the matrix material through physical blending, particle dispersion, coaxial extrusion, or chemical grafting, and in select cases, directly printing the PCM without a supporting matrix.

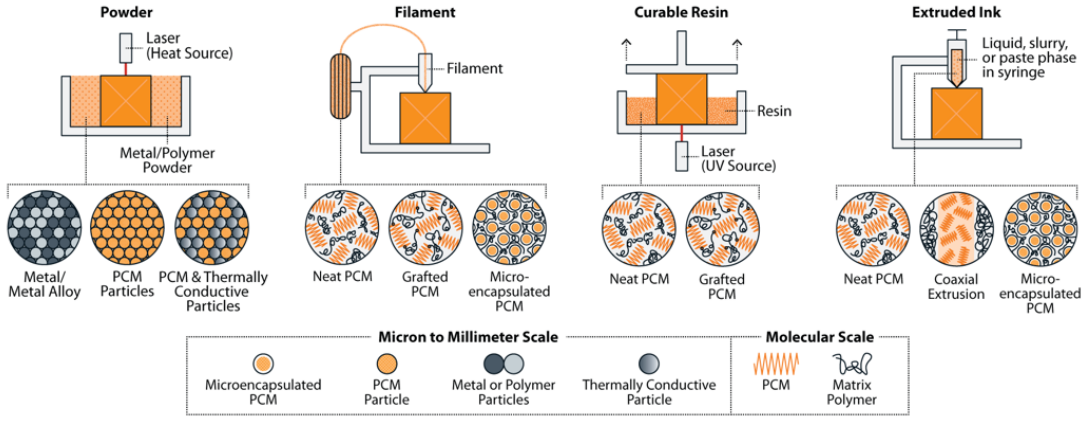

Figure 1.7 Graphical depiction of common additive manufacturing methods; a) selective laser sintering (SLS), also known as selective laser melting (SLM); b) fused filament fabrication (FFF), also known as fused deposition modeling (FDM); c) stereolithography (SLA); and d) direct ink writing (DIW). Varying forms of AM materials with different methods to incorporate PCMs into the matrix.

PCMs used in AM

The PCMs targeted in AM applications are largely organic in nature, due to low corrosivity, high latent heats of transition, limited supercooling and thermal stability at elevated temperatures required for some AM processes. Most PCMs used in AM applications exhibit solid-liquid transition behavior, which generally have higher latent heats compared to solid-solid transitions.

Commonly utilized PCMs for AM applications are (1) paraffins [206–216], (2) alkanes [211, 216–223], and (3) polyethylene glycols (PEGs) [224–226]. Other PCMs used include a sugar alcohol, fatty alcohol, fatty acid, and water [227–231]. Commercialized PCMs are routinely utilized due to the variety of transition temperatures and are available both in neat [200, 201, 232–248] and microencapsulated forms [204, 233, 249]. In an example of a metal PCM, researchers capitalized on the solid-stated transition of a nickel titanium alloy from monoclinic Martensite configurations to a cubic Austenite lattice for AM metallic parts [250]. Another case of metal PCMs used a printed aluminum-tin alloy where tin was the PCM due to

its comparatively low melting temperature [251]. Other niche PCMs include a thiolated octadecane derivative and stearyl acrylates, which are derivatives of the fatty acid stearic acid intended for chemical grafting and polymerization [207, 252–254].

Filament Materials

Filament-based AM is one of the most widely used forms of AM due to its low equipment and material cost, limited post processing requirements, and diversity in availability of materials. Compared with other AM techniques, filament-based processes have lower layer resolution, weak inter-layer adhesion, and may require support structures for complex parts. Due to the ease of filament accessibility and processing, incorporation of PCMs has taken several forms, (1) neat PCM blending, (2) dispersion of microencapsulated PCMs (MEPCMs), and (3) copolymerization. All filaments that encapsulate PCMs have been polymers like high density polyethylene (HDPE) [200, 201], polycaprolactone (PCL) [233], thermoplastic polyurethanes (TPU) [225, 249], acrylonitrile-butadiene-styrene (ABS) [241, 248, 255], and nylon [204].

For filaments incorporating neat PCM, encapsulation relies on solubility and uptake of the PCM into the filament material that remains upon extrusion and printing [200, 201, 233]. Addition of commercial PCMs to matrix materials has been done in the solution phase with PCL as well as mechanical mixing in the melt state prior to extrusion with HDPE [200, 201, 233]. Using HDPE as a matrix, 40 wt% of PCM was mixed in with good filament extrusion properties and a transition enthalpy of 64 J/g [201, 202]. Using PCL as a matrix, PCM additions up to 60 wt% were made, but only 20 wt% PCM filaments were printed, reducing the PCM transition enthalpy from 25 J/g to 10 J/g in the printed state [233].

MEPCMs have been incorporated into nylon, TPU, and PCL filament types. Methods of integration can be divided into (A) powder mixing and (B) solution dispersion. In two examples, MEPCMs were mixed with polymer powders and ex-

truded directly into filament achieving MEPCM contents between 30–50 wt% and exhibited melt enthalpies in the range of 46–70 J/g for the printed parts [204, 249]. Using solution processes, PCL was dissolved in chloroform and 60 wt% MEPCM was dispersed in the solution prior to drying and breaking up into pellets that had a melt enthalpy around 40 J/g [233].

Along with using MEPCMs to prevent PCM leakage from filaments, direct covalent bonding of the PCM with the filament matrix material has been shown to be an effective method to achieve TES in a printable material without leakage. Yang et al., capitalized on the hydroxyl end groups of PEG 8000 to copolymerize with an isocyanate-terminated TPU precursor to form domains of PEG that could melt and crystallize while tethered to the matrix materials, exhibiting a quasi-solid-solid phase transition with a transition enthalpy of 65 J/g, which did not diminish even after >2000 cycles [225].

Resin Materials

Resin-based AM relies on crosslinking photocurable chemical groups with a laser at each layer. This process, stereolithography (SLA), produces high resolution objects at a relatively rapid rate. Compared with other AM techniques, resins can be costly and hazardous, and the printed parts can require extensive post-processing, and support material cannot be reused. The types of resin materials that have been combined with PCMs include: acrylamides [231], acrylic esters [224], siloxanes [207, 252], and stearyl acrylates [254]. An important limitation of resin approaches is that any material mixed into the resin must not optically interfere with the light source which initiates photocuring. As such, dark or highly opaque materials must be avoided.

When integrating PCMs into resin-based systems, researchers have blended neat PCM into resins as well as covalently linked PCMs into the resin matrix. With PCMs blended into resins, the PCM domains would ideally be locked into the crosslinked

structure with curing. Wang et al., mixed two PEG PCMs into an acrylic ester resin and printed a simple rectangular prism (5 x 5 x 35 mm) with layer resolutions of 50 μm. At temperatures above PCM melting, PEG seeped to the surface of the print. The PEG seepage, coupled with a low latent heat, 7.2 J/g indicates substantial durability issues with the composite [224]. Gogoi et al., used water as the PCM absorbed into a flexible, SLA printed acrylamide-alginate hydrogel supported by PDMS at a size of 30 x 30 x 60 mm. In this example, water is supported through secondary intermolecular interactions and the flexibility of the hydrogel-PDMS system accommodates the volumetric changes with water during phase transitions [231].

A few efforts have used derivatives of solid-liquid PCMs that can be grafted to polymer backbones or directly polymerized into a brush configuration. Singly tethered ends of attached PCMs restrict mobility and inhibit leakage while leaving the other end free to undergo crystallization and melt events exhibiting a quasi-solid-solid phase transition. Ma, et al. used thiolated derivatives of octadecane as a PCM with the ability to be grafted to siloxane matrix materials and achieved transition enthalpies in the range of 25-125 J/g with print sizes around 30 x 30 x 5 mm [207, 252]. Utilizing a macromonomer approach, Mao, et al., used an acrylate derivative of stearic acid along with an acrylamide monomer and crosslinker. These were copolymerized during the printing process to form a polymer network that had a transition enthalpy around 70 J/g [254].

Ink Materials (Direct Ink Writing)

Ink based materials in the AM context refer to liquids or slurries that are directly extruded in a layer-by-layer fashion in a process called direct ink writing (DIW). As the ink is deposited, solidification of each layer can occur through thermal curing, photocuring, solvent evaporation, or reactions with the solvent [256]. Because ink-based AM can accommodate numerous curing processes and can be

performed at low temperatures, there is large diversity in material selection, which is advantageous over other, more restrictive techniques. A notable disadvantage of ink-based AM includes the high degree of control required over the rheological properties to achieve high resolution, cohesive prints. Matrix materials that have been targeted for DIW of PCM composites include siloxane [207], cements [230, 257–259], graphene oxide [223], and a commercial UV curable resin [211]. The thiolated octadecane grafted to a siloxane matrix material developed by Ma et al. discussed in the previous section was demonstrated to be able to be processed via DIW utilizing a high temperature UV curing step after printing [207].

In an example of coaxial DIW, Yang et al., demonstrated a thermally conductive graphene oxide ink printed as a sheath around a pulsed octadecane core that demonstrated a composite transition enthalpy and thermal conductivity of 190 J/g and 1.67 W/mK, respectively [223]. The pulsations of the PCM core created isolated "beans" within the graphene oxide sheath that mitigated leakage in the event of localized damage to the print not resulting in the total leakage of the PCM. Using a similar process of creating localized regions of PCM within the matrix, Wei et al., created small waxy beads using emulsion processes and suspended the beads in a commercial resin typically used for SLA printing. Because the ink could be extruded and each layer UV cured at temperatures below the 60 °C melting point of the paraffin PCM, the matrix was cured around the PCM beads in the solid state and prevented leakage from the print to achieve a transition enthalpy of 102 J/g.

An innovative development in ink-based AM utilizes electrostatic potentials to deposit <10 μm diameter minuscule droplets of paraffin on a substrate with extremely high resolution in a process deemed electrohydrodynamic (EHD) 3D printing. While not focused on TES and PCM applications, the demonstration of high-resolution methods of paraffin ink printing has potential for advanced PCM composite fabrication with spatially selective deposition of PCMs at resolutions <10

μm [260–262].

An emerging field of DIW TES composites is focused on PCM incorporation into cementitious materials for building-scale thermal management [230, 257–259]. In these materials, PCMs are dispersed in cement slurries that are then deposited in a layer-by-layer fashion. The highest transition enthalpy achieved in an AM cement-PCM composite was 40 J/g using a neat paraffin PCM [257].

Powder Materials

Fabrication of AM structures via powder processing utilizes a laser to selectively melt or sinter particles into a cohesive structure. These powder-based processes are known in the AM community as selective laser sintering (SLS), powder bed fusion, and direct laser metal sintering. Powder-based AM can yield high resolution parts with high interlayer strength and moveable components without the need for printed supports. However, powder-based AM processes can be slower than other AM techniques and the required hardware can be expensive.

The materials space of powder-based AM is largely dominated by metal powders. Metallic materials for AM offer high thermal conductivities but often at the expense of cost, corrosion resistance, and weight. In AM PCM devices, aluminum-silicon alloys, commonly containing magnesium, have been the most widely used due to their high strength-to-weight ratio, corrosion resistance, and ease of powder processing through laser sintering. The most common alloy is AlSi10Mg [206, 212, 213, 217, 219, 222, 226–228, 232, 236, 238, 246, 247, 263], but other aluminum-silicon formulations [220, 221, 234, 240] as well as other aluminum alloys [214, 215, 235, 237, 243–245, 251, 262] have also been used. Other metals printed for PCM applications have included copper alloys [216, 245], steel alloys [242, 245], nickel alloys [250], and titanium alloys [245]. These efforts produce metal structures that are generally fabricated to be porous for backfilling with PCM and focus on optimizing geometries that encourage rapid charging/discharging of the PCM [206,

212–222, 226–229, 232, 234–248, 255, 262, 263]. The backfilling of metallic AM devices with bulk PCM capitalizes on high thermal conductivities, leak resistant structures, and considerable PCM volumes for high energy capacity. A few AM metallic structures have sought to use the metal as the PCM. Sharar et al. examined the solid-solid phase transition of a nickel titanium alloy, achieving a transition enthalpy of 16 J/g at 25 °C [250]. In a solid-liquid transition of a metal PCM, Confalonieri et al. capitalized on the low miscibility of tin within aluminum and the lower melting temperature of tin to achieve a transition enthalpy of 24 J/g at 230 °C [251].

Some special cases of powder based PCM composites exist where organic PCMs act as the binder during the powder fusion process. In a series of studies carried out by Nofal, et al., paraffin was used both as the PCM and the binder in combination with expanded graphite (EG) for laser sintering into multilayer composites in a variety of shapes that were 80% paraffin by weight and exhibited transition enthalpy of 155 J/g and thermal conductivity of 0.85 W/m K [208–210]. Using laser sintering methods for EG-PCM composite fabrication circumvented traditionally lengthy and wasteful processing like press-soak manufacturing that rely on PCM infiltration into EG powder prior to compaction [40, 169]. In another organic powder-based AM precursor, the derivative of the PCM stearic acid, stearyl acrylate, was polymerized via both suspension and solution polymerization to yield particles of variable size that would allow for adequate coalescence during the powder fusion process. The parts fabricated using powdered poly(stearyl acrylate) exhibited a transition enthalpy of 82 J/g [253].

1.4.2 Thermal Conductivity Enhancement

Thermal conductivity is an important property of PCMs and thermal energy storage systems, as the thermal conductivity of PCMs affects the charging and discharging time of the material. Due to low heat transfer rates of some PCMs (i.e.,

organic PCMs), thermal conductivity enhancement has been utilized as a means of enhancing the rate of charging and discharging heat. Moreover, base polymeric materials used in AM often suffer from low thermal conductivity. Additives are thereby incorporated to increase the heat transfer rate of the composite material. Additives utilized for thermal conductivity enhancement are typically materials with inherently high thermal conductivity. Of note, thermal conductivities of additives and their effect on TES devices can be highly variable depending on factors such as particle size, filler volume, crystallinity, and orientation within the composite [264]. Shemelya et al., show that anisotropic thermal conductivity for 3D printed structures is related to the print direction and filler morphology, meaning that thermal conductivity can be controlled through a combination of print raster direction and material design [265]. Therefore, further optimization techniques for AM components can be employed to improve the thermal conductivity.

During FFF (or FDM) anisotropy of the filament occurs due to the differing degrees of interdiffusion in the in-plane and out-of-plane directions of the filament and incongruent layering between the filament [266]. Studies primarily focus on the mechanical properties of AM components; however anisotropic characteristics of the AM components can significantly vary along the print direction [267]. Anisotropy occurs due a discontinuity of material across the print layers. Control over anisotropy can be achieved by modifying the polymer matrix and adjusting the print parameters [268, 269]. The particles or fillers used to enhance thermal conductivity provide conductive pathways within raster direction of the composite when they are aligned in the proper orientation.

Improving heat transfer in AM objects can be controlled before, during, and after manufacturing utilizing appropriate design optimization principles, material selection, and post-processing of the AM component. There are three parameters that can be tailored to improve the heat transfer of AM components: (1) mate-

rial selection and incorporation, (2) fabrication parameter optimization, and (3) post-processing techniques to improve thermal conductivity. Selection of the appropriate TC enhancing additive, matrix material, and mixing ratio are crucial for good heat transfer and cohesive prints. During AM fabrication, an optimized design of the 3D model is generated, printing directions are chosen, and other printing parameters are determined to increase the adhesion between the printing bed and printed parts. The fabrication step also includes tailoring the surface roughness of the AM components based on printing conditions and slicing strategy to reduce the staircase effect [270, 271], and controlling local thermal conditions through microstructure (i.e., grain nucleation in metal AM components) [272, 273]. The post-processing treatment includes mechanical polishing and thermal or vapor annealing that can be directly applied to the surface of the printed part [274].

Thermal conductivity in AM components is generally lower than its parent material with the reduction most pronounced in the build direction [275–277]. The reduction in the thermal conductivity and the inherent anisotropy of AM components is due, in part, to incomplete fusing and substantial thermal contact resistance between the layers [275]. Certain AM processes lend to better interlayer adhesion and mitigate reductions in thermal conductivity.

Material Additives for High Thermal Conductivity

Materials development can be utilized with fundamental design principles for enhanced thermal conductivity. These composites often consist of a base polymer and a thermally conductive filler (e.g., graphene, boron nitride, aluminum oxide) [278]. For a thorough review of material parameters the reader is referred to Almuallim et al. [273]. The thermal conductivity of the base polymers is often on the order of 0.04-0.36 W/m K [279]. High thermal conductivity fillers, like carbon derivatives, metals, or ceramics are added to polymer-based composites to enhance the overall thermal conductivity of the composite.

Additives based on carbon derivatives are available in a variety of allotropes and commonly include carbon fibers and nanotubes, graphene, and carbon black have been widely studied for their effect on improving the thermal conductivity of polymer composites, as well as mechanical properties [280–282]. Carbon-based additives have advantages of high thermal conductivity, chemical stability, and low density (2 g/cm3) [283, 284]. Thermal conductivity measured at ambient conditions (25 °C) of expanded graphite (EG) can range from 4-400 W/mK [285], carbon nanotubes (CNT) 2000-6000 W/mK [286], and carbon black (CB) 30-170 W/mK [287]. In carbon-based additives, geometry (i.e., how the carbon additive is oriented within the material) plays a role in the improvement of thermal conductivity. Alignment of conductive fillers or fibers in the print direction can assist in the direction of heat flow through the printed material. Liao et al., showed that as the carbon fiber content increased above 4 wt.%, the thermal conductivity rapidly increased from 0.221 W/mk to 0.835 W/mk, which may be due to carbon fibers in the matrix establishing a continuous heat-channel to efficiently enhance the conductivity, resulting from the preferentially alignment of the carbon fibers in the print direction [288]. Wang et al. utilized CNTs to prepare a composite aerogel, via melt deposition of the initial hydrogel, that exhibited anisotropic thermal conductivity of 0.025 W/mK in the axial direction and 0.302 W/mK in the radial direction as the CNT filler ratio increased [289]. Shemelya et al. showed key thermal conductivity results for ABS/graphite composites, where the thermal conductivity was measured in the z-plane to be 0.25 W/mK and the x-y plane at 0.37 W/mK [265]. It was noted that the ABS/graphite composite exhibited noticeable thermal anisotropy due to the as-printed alignment of the graphite flakes.

Ceramic fillers such as boron nitride, silicon carbide, aluminum nitride, and silicon carbide are used for their high thermal conductivity, low coefficient of thermal expansion, and electrical resistance [273]. Among these fillers, aluminum ni-

tride has the highest thermal conductivity (140-180 W/mK), followed by silicon carbide (120 W/mK) [290], and boron nitride (30 W/mK) [291]. Other niche additives include, metal organic frameworks (MOFs), titanium dioxide foam, and nickel foam [292]. Li et al. investigated the particle size of hexagonal boron nitride (h-BN) with a fixed filler content on composite properties of FFF printed components using isotactic polypropylene [293]. Their results show that the particle size of the h-BN filler had a significant effect on the thermal conductivity, with composites exhibiting 2.02 W/mK parallel to the print direction. They concluded that the heat conduction formed by the aligned h-BN particles contributed to the improved thermal conductivity along the print direction. Sonsalla et al., tested Zn-SiC (zinc-silicon carbide) composites and determined that the addition of Zn-SiC improved thermal conductivity from 0.20 W/mK in the horizontal direction for the ABS control to 0.42 W/mK and further enhancement of 0.60 W/mK in the vertical direction due to alignment with the filament print direction [294].

Ongoing research and development studies indicate that the challenges of the improving the thermal conductivity of PCMs focus on the aspects of clarifying the phonon scattering mechanism in PCMs, increasing the number of thermal conductivity chains and broadening the thermal transmission channels [292]. Furthermore, increasing the thermal conductivity of AM composites with additives that have higher thermal conductivity than the parent matrix is affected by size, shape, and filler amount, which can play a role in the phonon transport properties of the matrix [273]. High contents of additives reduce the thermal storage capacity (i.e., latent heat). It is important to consider not only additives but relative amounts when improving thermal conductivity.

Fabrication Parameters for Improved Thermal Conductivity

Outside of materials development, improving thermal conductivity in AM components can be done through to optimization of printing parameters. Printed

geometries can be utilized such as lattice structure geometries can be printed to increase the thermal conductivity in an AM component [213]. Many studies report on the print parameters (e.g., layer height, fill density, print speed, nozzle diameter) for improvements in mechanical properties, but few report on the printer settings for thermal conductivity of 3D printed components. In optimizing the printing parameter, a study by Sonsalla et al., determined that the thermal conductivity of a 3-D printed structure was directly affected by fill density, layer height, and print speed. Nozzle diameter was found to be negligible in its effect on thermal conductivity [294]. An increase in the thermal conductivity was observed with an increase in the fill density. Additionally, they demonstrated optimal layer height of 0.4 mm and fill density of 100% to achieve the highest thermal conductivity for a 3-D printed object fabricated with a homogenous material printed in a horizontal orientation.

In another study by Elkholy et al., the effect of layer height and raster width and results showed that increasing the layer height and width causes a deterioration in the thermal conductivity up to 65% when compared to the pure polymer [295]. They also found that decreasing the fill ratio decreases the thermal conductivity and that adding a carbon fiber filler improved the thermal conductivity in the z and y direction by 26% and 162%, respectively [295]. They determined that the effect of raster width was more significant that the layer height in reducing the thermal conductivity in all directions due to porosity generation [295].

While optimization of printing parameters is important, this approach can be limited due to the process parameters and can negatively impact the production capacity (i.e., lower extrusion speeds reduce the output).

Post-Processing for Improved Thermal Conductivity

Post-processing of AM components has been shown to improve the thermal conductivity in extruded components via, thermal annealing [277]. In traditional

metal manufacturing thermal annealing is used to improve the grain structure and contact resistance [296]. The thermal contact resistance that exists between the layers of the AM components is often hard to show due to difficulties in experimental measurements and is not reported widely in the literature [275]. Thermal contact resistance occurs in the z-direction due to the interfaces between the layers and may impede the heat flow and mechanical strength when compared to the x-direction [275, 297]. Prajapati et al. showed that strong interfacial thermal contact resistance in the build direction was the cause of anisotropy, and that air gaps in the microstructure cause a reduction in the thermal conductivity in the measured raster direction [275]. They showed significant improvements in the thermal conductivity were observed when the polymers, ABS and ULTEM thermoplastic materials, were annealed at 135 °C for 96 h [275].

Vapor finishing techniques are used to smooth outer surfaces of the printed parts and serve to help lower thermal contact resistance with adjacent components at the surface; however, it is unclear if there is a significant impact on the interior geometry and thus the effective thermal conductivity of the printed parts [295].

1.4.3 Advanced Manufacturing for Integrating PCMs into Devices

3D-Printed Scaffolds for Thermal Batteries

One of the most common methods of combining PCMs with advanced manufacturing is by generating scaffolds that are then backfilled with various materials. By utilizing materials with high levels of thermal conductivity to build the scaffolds, these structures are capable of generating thermal batteries that can more quickly be charged and discharged relative to encapsulated PCMs alone. Furthermore, the ability to utilize computer aided design (CAD) software to produce intricate scaffolds with high levels of surface area allows for optimized advanced manufacturing. For instance, Qureshi et al. utilized aluminum AlSi10Mg gas-atomized powder to 3D print metal scaffolds via laser powder bed fusion , which produced in-

tricate structures with high levels of surface area and thermal conductivity. With 85-90% porosity, the structures were then back-filled with molten paraffin wax-based PCM to generate thermal batteries [238].

Similarly, Guo et al. developed metal printed scaffolds from AlSi10Mg through selective laser melting and back-filled them with n-tetradecane, resulting in a PCM thermal energy storage device with 13 times greater thermal conductivity than the selected PCM for faster charging/discharging [298]. Yazdani et al. 3D printed an aluminum silicon alloy (AlSi10Mg) grid as an extended surface on a flat plate heat exchanger using a selective laser melting process. The heat exchanger was tested with different grid designs charging/discharging paraffin wax and myristic acid. The proposed application was cooling high power 5G electronics and using the waste heat for other applications such as space heating [227]. A parametric 2D FEM simulation was used for the design of an additively manufactured thermal storage device. Several designs were printed out of AlSi10Mg using direct laser metal sintering (DLMS) and tested in a coolant loop with paraffin wax as the PCM [206]. Additionally, a maraging steel two-phase heat exchanger was manufactured using DLMS by Kabir et al. that was then backfilled with a commercial bio-based PCM, PureTemp25. The heat exchanger was designed for use as a thermal capacitor or thermal storage in spacecraft thermal management systems, using methanol driven by capillary pumping pressure within the wick structure [242].

PCM-Integrated Materials for Wearable Technology

One unique application space for advanced manufactured PCM devices that has received much study is wearable technology. For example, the acrylamide-alginate hydrogels developed by Gogoi et al. were designed as a wearable technology intended for cooling athletes during training and competitions. These composite prints possess a high level of wear resistance and mechanical stability suitable for this application. This technology is being explored for commercial use under the

name CoolPak Hydrogel [231]. In another study for wearable technology that incorporates PCMs, the octadecane grafted siloxane composites developed by Ma et al. deposited their SSPCM on carbon fiber cloth, enabling temperature regulation for the wearer [252]. They demonstrated the cooling potential with surface skin temperature reductions from 46 °C to 38 °C over 20 minutes. The crosslinked stearyl acrylate gel developed by Mao et al. were printed on fabrics such as cotton and demonstrated a prolonged equilibration time with the hot/cold stage indicating thermal regulation capabilities. The authors propose that this PCM-integrated gel on fabric may be applicable to the wearable technology market [254]. The PEG-TPU copolymer created by Yang et al. utilized single-walled carbon nanotubes (SWNT) to facilitate heat transfer to solid-solid PCM that was 3D printed into flexible sheets for cooling fabrics. At 1 wt.% SWNT, these sheets possessed a thermal conductivity of 0.52 W/m-K and demonstrated rapid thermal regulation from 30 °C to 60 °C and back to 30 °C in just 2 minutes. latent heat of 65 J/g.

1.5 Commercially Available Materials and Systems

This section will outline a few specific examples of PCMs being utilized in commercial products. See the recent work by Mehling et al. for a comprehensive review of the state of PCM-based products across multiple industries [299]. A graphical timeline of major developments in the commercial development and implementation of PCMs is outlined in Figure 1.8.

1.5.1 Phase Change Material Manufacturers

Several companies have developed PCMs with a range of chemistries including paraffin, bio-based, and salt hydrate based PCMs. These companies, listed alphabetically, include (but are not limited to) Axiotherm [300], Boyd Corporation [301], Climator Sweden AB [302], Crodatherm [303], Eastex [304], ExxonMobil [305], Henkel Electronics Materials [306], Honeywell Electronic Materials [307], Insolcorp [308], Laird (DuPont) [309], Microtek Laboratories [310], Phase Change So-

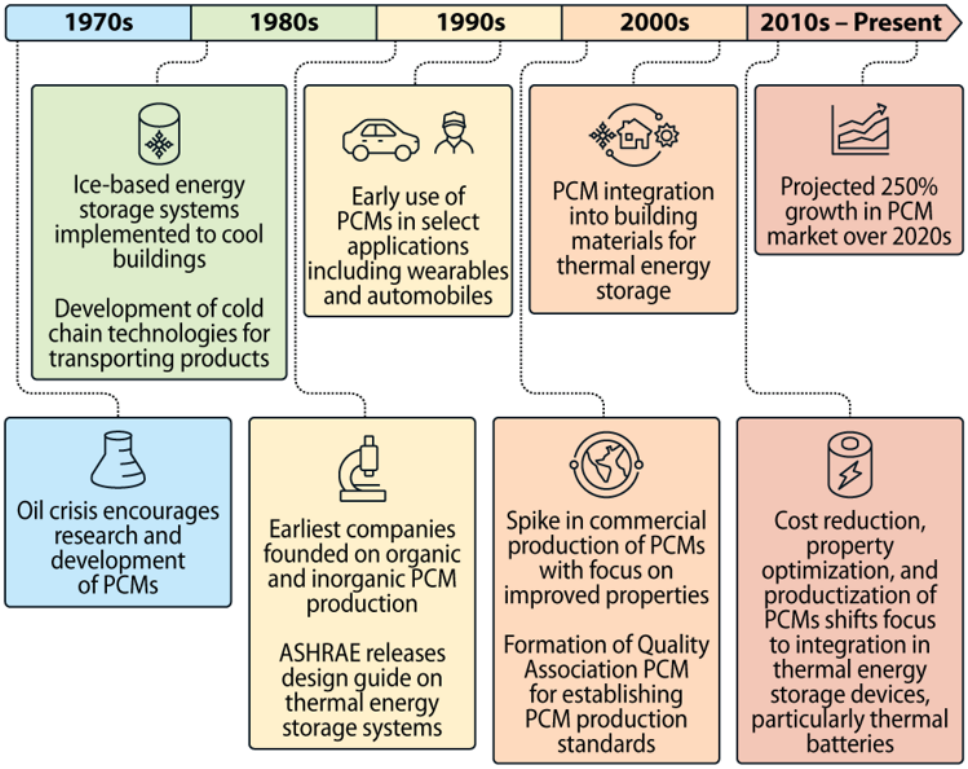

Figure 1.8 Graphical timeline displaying major events in the commercialization of PCM and PCM-integrated products.

lutions [311], Pluss Advanced Technologies [312], PureTemp [313], Rubitherm [314], Sasol Limited [315], Sunamp [316], and Tempered Entropy [317]. While PCMs have an extensive history of application research, the transition to commercially available products has been somewhat limited. Reasons for lack of industrial adoption include cost as well as limitations in thermal conductivity, latent heat, and charging/discharging, though these properties have experienced significant improvement over the last few decades. PCMs have traditionally been most successfully incorporated into thermal management devices for cooling electronics and in cold chain applications for temperature-controlled transportation of goods.

1.5.2 Water-Based Systems

Historically, ice has been the most used PCM given its abundance and low cost relative to other PCMs. Water-based systems have been implemented across

different geographies over the last few decades. This technology aims to store thermal energy in large-scale ice tanks that can be stored indoors or outdoors. The ice then undergoes solid-to-liquid phase change at times of need for building space cooling, typically through a secondary loop flowing a glycol-water solution. Companies like Baltimore Aircoil [318], Calmac [319], and Evapco [320] produce ice-based thermal storage systems that aim to reduce greenhouse gas emissions and save money on cooling costs in commercial buildings such as schools, hospitals, malls, and more.

1.5.3 PCMs for Heating Applications

Due to advancements in material properties and cost reductions, PCMs are now being used for thermal energy storage in both water and air heating applications. For example, in addition to manufacturing and selling their own PCM under the Plentigrade tradename, Sunamp develops TES devices utilizing PCMs for heating water and air. Sunamp claims their Thermino thermal battery can be charged by air-source heat pumps, ground-source heat pumps, photovoltaics, grid electricity and boilers [321]. Phase Change Solutions manufactures a wide range of biobased PCMs, some of which remain solid through their phase transition temperature. In addition to these products, Phase Change Solutions also offers a device named ENRG that is reported to save a 25,000 ft^2 facility 81,000 kWh of energy annually. This "blanket" consists of PCM placed between two polymer and/or aluminum films that can be placed in the ceilings, roofs, or walls for load shaving/shifting and thermal buffering [322]. Axiotherm produces both organic and inorganic PCMs across a wide range of temperatures, as well as products incorporating their macroencapsulated PCMs into both water-based (HeatSel) [323] and air-based (HeatStraxx) [324] energy storage devices. Ephex markets and sells a total PCM-integrated system for water heating applications [325]. This system utilizes solar panels that collect thermal energy during the day and then uses flowing

water beneath the panels to transfer the energy to a salt based PCM thermal battery located near the facility's hot water tank. The tank then pulls thermal energy from the battery at times of need to meet domestic hot water needs of the facility. PCM Technology manufactures floor/ceiling panels that integrate PCM for heating and cooling for both homes and office spaces, in addition to PCM-based solutions to cooling data centers and improving energy efficiency [326].

1.5.4 PCMs for Cooling Applications

In cooling applications, PCM are used to produce cold packs for transporting food, pharmaceuticals, temperature-based therapies, for cooling electronics, and for air-conditioning in buildings. In this space, Cold Chain Technologies produces low phase transition temperature PCM gel and foam packs for use in keeping products cold during shipping [327]. Similarly, Sonoco encapsulates low temperature PureTemp PCM gel within metal-lined bagging to produce cold packs [328]. Several companies also produce smaller portable coolers that incorporate either ice packs or PCM-lined walls, which are intended for everyday consumer use. In electronics cooling, AllCell's Phase Change Composite technology absorbs and conducts heat away from lithium-ion batteries for increased power density and battery life [329]. Advanced Cooling Technologies has produced PCM-integrated heat sinks that are utilized in military and aerospace applications, specifically to replace complex thermal management systems already implemented. These devices utilize thermal modeling coupled with advanced manufacturing to develop optimal geometries for high performance heat sinks [326]. Viking Cold is another company that combines intelligent controls and monitoring software in conjunction with PCM thermal batteries to provide cold chain solutions to food transport and long-term storage. These batteries utilize PCM in the range of –28 to 0 ^{o}C that are encapsulated within high density polyethylene (HDPE) packs that Viking Cold claims absorbs 50-85% of heat infiltration into cold storage spaces [330]. PLUSS Technologies develops both

hydrated salt and organic PCMs, in addition to several products utilizing these materials. These products include a solar-powered cold-room (HimaCool) and a portable freezer (PronGO) that implement cold storage thermal batteries to maintain setpoint temperatures [331].

1.5.5 Wearable Technology

Wearable technology that incorporates PCMs for thermal management of the human body has seen considerable research in recent years, with several products reaching the market. For instance, GlacierTek develops PCM-integrated cooling vests that utilize PureTemp's materials [332], while Inuteq produces a similar cooling wearable technology that uses materials from CrodaTherm [333]. Both products use macroencapsulated PCM as a means of pulling heat away from the body, which can improve performance in athletics or for safety in certain professions such as firefighting or nursing where overheating can occur. For sleeping applications, Outlast Technologies GmbH produces composite polyester fibers blended with PCMs called ThermoCules that can be utilized in comforters and sleeping bags for keeping bodies thermally comfortable during rest [334]. In a similar application, companies such as Rubitherm have produced sheets filled with PCMs for wearing during heat therapeutic treatments [335].

1.5.6 Thermally Conductive Scaffolds

Several companies are investigating ways of producing thermally conductive structures via advanced manufacturing that can serve as scaffolds for PCM-integrated thermal batteries. The most common method of producing thermally conductive scaffolds is through metal printing. Several companies manufacture 3D printers capable of 3D printing metal, which, listed alphabetically, include 3D Systems, Desktop Metal, Digital Metal, EOS, Fabrisonic, Formalloy, GE Additive, Markforged, Pollen AM, Renishaw, SLM Solutions, SPEE3D, TRIDITIVE, TRUMPF, Velo3d, Xact Metal, and XJet. These systems largely rely on laser sin-

tering of metal powder that fuses together particles and forms a solid structure, though some like Markforged's Metal X printer use a metal-infused polymer filament that is printed normally and then placed in a kiln to burn off any non-metal components and fuse the metal particles together. However, these printing methods can often be cost prohibitive, with printers from the above-mentioned manufacturers costing anywhere between $100k-$750k, in addition to necessary add-ons like furnaces for sintering. Outside of metal printing, TCPoly is a company that manufacturers polymer filament with a thermal conductivity of 5.0-8.0 W/mK, which is about 20x greater than that of neat polymeric materials [336]. These polymer composites are not as thermally conductive as metal-based materials, but they are comparatively cheaper, use more accessible equipment to print, corrosion resistant, and require no post processing steps. With either technology, scaffolds can be backfilled with a variety of PCMs and encapsulated, allowing for applications to thermal battery systems that require rapid charging/discharging.

1.6 Perspective on Future Directions

There are many potential applications of PCMs - ranging from heating and cooling equipment to thermal management of electronic devices. Each application will have its own constraints, which will impact how the PCM should be integrated. In devices used for heating and cooling, PCM TES incorporation allows for load shifting and peak shaving, reducing stress on the electrical grid and facilitating renewables integration. Certain power electronic equipment is highly transient and requires pulse heat dissipation. A heat sink, or thermal management device, made of PCM can absorb large heat spikes while maintaining a constant temperature.

Additive manufacturing for thermal management systems utilizing PCM allows for the development of novel, thermally conductive scaffolding that cannot be produced by subtractive manufacturing. As mentioned previously, several companies are beginning to use metal 3D printing to make structures for PCM-integrated

thermal batteries. Furthermore, technology to directly print relatively high conductivity composite PCM and polymer composites is emerging. One of the main advantages of the ability to 3D print heat sinks (particularly extrusion-based) is in situations where fast, easy, cost-effective manufacturing is necessary, such as the ability to manufacture replacement parts on demand while away from fabrication facilities (e.g., while in orbit in space or in a field location).

Currently, commercial TES, which allows for peak shaving and load shifting, results in energy and cost savings for businesses. However, the widespread adoption of TES, including extension to residential customers, will further aid in reducing the demand on the aging and unstable electrical grid. TES can be extended to manage waste-heat and waste-cool recovery, further enhancing the energy and cost-savings benefits. It is expected that advanced manufacturing will play an important role in advancing the design of the heat exchanger form for TES systems.

The current state-of-the-art of many latent heat TES systems is large PCM-filled tanks with immersed heat exchanger tubing with length scales on the order of 10-40 mm, see Figure 1.9. Since in many lower-temperature HVAC-type applications the PCM is water, expansion and contraction during the phase change has historically, due to both mechanical stresses and the ability to maintain contact between the water/ice and the heat exchanger surfaces, prevented smaller channels and PCM length scales from being utilized for more effective heat exchanger designs. However, with the advent of utilizing newer, higher-energy-density, cost-effective PCMs (with lower coefficients of expansion), the design of next-generation thermal energy storage units can take advantage of additive manufacturing processes to produce compact heat exchangers with very high surface-area-to-volume (length scales on the order of 1-3 mm, see Figure1.9) that incorporate novel heat-transfer-enhancing elements, such as complex fins or flow geometries, not possible with traditional manufacturing. In addition to manufacturing novel geometrical

features, additive manufacturing precipitates the use of alternative heat exchanger construction materials, such as composite polymers comprising PCM or thermal-conductivity-enhancing additives.

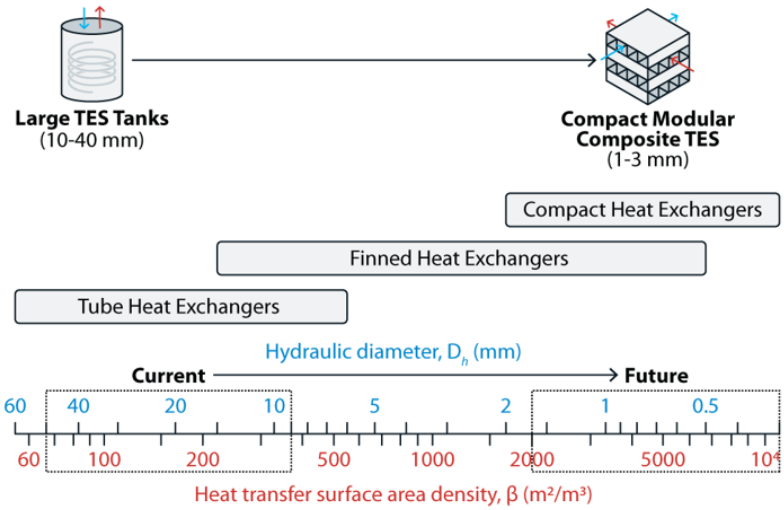

Figure 1.9 Vision for the future of TES heat exchangers with respect to magnitude of length scales and surface-area-to-volume ratios.

Currently, there is a dearth in PCMs with high energy density and phase-change temperatures in room-temperature range for building applications as seen in Figure 1.10. Although water has an energy density of 92 kWh/m^3, exceeding the BTO target of 80 kWh/m^3, alternative eco-friendly materials with higher phase-change temperatures are needed. Salt-hydrate-based PCMs are promising; however, remedies for supercooling and separation issues continue to be explored by researchers. Furthermore, innovation in advanced manufacturing techniques is needed to incorporate salt-hydrate-based PCMs into composite 3D printing.

For additively manufactured TES to become competitive with traditional manufacturing techniques, the ability to scale-up the technology from small form factors is imperative. Many 3D printers are prohibitively slow and can only produce very small footprints, making large heat exchangers that can be produced quickly nearly impossible. However, as additive manufacturing advances, the ability to pro-

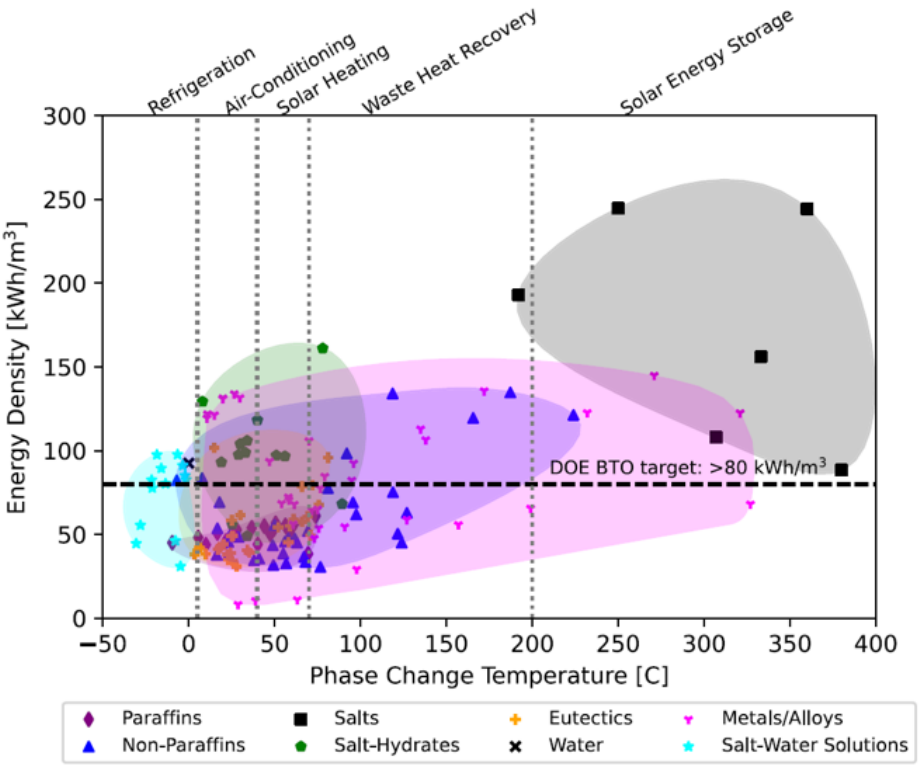

Figure 1.10 Energy density of various PCM categories with applications and DOE BTO target energy density.

duce compact, modular heat exchangers becomes more of a reality.

1.7 Relevent Literature: PCM Modeling

There is a need to decarbonize the growing energy systems in the world to help mitigate the effects of climate change [1]. This requires the rapid development of clean energy solutions such as solar and wind energy to help reduce current and future emissions [2]. To achieve these clean energy solutions, co-deployment of scalable, affordable, and sustainable energy storage technologies need to be explored [3]. Several methods of storing large quantities of energy have been developed at different levels of readiness and their own set of pros and cons [4–7]. Thermal energy storage (TES) systems are of great interest due to the low cost and reliability. Materials used for TES can be classified into three categories: sensible heat, latent heat via phase change, and thermochemical reactions. Authors have presented com-

parisons as well as advantages and disadvantages of sensible [8], latent [9, 10], and thermochemical energy storage materials [11–13]. Of the three energy storage material categories, latent heat via phase change has become the area of interest in TES research. To properly design and implement latent heat TES systems, the phase change materials (PCMs) need to be modeled properly and effectively.

When it comes to modeling PCMs, more specifically understanding the mathematics of a moving boundary separating two different phases of a material, this work began in the 1800's. The first known instance of these types of problem sets was by Lame and Clapeyron in 1831[337], shortly followed by a lecture from Neumann on moving boundary problems[338], and lastly a series of papers by Stefan in the late 1800's[339, 340] that is now famously referred to as the Stefan problems. Due to the time period of these discoveries, only simplified closed form analytical solutions were developed due to the lack of numerical computational capabilities.

It wasn't until the 1970's, when the Neumann-Lame-Clapeyron-Stefan Problems could be revisited with the intention of using numerical solutions to further advance these problem sets. This first known numerical work was done by researchers Bonacina et al.[341], Meyer[342], and Shamsundar and Sparrow[343, 344]. From these works, the handling of the phase change process was done using conduction as the primary form of heat transfer throughout the solid and liquid phase of the PCM. In 1977, Sparrow et al. concluded that the natural convection that occurs in the liquid region of the phase change could not be ignored and has a significant impact on the interactions at the phase boundary between the solid and liquid regions[345]. This conclusion was further emphasized and proven since then by various researchers performing numerical calculations and experiments [346–352].

From the countless work done over the past decades, the modeling of phase change processes are handled numerically by various techniques and methods[353, 354]. One of the main and most important assumptions made to determine which

method to use when modeling a PCM is to decide if natural convection within the liquid region can be neglected or not. In many scenarios, natural convection is neglected to help reduce computational intensity despite enough evidence to believe that natural convection would be present and significant within the PCM. Improper use of the assumption on natural convection can lead to large error in the modeling of PCM.

The most appropriate time to neglect the effects of natural convection and model the PCM only with conduction, is when the PCM is shape-stabilized. A shape-stabilized PCM, is a PCM that is formed into a composite material that maintains its overall shape while the PCM undergoes a phase change from a solid to liquid phase. A PCM can be shape-stabilized by being mixed with a polymer (HDPE [200, 201], PCL [233], TPU [225, 249], ABS [241, 248, 255], Nylon [204]) or impregnated into and expanded porous material (expanded graphite [355–357], metal foam [358–360], polymer foam [361]). With these shape-stable PCMs, the effects of natural convection are greatly reduced as the large liquid region that forms during a phase change process is broken up into smaller micro cavities. This reduction in natural convection effects causes conduction to be the primary form of heat transfer during the melting process [362, 363]. Therefore, the use of a conduction based modeling method, like the enthalpy method is very appropriate when used for shape-stabilized PCMs.

When modeling a phase change process with a heat transfer fluid to exchange energy with the PCM, a major assumption is made to estimate the heat transfer coefficient at the heat transfer boundary. In the literature, a heat transfer coefficient is estimated by using correlations available for constant wall temperature and constant wall heat flux boundary conditions [364–369]. None of the correlations used account for the dynamic transient effects at the boundary when the melt front of the PCM is moving. In the present study, a closer examination of the coupled re-

lationship between the transient melting of a shape-stabilized PCM and the forced convection of a heat transfer fluid is explored and a comparison is made with heat transfer coefficients from the literature.

2 HDPE/PCM Composite Filament

In this chapter, the fabrication and characterization of a composite PCM filament was developed for fused filament fabrication (FFF). The filament consist of the composition of high density polyethylene (HDPE) with an organic PCM (PureTemp) through the use of a single screw extruder. Characterization includes thermal storage capacity and thermal conductivity of both the filament and 3D printed samples. The contents of this chapter contributed to the publication in the Journal of Additive Manufacturing [205].

2.1 Materials and Manufacturing Methods

2.1.1 Materials

HDPE pellets (PPR-HDPE01) with a specific gravity of 0.955 and a melt flow rate of 20 g/10 min (190 °C and 2.16 kg) were supplied from Premier Plastic Resins (Lake Orion, MI). The PCM, PureTemp 42 (henceforth known as PCM42), was supplied from PureTemp (Minneapolis, MN). The data sheet from PureTemp reports that PCM42 has a phase-change temperature of 42 °C and latent heat of fusion (h_{sl}) of 218 kJ/kg. The latent heat of fusion is the energy absorbed or released during a constant-temperature phase change from a solid to a liquid.The data sheet provided by the manufacturer also reports that when PCM42 is in the solid phase, it has a density (ρ) equal to 940 kg/m^3 and a thermal conductivity (k) equal to 0.25 W/mK. When PCM42 is in the liquid phase, it has a density equal to 850 kg/m^3 and a thermal conductivity equal to 0.15 W/mK.

2.1.2 Filament Fabrication

Mixtures of HDPE and PCM42 were prepared by pre-melting and mixing the two materials together for specific mass ratios. The thermal storage capacity correlates to the PCM percentage within the composite; however, too much PCM content can diminish the structural integrity. The mass content of the PCM42 in the mixture was varied between 20% and 60%, in increments of 10%, in order to deter-

mine the maximum amount of PCM42 that can be mixed with HDPE to produce filament suitable for FFF. The mixtures were observed for consistency of filament diameter during the extrusion process and their ability to remain flexible enough for printing (i.e., could physically be handled without breaking). If the percentage of PCM42 in the mixture was too high, then an inconsistent diameter was observed during the process, and the resultant filament would break easily when handled. It was found that the 40% PCM42 mixture contained the maximum amount of PCM while still maintaining the criteria for printable filament; therefore, this composition is the focus of the current study. The DSC was used to examine the filament by testing the latent heats of fusion and melt temperatures of both the PCM42 and the HDPE in the composite. As will be discussed later, the DSC results were also used to hypothesize the amount of PCM loss due to the extrusion process (e.g., leaking).

The PCM42/HDPE mixture was pelletized using a shredder (SHR3D IT, 3devo, Utrecht, Netherlands) and extruded into 1.75-mm-diameter functional composite filament using a filament extruder (Next 1.0, 3devo, Utrecht, Netherlands) with a 4-mm-diameter nozzle. The extruder has four equally spaced independent heating elements and a single screw to help promote better mixing. At the nozzle outlet of the extruder, there are two adjustable directional fans for air cooling. During the extrusion process, the filament diameter was affected by a number of factors, such as the cleanliness of the extruder screw, heating element temperatures, the speed of the screw, and nozzle diameter. Therefore, an initial set of experiments was conducted to optimize the extruder settings for pure HDPE and the PCM42/HDPE composite. The heater temperatures, screw speed, and filament diameter were monitored throughout each extrusion process. Filament with a consistent diameter for FFF is compared to that with an inconsistent diameter in Figure 2.1. Consistent-diameter filament was produced using optimal settings

(discussed below) after starting with an extruder that had been purged with specialized cleaning materials (HDPE Flush, Devoclean Purge, 3devo, Utrecht, Netherlands). Inconsistent-diameter filament typically arose from any combination of not using optimal settings, starting with an uncleaned extruder screw, and/or too much PCM42 in the mixture (discussed earlier). As a reference, the filament diameter of pure HDPE and the composite was measured over a ten-minute time period, as shown in Figure 2.2. The composite had slightly more variance in filament diameter than pure HDPE, which could cause inconsistencies within the print, but was still useable for FFF purposes.

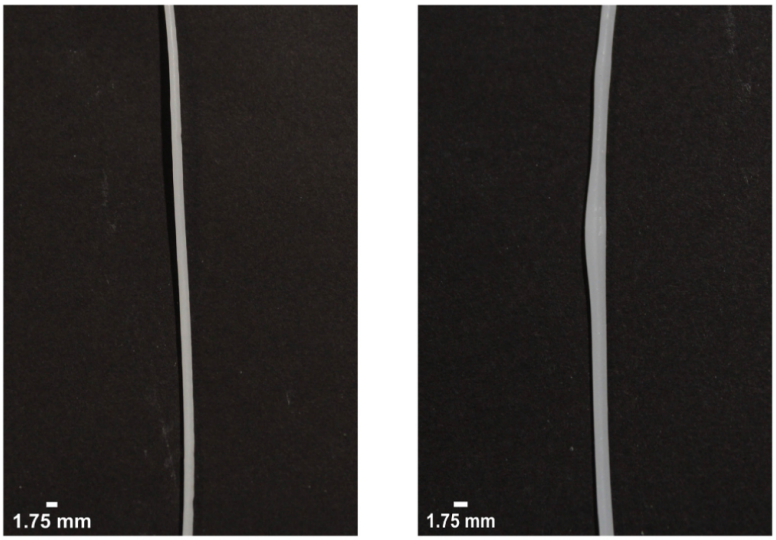

Figure 2.1 Comparison of filament with (a) a consistent diameter and (b) an inconsistent diameter.

Common extrusion practice requires a balance between the temperature of the material and flow through the nozzle. The amount of PCM content can affect the settings required to produce the desired filament diameter. Heater temperatures were kept between 170 and 210 °C to ensure the filament properly melted, but did not burn, and screw speeds were set between 3 and 6 RPM to adequately move material. Adjustments were made based on the analysis of the filament di-

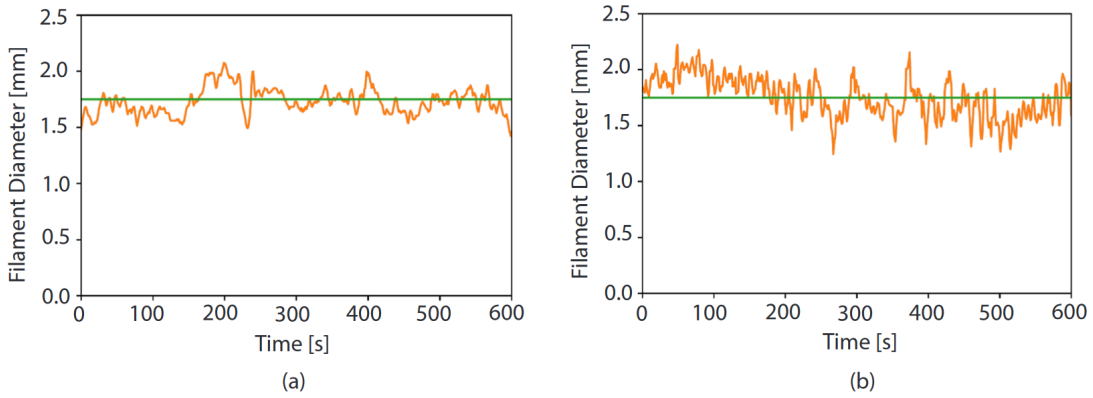

Figure 2.2 Filament diameter, utilizing optimum settings and a clean extruder screw, versus time for (a) pure HDPE and (b) the PCM42/HDPE composite.

ameter. From this analysis, the settings that produced the most consistent filament diameters for pure HDPE and the composite studied here are shown in Figure 2.3, which conveys the screw speed, heater temperatures, and nozzle diameter. Due to the incorporation of PCM42, the composite settings are ideal at the lower heater temperatures (190 °C) and screw speed (4 RPM), whereas the pure HDPE extrudes best at the higher ranges (200 °C and 5 RPM). Additional factors, such as blockages within the extruder and heavy directional cooling (from the cooling fans), can influence the consistency and shape of the filament. From the optimal parameters provided, the settings can be altered further depending on the response of the material at the specific time of extrusion.

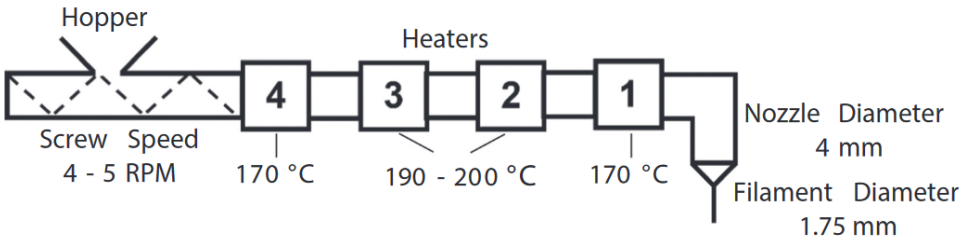

Figure 2.3 Optimal extruder settings for pure HDPE (200 °C and 5 RPM) and the PCM42/HDPE composite (190 °C and 4 RPM).

2.1.3 Additive Manufacturing

Pure HDPE and shape-stabilized PCM42/HDPE composite samples were 3D printed using a MakerGear M3-ID (Beachwood, OH) with Gcode sliced using Simplify3D software. The print settings are shown in Table 2.1, and the general pathing of the G-code for the samples is shown in Figure 2.4. When printing HDPE using FFF, adhesion and detachment is difficult due to the high shrinkage of the material. Schirmeister et al. [57] evaluated several types of build plates for use in printing HDPE, and good adhesion was found either using SEBS (Kraton FG1901 G) or roughened HDPE. However, they found that detachment from the heated SEBS build plate was much easier than from the heated roughened HDPE build plate. In both instances,the build plate was heated to a temperature of 60 °C.

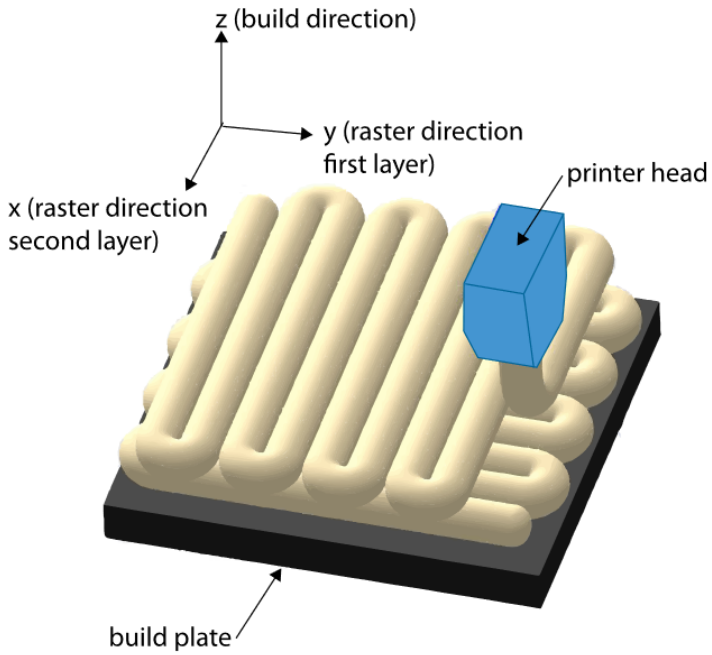

Figure 2.4 Schematic diagram of the material deposition process.

In the current study, a heated HDPE build plate was also used; however, a smooth build plate provided excellent adhesion with minimal curling for pure HDPE filament, so roughening or a SEBS build plate was not necessary. Delamination between the layers and curling was observed during the printing of larger

Table 2.1 Print Settings

Setting	Value
Nozzle Diameter	0.35 mm
Nozzle Temperature	240 °C
First Layer Height	0.18 mm
Layer Thickness	0.20 mm
Line Width	0.42 mm
Fill Percentage	100%
Material Flow	1.00
Build-Plate Temperature	60 °C
Filling Pattern	Lines, 45°Offset Alternating
First Layer Printing Speed	550 mm/min
Printing Speed	1100 mm/min

HDPE samples, as seen in Figure 2.5. The delamination and subsequent curling was caused by the temperature disparity between the extruded material (240 °C) and the ambient printing environment (25 °C). Similar problems have been described by Choi et al. [61] when printing with ABS. Choi et al. [370] noted that as the build-plate temperature increased, print results near the build plate improved; however, layers farther away from the build plate still showed delamination. To mitigate the delamination issue in the print farther away from the heated build plate, an elevated-temperature environment, similar to Zawaski and Williams [371], was implemented(see Figure 2.6). Successful printing was observed for heated-environment temperatures between 60 °C and 65 °C. The elevated temperature significantly improved the bonding of the layers and reduced curling and delamination, thereby reducing the frequency of failed prints.

Although the heated HDPE build plate was successful in promoting good adhesion, the print became difficult to remove since the first layer was fused to the build plate.In the present study, initial prints resulted in the bottom of each sample being destroyed during the removal process. Therefore, a design modification was implemented to resolve this issue by simply adding extra depth to the sample disks, and, when required, the final surface was sanded until a desired surface finish

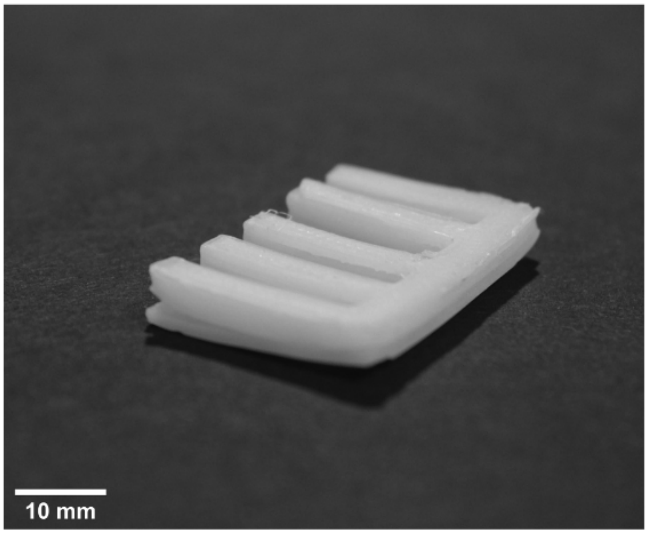

Figure 2.5 Curling causing layer separation and delamination of a print sample prior to implementation of the heated build environment.

and/or dimension was attained.

It was found that the shape-stabilized functional composite prints had noticeably less curling and were easier to remove from the build plate than pure HDPE prints, which suggests that the PCM reduced the effect of these issues. Any printing problems with the composite typically stemmed from inconsistent filament quality or issues introduced by the heated enclosure, which caused either obstructions in the nozzle or under-extrusion of the sample. These issues were resolved by visually screening the filament before use and increasing the material flow when the diameter was significantly below the nominal 1.75mm.

In the heated environment, the composite feedstock would become slick with PCM since the ambient temperature inside of the heated enclosure was greater than the phase-change temperature (42 °C). Despite the aforementioned difficulties, multiple disk samples (25-mm diameter and 4-mm thick) were successfully printed, which can be seen in Figure 2.7(a) and 2.7(b). The slick filament occasionally created extruder clogs, but a slower print speed reduced the frequency of this issue.

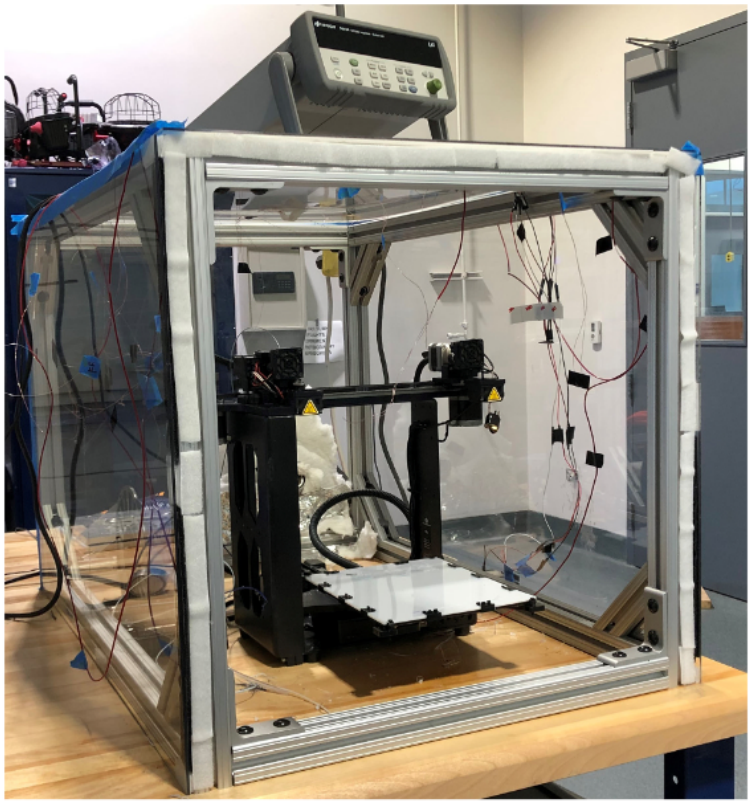

Figure 2.6 3D printer enclosed in an elevated-temperature environment.

2.1.4 Molding of Bulk Samples

A custom machined mold was used to create the bulk material samples used as the baseline for the thermal characteristics of the printed samples. The bulk material samples were made to have the same dimensions as the 3D printed samples. The PCM 42/HDPE composite filament, pure HDPE, and pure PCM42 were melted down and compression molded into 25-mm-diameter and 4-mm-thick disks. Processing temperatures for the pure HDPE and composite were around 200 °C. Resultant molded samples for both the HDPE and the composite are shown in Figures 2.7(c) and 2.7(d).

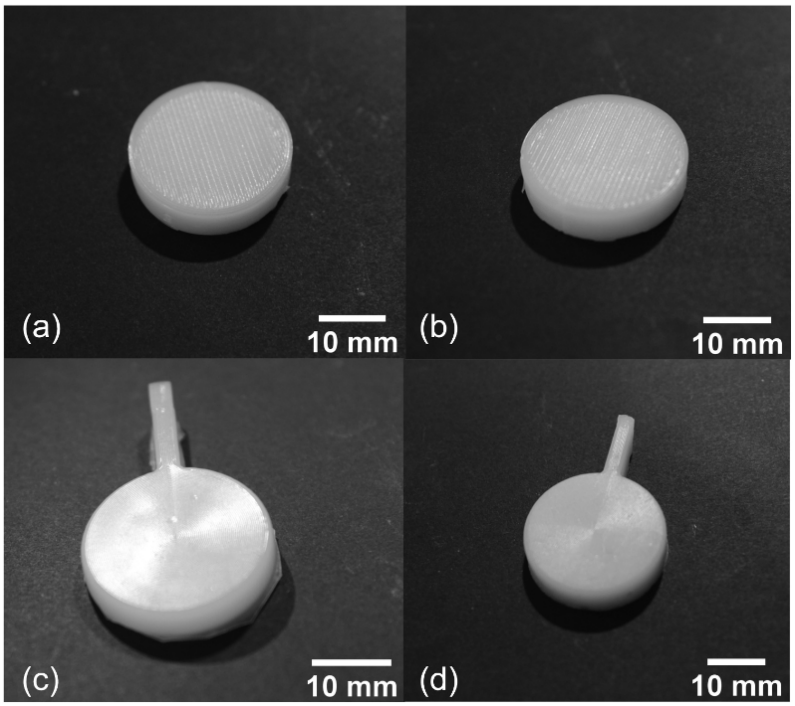

Figure 2.7 Images of the samples (25-mm diameter and 4-mm thick) showing (a) printed HDPE, (b) printed PCM42/HDPE composite, (c) molded HDPE, and (d) molded PCM42/HDPE composite.

2.2 Experimental Methods

2.2.1 Differential Scanning Calorimetry

The latent heat of fusion and phase-change temperature of the PCM42/HDPE composite filament was measured using a DSC (DSC 3 STARe, Mettler Toldeo, Columbus, OH). The masses of five random samples from the filament were measured using a balance (XS105DU, Mettler Toledo, Columbus, OH). The samples,ranging in mass between6 and 18mg, were placed in 40-μl aluminum crucibles. The temperature of each sample was initially held at 10 °C for 10min and then heated from 10 to 200 °C at 2 °C/min. Each sample was held at 200 °C for 10min and then cooled at 2 °C/min until it reached a temperature of 10 °C. Temperature and heatflow were recorded every one second. The heating and cooling cycle was performed at least two times because each sample needed to be melted down once to make good thermal contact with the bottom of the crucible before the actual measurement.

Since PCM42 is not a pure substance,the phase change happens over a range of temperatures and not just over a single temperature (as is observed in a pure substance). The melting temperature range of the composite was calculated based upon the onset and endset temperatures from the heatflow versus temperature graph as shown in Figure 2.8. The onset and endset temperatures are the temperatures where the material begins and ends the melting phase, respectively. These temperatures are defined as the intersections of the inflectional tangents of the leading and trailing edges of the peak and the extrapolated tangent of the baseline. The latent heat of fusion is calculated by the area under the peak of the heatflow versus time curve.

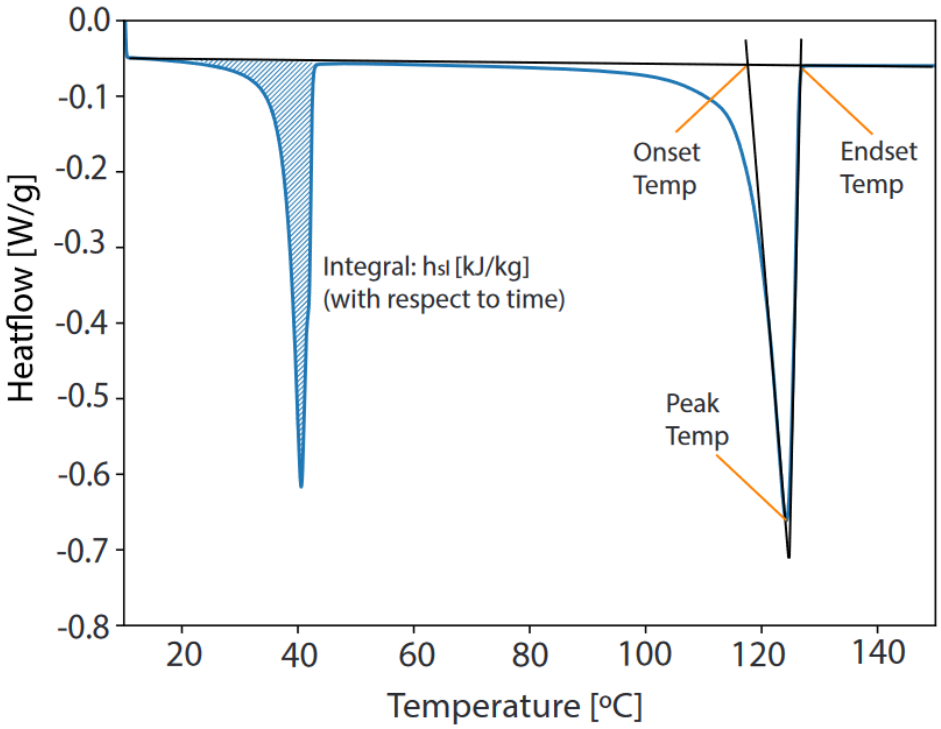

Figure 2.8 Heat flow versus temperature diagram illustrating latent heat of fusion, onset, endset, and peak temperatures. The first peak represents the PCM42 phase change and the second peak represents the HDPE phase change.

2.2.2 Thermal Conductivity Measurements

A thermal constants analyzer (Transient Plane Source (TPS) 2500S, Hot Disk, Gothenburg, Sweden) was used to measure the thermal conductivity of the PCM42/HDPE composite bulk material and the printed samples. The isotropic module with a 4-mm-diameter Kapton sensor (C7577, Hot Disk, Gothenburg,Sweden), which includes both a resistive heater and a temperature sensor, was used. The sensor was sandwiched between two matching 25-mm-diameter and 4-mm-thick samples made of the same material and identically manufactured (see Figure 2.9). Joule heating was applied, which produced a dynamic temperature field in the sample and sensor. The temperature response of the sensor was monitored, and the thermal conductivity of the sample was determined from a model. A power of 50mW and time of 10s was used. For statistical significance, ten tests were performed for each sample to obtain an average thermal conductivity and standard deviation.

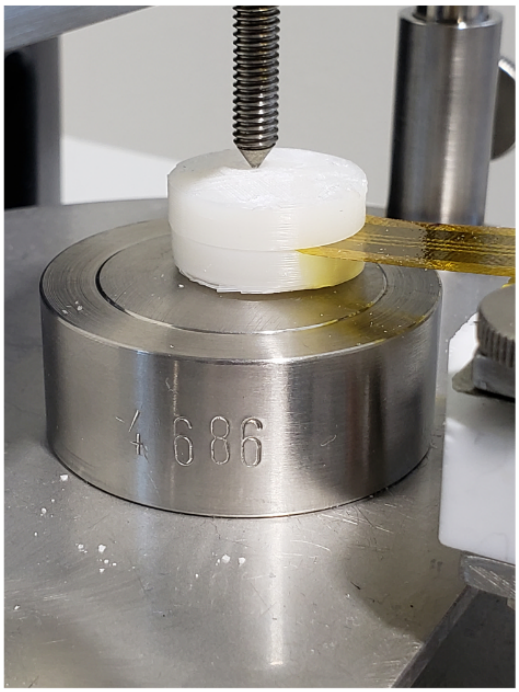

Figure 2.9 Hot Disk TPS operation setup. The Kapton sensor is sandwiched between two bulk PCM42/HDPE composite samples.

Table 2.2 Phase-change temperature and latent heat of fusion of the PCM42/HDPE composite filament.

	PCM42				HDPE			
	Tpeak (°C)	Tonset (°C)	Tendset (°C)	$h_{sl}(kJ/kg)$	Tpeak (°C)	Tonset (°C)	Tendset (°C)	hsl (kJ/kg)
Pure	44.47	40.36	46.28	200.00	133.33	125.95	136.75	191.68
Sample 1	40.70	37.67	42.51	59.94	124.59	118.38	126.54	116.42
Sample 2	40.58	37.68	42.49	60.02	124.50	118.66	126.37	118.27
Sample 3	40.55	37.63	42.43	62.68	124.43	118.36	126.39	123.30
Sample 4	40.61	37.61	42.48	63.28	124.44	118.41	126.50	122.91
Sample 5	40.58	37.82	42.66	72.40	123.78	117.79	126.67	117.87
Sample Average	40.60	37.68	42.51	63.66	124.35	118.32	126.29	119.75
Sample St.D	0.06	0.08	0.09	5.11	0.32	0.32	0.36	3.14

2.3 Microscopy

The microstructures of the PCM42/HDPE composite filament and resultant prints were visualized using a scanning electron microscope (SEM, Quanta 650, ThermoFisher Scientific, Hillsboro, OR). To allow for high-vacuum setting used for visualization, the samples were coated in gold (Sputter Coater 108, Cressington Scientific Instruments, Watford, UK). An accelerating voltage between 15kV and 20kV was used, and the vacuum pressure was between 3.5 and 8 × 10 6 Torr. To observe the cross section of the filament and printed samples, liquid nitrogen was used to freeze the samples before shattering.

2.4 Results and Discussion

2.4.1 Phase-Change Temperature and Latent Heat of Fusion

The PCM42/HDPE composite filament was extruded and samples were taken from five randomly selected regions throughout the extrusion process. Results are shown in Table 2.2 for each of the five samples that were tested in the DSC to measure the average and standard deviation of the phase-change peak temperature (T_{peak}), onset temperature (T_{onset}), and endset temperature (T_{endset}). Values of the five samples and the standard deviation show that the material composition is fairly consistent.

The phase-change peaks for pure PCM42, pure HDPE, and the composite filament are shown in Figure 2.10. In the figure, the first peak represents the phase change of PCM42 around 42 °C, and the second peak represents the phase change

of the HDPE around 130 °C. Effective latent heats of fusion (h_{sl}) for both the PCM42 and HDPE in the composite were also calculated by integrating the area under the peaks with respect to time in Figure 2.10. Baseline samples for pure PCM42 and pure HDPE are represented in the table as Pure.

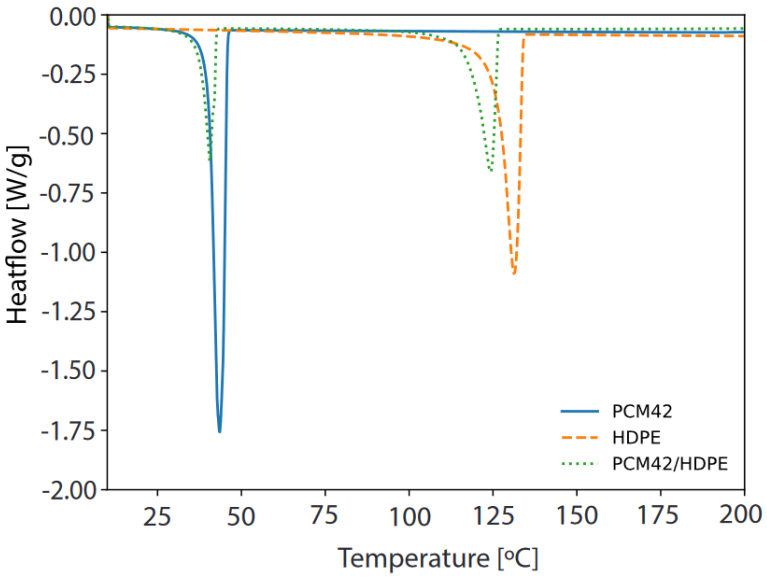

Figure 2.10 Heatflow versus temperature for pure PCM42, pure HDPE, and the PCM42/HDPE composite filament.

The latent heat of fusion for the pure PCM42 is approximately 9% lower than the published value of the manufacturer,which is 218 kJ/kg. It is interesting to note that the latent heats of fusion for both the pure PCM42 and the pure HDPE are very close in value, where the HDPE latent heat of fusion is approximately 5% less than the PCM42 value. Based upon the results in Table 2.2, the composite filament has an average effective h_{sl} for PCM42 of 63.66 kJ/kg. This value is only 31.8% of the latent heat of fusion of 200.00 kJ/kg for pure PCM42. It is hypothesized that if there is 40% of the PCM42in the filament, the effective h_{sl} should be 40% of 200 kJ/kg, which is 80 kJ/kg. The difference between the true value and the hypothesized value may be due to multiple factors, such as material loss during the mixing and extrusion processes involved in the fabrication of the composite filament, the

chemistry of mixing the materials, or a combination of both. Regardless, the thermal energy storage capability of the composite filament effectively acts as if there is 31.8% of the pure PCM42 in the composite.

According to the results(Table 2.2 and Figure 2.10), the composite filament causes the peak, onset, and endset temperatures to decrease. The peak melting temperature for pure PCM42 is 44.47 °C, compared to the average peak melting temperature of 40.60 °C for the PCM42 in the composite. An even greater decrease in melt temperature for the HDPE in the composite is observed, with pure HDPE having a peak melting temperature of 133.33 °C, and the HDPE in the composite having an average peak melting temperature of 124.35 °C. This phenomenon can help explain why the composite required lower temperatures during the extrusion process as compared to the extrusion temperatures of the pure HDPE (see Figure 2.3).

2.4.2 Thermal Conductivity

Each sample was measured ten times to determine an average thermal conductivity (k) and standard deviation, and the results can be seen in Table 2.3. Figure 2.11 displays the information in a bar graph for comparison purposes. In the figure, the error bars represent the standard deviation. The pure PCM42 does not have a print value due to the inability to print pure PCM42 without a shape stabilizer. Based upon the results,it can be seen that pure HDPE and pure PCM42 in their bulk forms have a measured thermal conductivity of 0.576 W/mK and 0.276 W/mK, respectively. The thermal conductivity value for pure PCM42 is 10.4% higher than the values provided by the manufacturer, which is 0.25W/mK. The thermal conductivity of the molded bulk PCM42/HDPE composite was measured to be 0.413 W/mK. This value corresponds to a 28.3% decrease in the original thermal conductivity of the HDPE, which shows that the addition of the PCM42 mixed into the HDPE causes the overall thermal conductivity to be lower than the value

Table 2.3 Thermal conductivity (average of each sample measured ten times) of the molded and printed samples.

Sample	k [W/mK]	St.D
Bulk Pure HDPE	0.576	0.001
Bulk PCM42/HDPE Composite	0.413	0.013
Bulk Pure PCM42	0.276	0.005
Printed Pure HDPE	0.435	0.026
Printed PCM42/HDPE Composite	0.365	0.024

of pure HDPE.

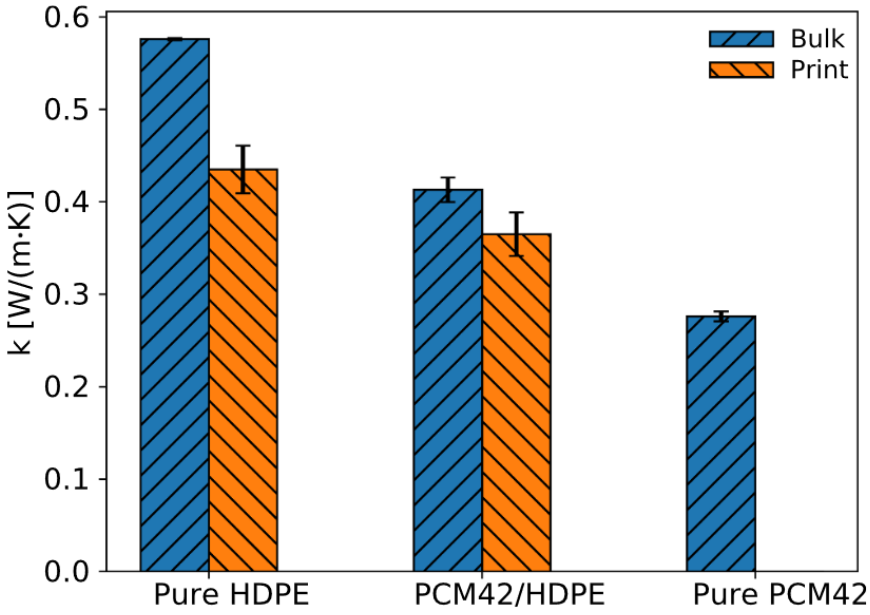

Figure 2.11 Thermal conductivity (average of each sample measured ten times) of the molded and printed samples. The error bars represent the standard deviation.

The printed pure HDPE and printed PCM42/HDPE composite were measured to have thermal conductivities of 0.435 W/mK and 0.365 W/mK, respectively. These values are noticeably lower than the respective thermal conductivities of the bulk materials. The reason that the printed materials have a lower thermal conductivity than their bulk counterparts is because of the air gaps that are formed within the printed part from the actual printing process. The small air gaps cause thermal contact resistance between the layers. Based upon the current state

of FFF, air gaps within the printed part will always be present, although some recent efforts have been made to reduce this effect [275, 277]. The thermal conductivity of the printed part will change based upon the size and quantity of these air gaps, which are highly dependent on print settings. The printed HDPE was 24.5% lower than that of the bulk value, and the printed composite was 11.6% lower than the bulk composite. The smaller difference in thermal conductivity between the bulk and printed composite compared to the pure HDPE bulk and printed samples may be due to PCM42 filling in the air gaps during the printing process. Evidence of this is shown in the microstructure visualization results.

Another reason for the decrease in thermal conductivity for the printed material may come from the surface quality of the printed part versus that of a molded version of the same material. Similar to the reasons for why the air gaps are formed within the material, the FFF process results in a poor surface finish depending upon the printing parameters. A poor surface finish leads to poor thermal contact with the respective heating source (Kapton sensor) used to make the measurement, which inherently lowers the overall measured thermal conductivity. Without any post processing,such as sanding,the printed samples had a noticeably rougher surface finish than the molded samples, which can be seen in Figure 2.7.

2.5 Microstructure Visualization

A cross-sectional view of the extruded PCM42/HDPE composite filament (before FFF) is shown in Figure 2.12. Figure 2.12(a) shows the filament with the edge visible,and Figure 2.12(b) shows a closer view of the center of the filament. Microstructure images of the pure materials are shown to be clearly differentiated in [200, 203] where pure extruded HDPE has a platelet-like structure, and PCM42 has a cloud-like structure. In Figure 2.12, the structure of the HDPE is clearly seen with the PCM encapsulated in between the platelets. Based upon visual inspection, the mixing of the two materials appears to have produced homogeneous filament.

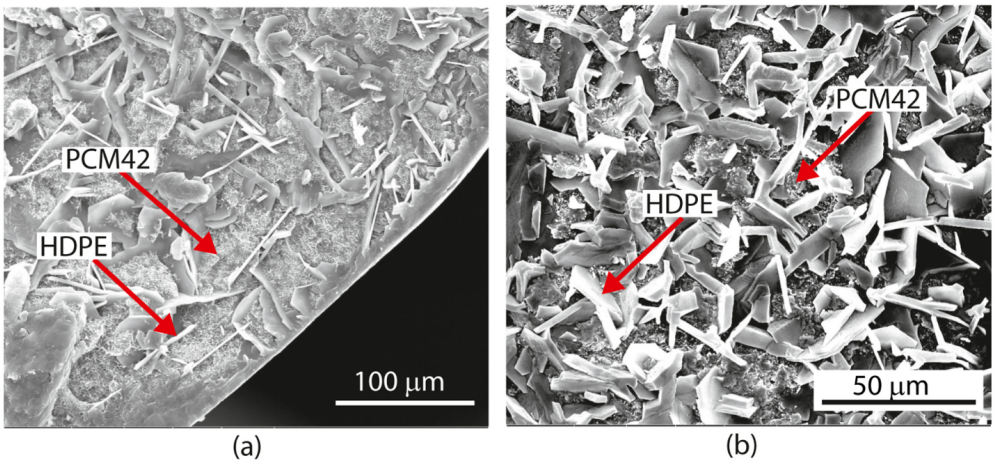

Figure 2.12 PCM42/HDPE composite filament (a) scale bar 100 μm and (b) scale bar 50 μm.

The fracture surface (cross-sectional view) of both the composite and pure HDPE printed samples at different magnifications can be seen in Figure 2.13. While Figure 2.13(a) and 2.13(b) show the printed composite for different magnifications, Figure 2.13(c) and 2.13(d) show the printed pure HDPE for corresponding similar magnifications. It is interesting that the composite material retained its basic microstructures(as seen in Figure 2.12) after the second extrusion of the material during the FFF process.

Also in Figure 2.13, the print directions and print patterns can be clearly observed, and noticeable air gaps, formed by the printing process between parallel beads of material, can be seen. Despite having an infill percentage of 100% for both samples, small air gaps are still present within the printed material. The air gaps are one of the main reasons for the reduction in thermal conductivity in the printed samples when compared to the bulk material thermal conductivity. The presence of air gaps causes a decrease in thermal contact from one layer to the next, therefore causing a decrease in overall thermal conductivity. As the amount and size of small air gaps increases for a given print, the thermal conductivity is expected to also decrease.

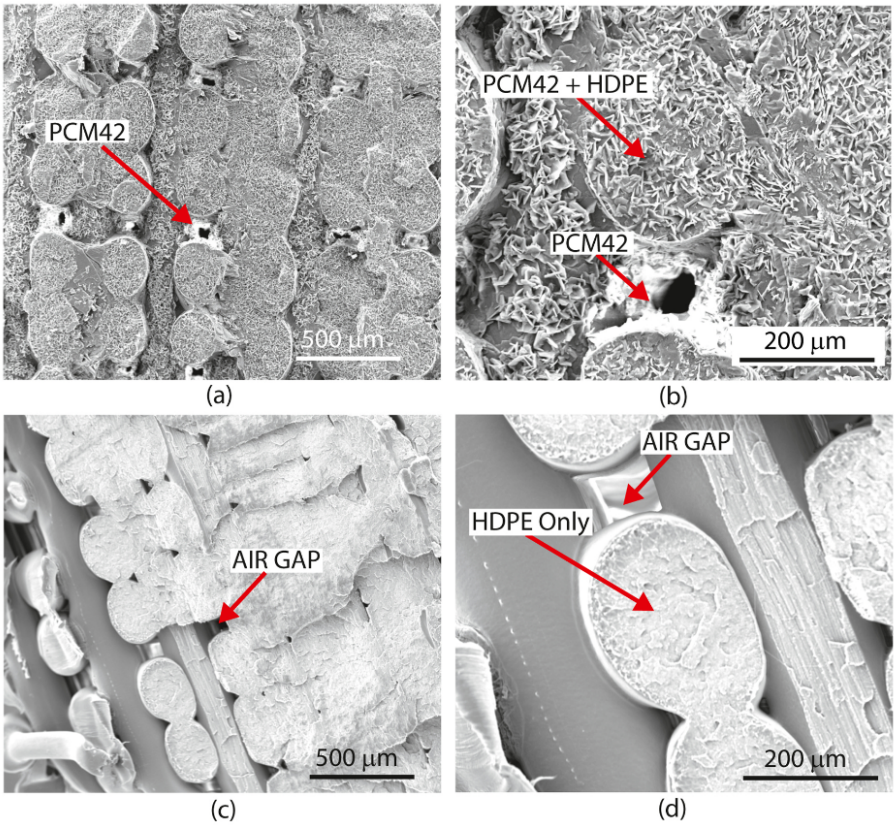

Figure 2.13 Printed samples (a) PCM42/HDPE composite scale bar 500 μm, (b) PCM42/HDPE composite scale bar 200 μm, (c) HDPE scale bar 500 μm, and (d) HDPE scale bar 200 μm.

It can be observed in Figure 2.13(a) and 2.13(b), that when the composite filament is printed, the air gaps becomepartially filled with PCM42.This leads to a reduction in air-gap size, which in turn leads to less of a decrease in thermal conductivity. The air gaps formed when printing pure HDPE can be seen in Figure 2.13(c) and 2.13(d), and when compared to the printed composite, appear to be more prominent. The relative effect of the air gaps can also be observed in Figure 2.11, which shows that the difference in thermal conductivity between the bulk material and the printed material is greater for the pure HDPE than it is for the composite.

3 Moisture affinity of HDPE/PCM composites

In this chapter, the further characterization of the HDPE/PCM composite is performed to characterize the materials moisture affinity. Characterization includes the steady-state and transient adsorption and desorption of the composite material, along with the the base constituents that comprise of the composite. The adsorption and desorption characterization of a material helps with the understanding of a materials response when exposed to humid environments. The work in this chapter contributed to the publication in the Royal Society of Chemistry Advances Journal [202].

3.1 Sample Preparation

PureTemp 42 (PureTemp, Minneapolis, MN), an organic PCM which changes phase at 42 °C and has a latent heat of fusion of 218 kJ/kg, was heated and mixed with HDPE (PPR-HDPE01, Premier Plastics Resins, Lake Orion, MI). A mixture of 50% PureTemp 42 and 50% HDPE by mass (50/50) was prepared. The mixture was then formed into pellets utilizing a shredder (SHR3D IT, 3devo, Utrecht, Netherlands). The pellets were then fed into the hopper of a filament extruder (next 1.0, 3devo, Utrecht, Netherlands) to fabricate 1.75 mm diameter filament.

3.2 Microscopy

Filament samples were frozen using liquid nitrogen and then subsequently shattered to examine the interior of the filament. The samples were gold coated (Sputter Coater 108, Cressington Scientific Instruments, Watford, UK) for visualizing with a scanning electron microscope (SEM, Quanta 650, ThermoFisher Scientific, Hillsboro, OR).

Figure 3.1 shows SEM images of the extruded filament containing HDPE and PureTemp 42. Prior work examined the microstructures of both pure HDPE and pure PureTemp 42 [12,13]. The platelet-like structure of the HDPE is clearly seen with the lattice-like structure of the PCM embedded in between the platelets.

Upon visual inspection of Figure 3.1 and other similar SEM images, the dispersion of PCM appears to be homogeneous.

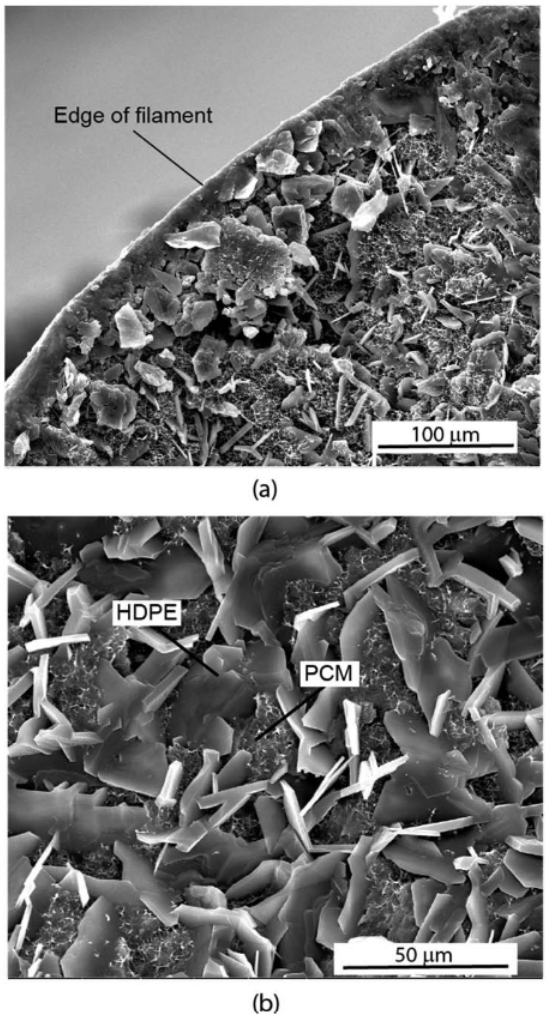

Figure 3.1 Microstructure visualization of HDPE with PureTemp 42 (50% PCM by mass) at 25 °C (a) image showing edge of filament, and (b) view showing HDPE (platelet-like structures) and PCM (lattice-like structures).

3.3 Dynamic Vapor Sorption

Both equilibrium (steady-state) and transient adsorption and desorption behaviour of the materials are important to characterize the affinity of water. While the steady-state isotherms establish the total moisture adsorption capacity, the diffusion coefficient determines the response of the material (i.e., how quickly water can be adsorbed or desorbed). A dynamic vapor sorption apparatus (DVS Advan-

tage, Surface Measurement System, UK) has been used to conduct the steady-state and transient experiments [14,15].

Figure 3.2 shows the DVS experimental setup. The relative humidity is controlled by mixing wet and dry nitrogen gas (N_2). A vapor sensor is used to measure the relative humidity. Water vapor, with a known concentration, flows over a sample that is suspended from an ultra-fine microbalance, which is used to measure the change in weight of the sample due to adsorption or desorption of the vapor molecules. The sample mass for various experiments varied between 1–3 mg. It is worth noting that regardless of the variation of dry sample mass, the percentage in mass is an indication of potential for moisture for various samples and provides the relative comparison independent of the sample mass.

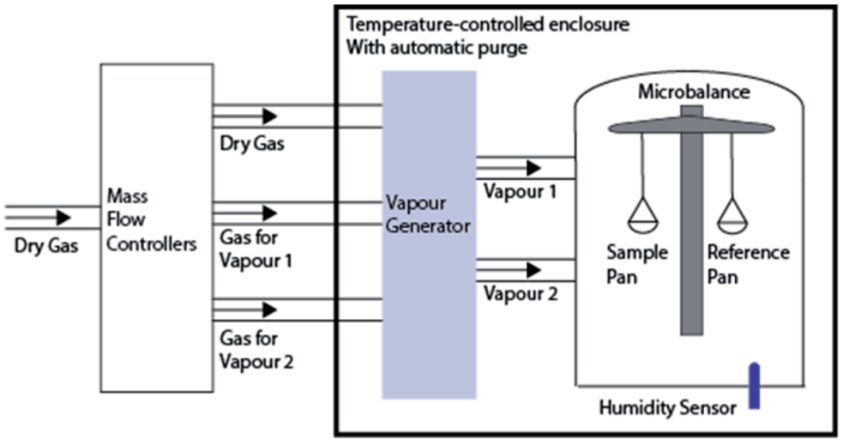

Figure 3.2 Components of the experimental setup.

Temperature is an important factor for moisture adsorption and desorption potential. Prior studies have shown that, in general, the moisture adsorption capacity of the material increases with temperature while the response time decreases, indicating higher diffusion coefficients [372].

In the current study, the samples were suddenly exposed to a dry or humid environment and the weight change due to moisture adsorption and desorption was measured as a function of time. The data was then used to calculate the steady-

state capacity and diffusion coefficients.

3.4 Steady-State Adsorption/Desorption Capacity

Steady-state experiments have been conducted to investigate the moisture adsorption capacity of the materials. The experimental procedure is presented in Figure 3.3. A sample, with a known initial mass, is exposed to a series of moisture levels, and the change-in-mass response is recorded. The experiments are conducted for both adsorption and desorption modes for a set temperature. The entire process is repeated for various temperatures, and the steady-state mass gain at respective humidity conditions is recorded to establish the moisture adsorption/desorption isotherms at specified temperatures. The relative error in measurement is less than 1 mg. The average variation in relative humidity and temperature is noted as ± 1% and ± 0.25 °C, respectively. Prior to the beginning of the test, each sample was exposed to a completely dry-air condition (0% RH) for sufficient time to ensure that the sample had no initial moisture content at the beginning of the test. The same drying test has been repeated for different temperatures.

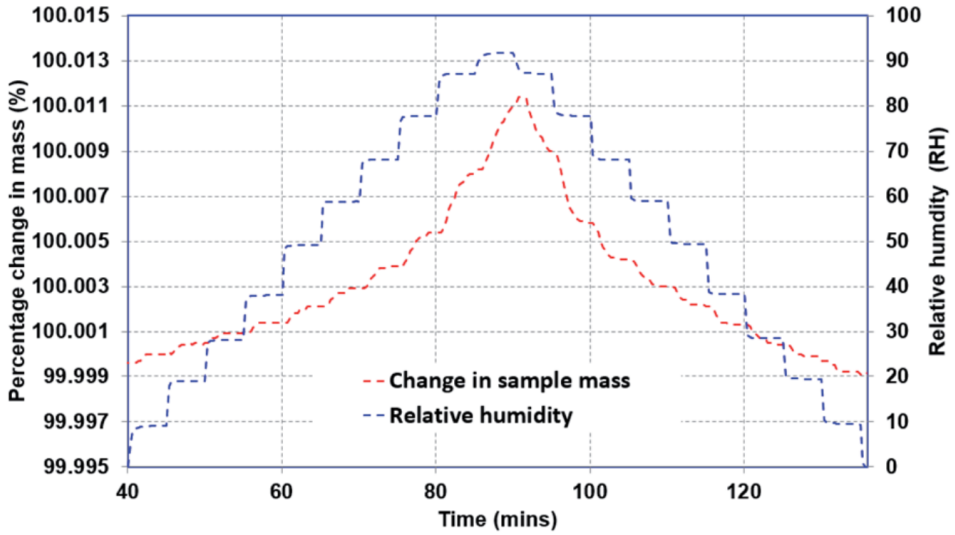

Figure 3.3 Experimental procedure to establish adsorption/desorption isotherms.

3.5 Transient Adsorption/Desorption Analysis

The transient response of the sample is established by evaluating the time response of the sample when the ambient moisture content is changed as a step function, and the mass of the sample continues to change until it reaches the steady-state condition. Two types of experiments were performed: (i) small incremental change in moisture content (10%), and (ii) large incremental change in moisture content (70% and 90%). Figure 3.4 presents representative data for the second type of test. As can be noted, the relative humidity in the chamber was increased from 0% to 90% and then decreased back to 0%. Once the sample was completely dry, another cycle with 70% RH was initiated.

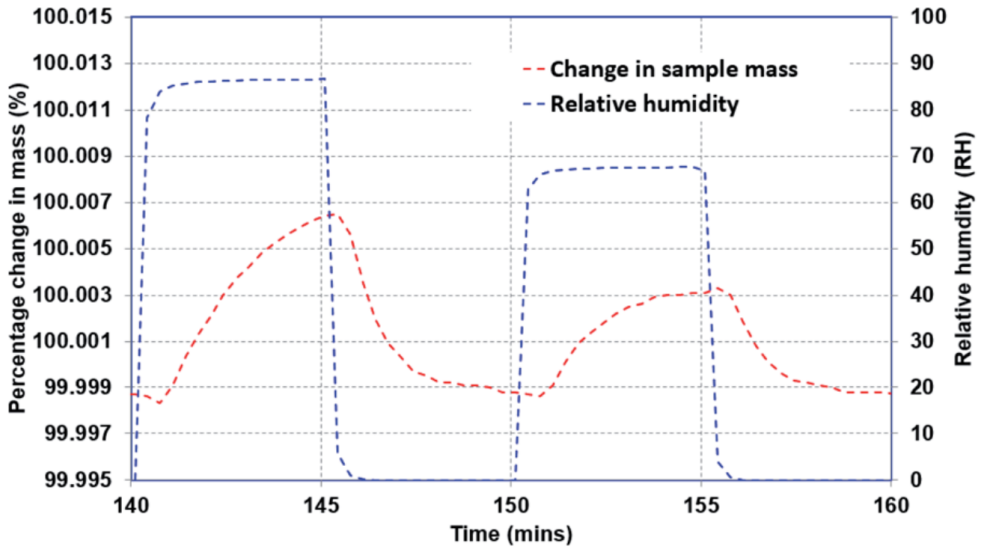

Figure 3.4 Transient experimental procedure to establish the diffusion coefficients.

The one-dimensional transient diffusion equation can be solved to extract the bulk diffusion coefficients (Equation 4.1) for the samples under consideration using appropriate initial and boundary conditions (Equation 4.2). The diffusion coefficient is obtained by curve fitting the solution while minimizing the error in predicted and measured values [14,15].

$$\frac{\partial \rho}{\partial t} = D\left(\frac{\partial^2 \rho}{\partial r^2} + \frac{1}{r}\frac{\partial \rho}{\partial r}\right) \tag{3.1}$$

Initial and boundary conditions.

$$\rho(r, t = 0) = 0 \tag{3.2a}$$

$$\rho(r = 1, t) = \rho_\infty \tag{3.2b}$$

$$\frac{\partial \rho}{\partial r}(r = 0, t) = 0 \tag{3.2c}$$

3.6 Results and Discussion

Samples of HDPE, PureTemp 42, and a 50/50 (by mass) composition were prepared and subjected to the experimental procedures outlined in the preceding sections. The steady-state isothermal experiments were performed for multiple temperature settings (25, 35, and 45 °C). For pure PCM and the composite sample, the 45 °C experiments were excluded since the melting temperature for PCM is 42 °C. Figures 3.5 - 3.7 show the adsorption and desorption isotherms for pure PCM, HDPE, and the composite sample, respectively. It also can be noted that the relative hysteresis is negligible except at relatively higher humidity values, and the capacity is increased slightly with increase in temperature for both types of materials.

The most important observation is the total capacity. Pure PCM can adsorb about 30% more moisture at higher humidity values. Similarly, the composite samples adsorb almost twice the amount of moisture adsorbed by the pure materials, which can be explained in terms of potential voids created during the mixing process. Regardless, the overall change in the sample mass is negligible due to a very small amount of moisture adsorption. It is concluded that the material has very little affinity for moisture.

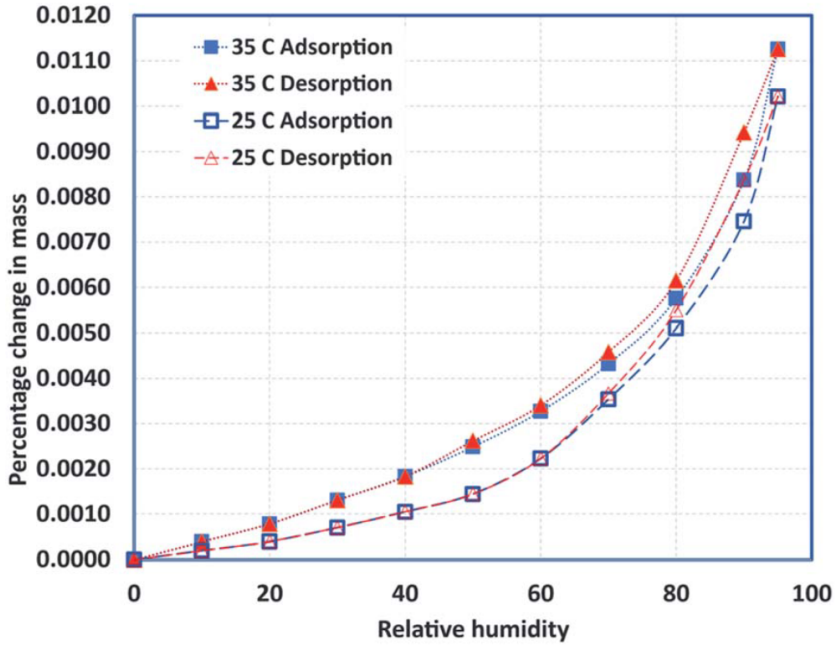

Figure 3.5 Adsorption/desorption isotherms for pure PCM at 25 and 35 °C.

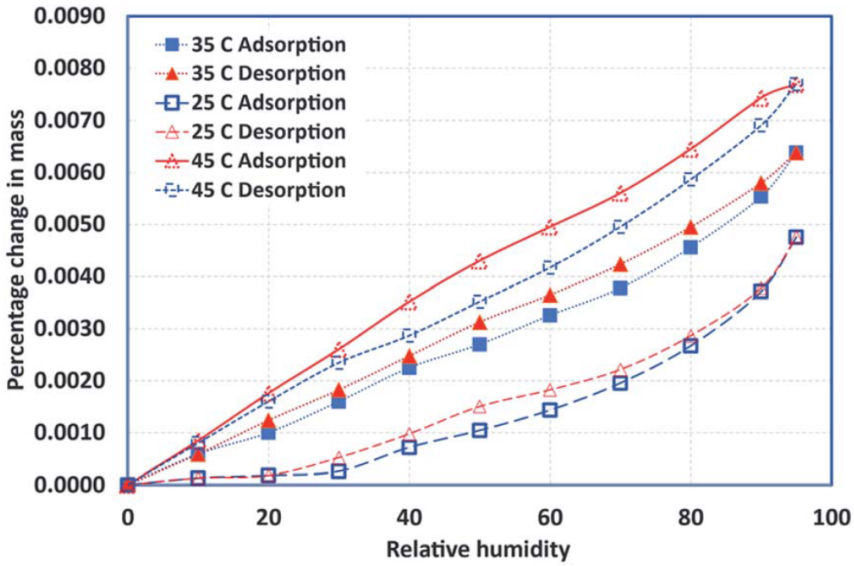

Figure 3.6 Adsorption/desorption isotherms for pure HDPE at 25, 35, and 45 °C.

The transient performance of the samples has been established in terms of bulk diffusion coefficients, as shown in Table 3.1. The diffusivity is determined for both the adsorption and desorption processes to observe any noticeable differences in the mechanism. Also, the temperature of the operation has been varied to estab-

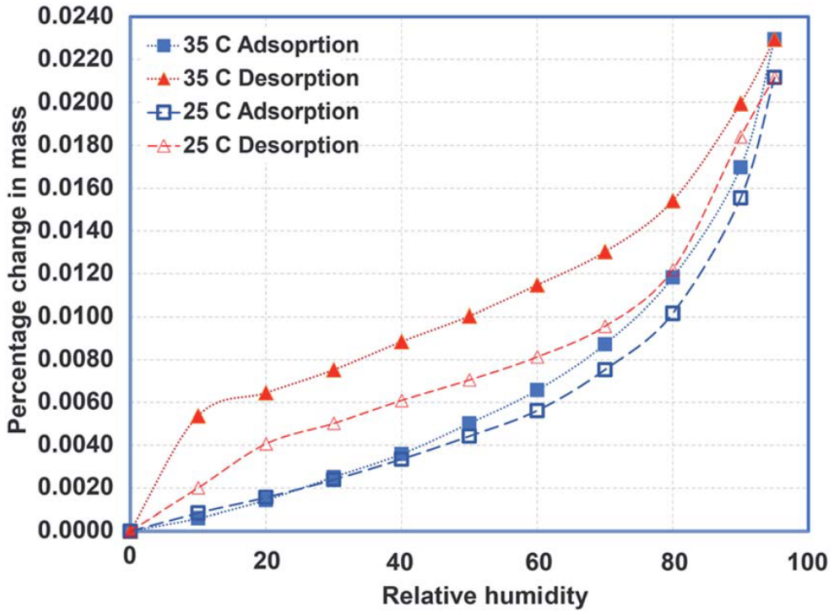

Figure 3.7 Adsorption/desorption isotherms for 50/50 composite at 25 and 35 °C.

lish the impact of temperature. As with the steady-state experiments, the 45 °C temperature was not reported for pure PCM and the composite sample since the PCM starts melting at 42 °C. Based on the established values (± 5% uncertainty), it can be concluded that relative moisture diffusivity for pure PCM and the composite (50/50 by mass) is around 10 and 3 times higher, respectively, compared to the pure HDPE. Furthermore, the mass diffusivity for moisture is independent of adsorption or desorption processes as well as the temperature. The relatively small variation in predictions can be justified in terms of errors in measurements.

Table 3.1 Adsorption/desorption diffusion coefficients.

Material Composition	Temperature (°C)	Adsorption Diffusivity m^2/s (x10^{-7})	Desorption Diffusivity m^2/s (x10^{-7})
Pure PCM	25	10.12	10.34
	35	11.95	11.19
Pure HDPE	25	1.25	1.29
	35	1.33	1.34
	45	1.45	1.41
50-50% HDPE + PCM	25	4.23	4.12
	35	3.95	3.98

4 Microencapsulated PCM and Thermoplastic Polyurethane Composites

In this chapter, the fabrication and characterization of a new composite filament material comprising of a microencapsulated PCM (MEPCM) and a polymer for 3D printing. This composite material is a new alternative to the work described in Chapter 2. The composite material in this chapter uses a MEPCM where the microcapsules fully encapsulate the PCM and the polymer is used as a binding matrix to combine the microcapsules into a homogoenous material. Characterization of the material includes thermal decomposition, thermal storage capacity, and transition temperatures.

4.1 Characterization of MEPCM-TPU Pellets and Filaments

4.1.1 Raw Materials

The raw materials comprising the MEPCM-TPU Pellets were 80A TPU as the base material with inclusion of 24D microencapsulated PCM (MEPCM) spheres. Scanning electron microscopy (SEM) was used to image the MEPCM shown in Figure 4.1. There was a notable size distribution of particle sizes with some as small as 5 μm.

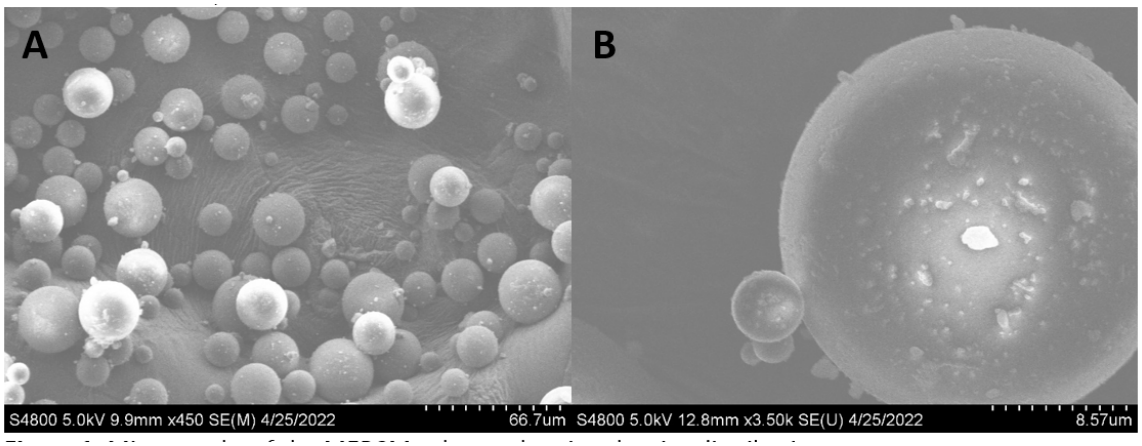

Figure 4.1 Micrographs of the MEPCM spheres showing the size distribution.

Thermal decomposition of the MEPCM and TPU was determined using thermogravimetric analysis (TGA), with decomposition profiles shown in Figure 4.2.

The PCM decomposed rapidly at 407 °C, off-gassing to the extent that the sample exerted a downward force on the pan causing a spike in weight percentage to nearly 150%. Two replicates of PCM were tested to ensure consistency of decomposition and are overlayed in Figure 4.2a. Thermal decomposition of the TPU occurred in two stages indicated by the derivative curve in red with an initial onset of 346 °C.

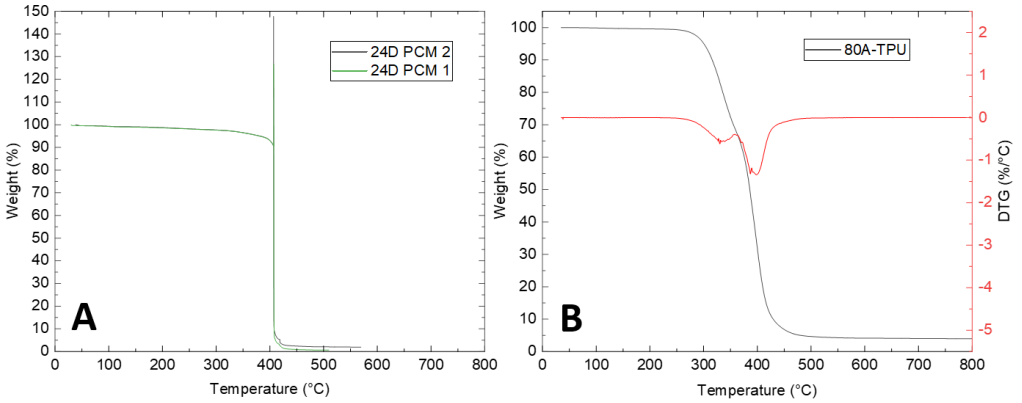

Figure 4.2 Thermal decomposition profiles for (a) MEPCM and (b) 80A TPU

4.1.2 Single Screw Extruded MEPCM-TPU Pellets

MEPCM spheres were compounded with a single screw extrusion process in increments of 20 wt% to achieves 60 wt% and 80 wt% MEPCM in TPU. SEM micrographs of the pellets show the aggregation of MEPCM in the TPU. Figure 4.3a shows the cross section of an extruded pellet and Figure 4.3b shows the density of sphere packing. There was observable damage imparted from the compounding process shown by broken MEPCM shell fragments and surface denting of the spheres in Figure 4.3c and 4.3d, respectively.

Thermal decomposition for both 60 and 80 wt% MEPCM exhibited similar bimodal decomposition as the virgin 80A TPU between 300 and 500 °C and are shown in Figure 4.4. There was mass loss at lower temperatures between 100 and 250 °C which were attributed to volatilization of free paraffin PCM that was liberated from the MEPCM shells during the compounding process.

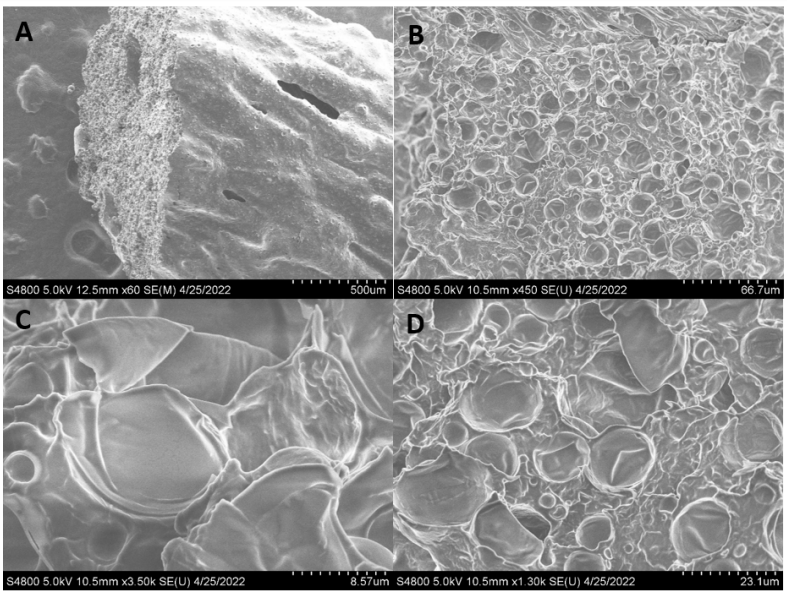

Figure 4.3 SEM micrographs of TPU-MEPCM pellets produced from multiple compounding steps using a single screw extruder. (a) macroscopic image of 60 wt% MEPCM in TPU, (b-d) 80 wt% MEPCM in TPU emphasizing the encapsulated PCM.

Transition properties of the single screw compounded MEPCM-TPU were adversely affected by MEPCM shell breakage but melt enthalpies for the 60 and 80 wt% MEPCM-TPU were 78.2 and 72.3 J/g, respectively. Full results are summarized in Table 4.1. Transition temperatures were not affected, indicating that the PCM was still responsive to temperature changes.

Table 4.1 Summarized Thermal Transition Properties of MEPCM-TPU Pellets

Sample Name	Extrusion Method (# extrusions)	Onset T_m (°C)	ΔH_m (J/g)	Onset T_c (°C)	ΔH_m (J/g)
24D PCM Powder	n/a	19.2	171.3	22.3	169.0
60wt% MEPCM	Single Screw (3x)	19.0 ± 0.2	78.2 ± 9.5	22.4 ± 1.4	72.1 ± 9.0
80 wt% MEPCM	Single Screw (4x)	19.1 ± 0.3	71.3 ± 8.9	22.2 ± 1.5	60.8 ± 8.2
50 wt% MEPCM	Twin Screw (1x)	19.6 ± 0.2	60.7 ± 15.8	22.8 ± 0.1	59.0 ± 15.5
60 wt% MEPCM	Twin Screw (2x)	19.4 ± 0.3	42.5 ± 3.0	22.6 ± 0.2	36.3 ± 2.2

4.1.3 Twin Screw Extruded MEPCM-TPU Pellets

MEPCM-TPU pellets were also produced using a twin screw extruder with one compounding step to achieve 50 and two compounding steps to achieve 60 wt%

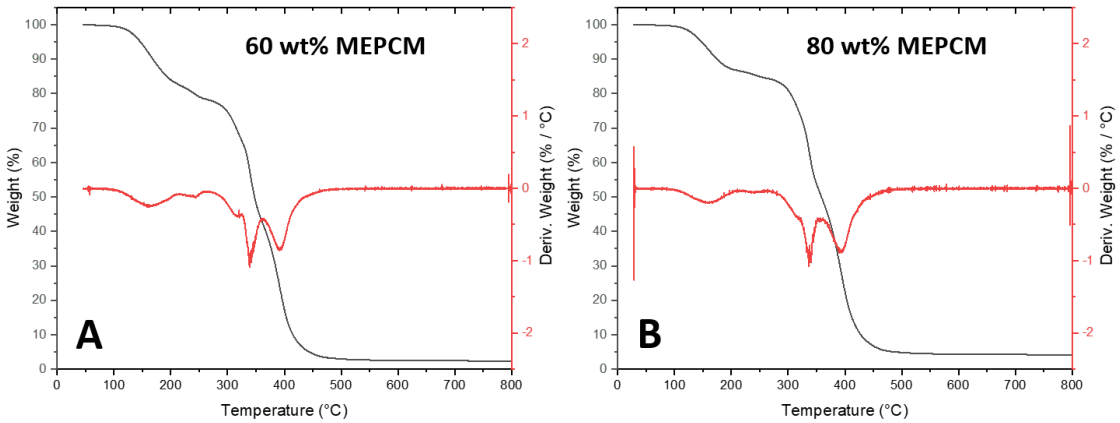

Figure 4.4 Thermal decomposition profiles for (a) 60 wt% MEPCM-TPU and (b) 80 wt% MEPCM-TPU produced from multiple compounding steps using a single screw extruder.

MEPCM to TPU. Reducing the amount of compounding steps led to reduced shell breaking as observed by SEM in Figure 4.5. There was evidence of a pock-marked void structure where MEPCM particles were removed after the fracture of a pellet in Figure 4.5a. The TPU texture was tackier from this process, shown by TPU bridging gaps induced by tensile forces in Figure 4.5b, which was not observed for the single screw extruded processing.

Thermal decomposition of these pellets was similar to the single screw extruded MEPCMs, where there was an initial loss from free PCM in the 100 and 250 °C region followed by the bimodal decomposition of the TPU between 250 and 500 °C. These results in Figure 4.6 indicate that some shell breakage did occur allowing for free paraffin to volatilize from the pellet.

Transition properties of the twin screw compounded MEPCM-TPU are shown in Table 4.1 where transition temperatures were not affected by the compounding process. Notably, across 4 random samplings from the pellets, the 50 wt% MEPCM-TPU appeared to have higher transition enthalpies and higher variability than the 60 wt% MEPCM. The higher variability in the 50 wt% sample was likely from reduced mixing during the extrusion process.

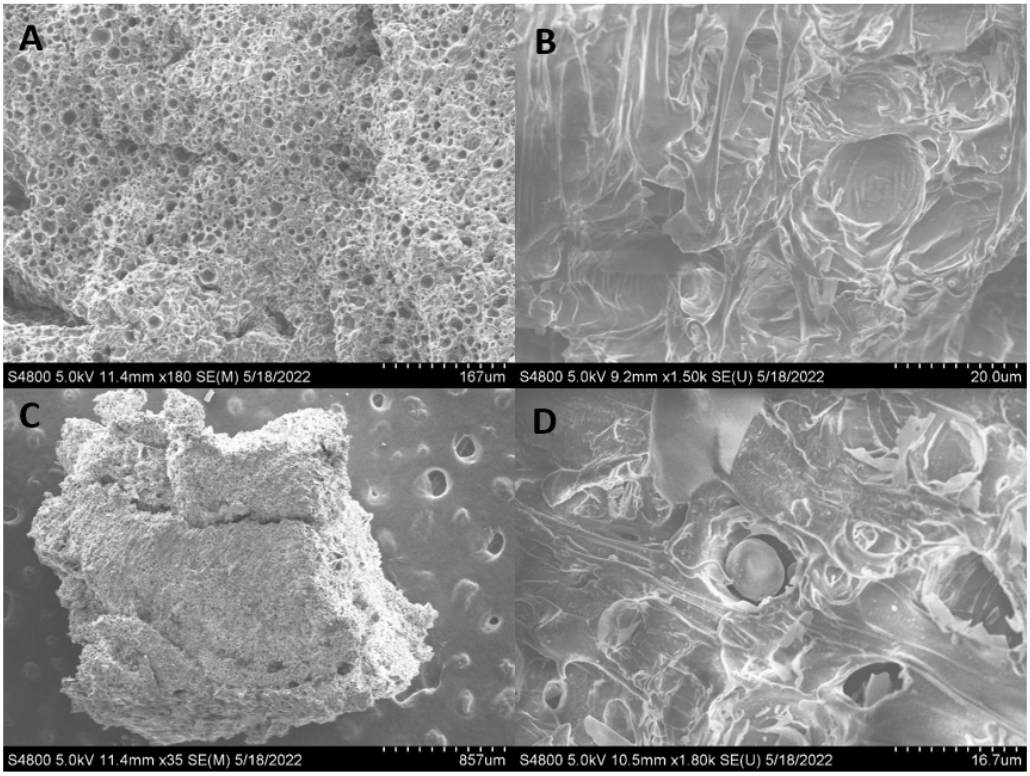

Figure 4.5 SEM micrographs of MEPCM-TPU pellets produced using a twin screw extruder. (a,b) Images of 50 wt% MEPCM in TPU, (c,d) 60 wt% MEPCM in TPU.

4.1.4 Extrusion of MEPCM-TPU pellets into Filament

Compounded MEPCM-TPU from both the single screw (60 and 80 wt%) and the twin screw (50 and 60 wt%) were extruded into 2.85mm diameter filament on a Precision 350 filament extruder (3devo, Utrecht, Netherlands). The Precision 350 extruder is a single screw extruder with four heating stages and a variable speed screw. The extrusion profile chosen can be seen in Figure 4.7.

MEPCM-TPU material was dried at 80 °C for 4 hours before extrusion. Samples of material were taken after the drying period and melt enthalpies were analyzed to determine if any loose PCM is lost in the drying period. Results show there were negligible loss in melt enthalpies from drying. After drying, each weight percentage were extruded only once into 2.85mm diameter filament. At the end of each extrusion, a substantial amount of liquid material was found in the hopper of

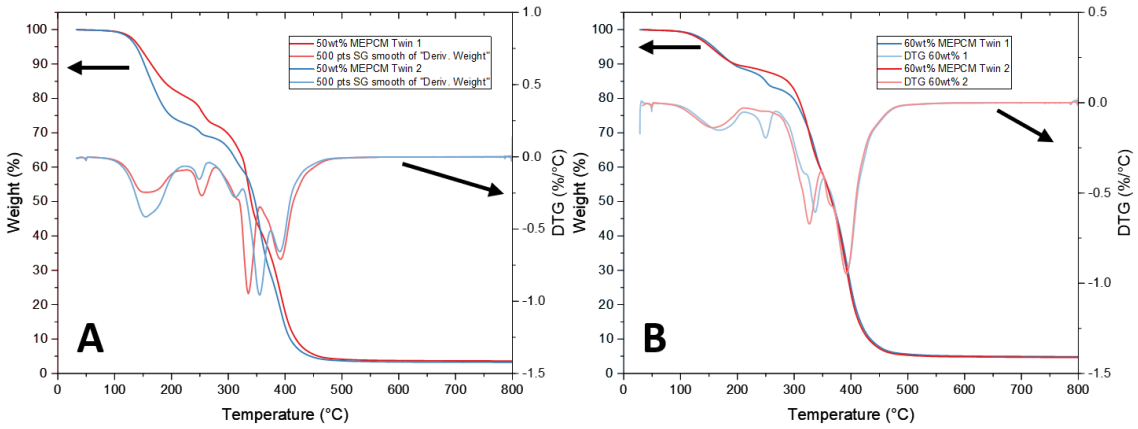

Figure 4.6 Thermal decomposition profiles for (a) 50 wt% MEPCM-TPU and (b) 60 wt% MEPCM-TPU produced from one compounding step using a twin screw extruder.

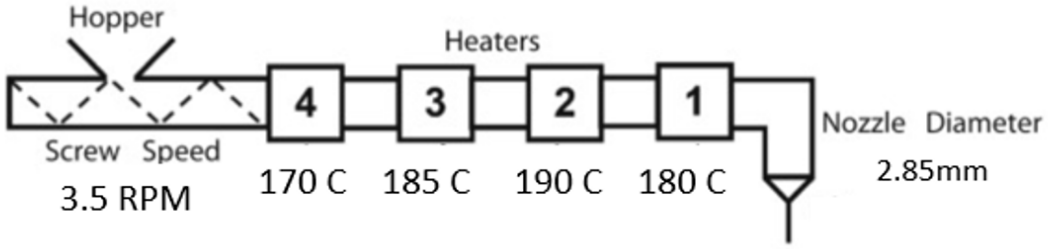

Figure 4.7 Extrusion profile for extruding TPU on a Precision 350 filament extruder.

the extruder. This liquid is considered PCM that is loss from the material due to broken capsules. This loss of PCM can be seen in the loss of melt enthalpy when compared to the material before filament extrusion in Table 4.2. Samples taken from the filament for analysis were taken near the beginning and end of the filament length.

The 50 and 60 wt% of MEPCM that was compound using a twin screw extruder and extruded into filament was used to 3D print samples to quantify any potential PCM loss from the temperatures experienced in the printing process. The 2.85mm diameter filament was printed using an Ultimaker S3 with printing parameters common for standard printing TPU. The print settings can be seen in Table 4.3. Three samples from both weight percentages were printed and three sam-

Table 4.2 Summarized Thermal Transition Properties of MEPCM-TPU Pellets extruded on the 3devo.

Sample Name	Extrusion Method (# extrusions)	Onset T_m (°C)	ΔH_m (J/g)	Onset T_c (°C)	ΔH_m (J/g)
24D PCM Powder	n/a	19.2	171.3	22.3	169.0
60wt% MEPCM	Single Screw (3x)	19.0 ± 0.2	78.2 ± 9.5	22.4 ± 1.4	72.1 ± 9.0
60wt% MEPCM	3Devo Single Screw (1x)	19.4 ± 0.1	55.7 ± 1.3	22.7 ± 0.1	46.0 ± 1.1
80 wt% MEPCM	Single Screw (4x)	19.1 ± 0.3	71.3 ± 8.9	22.2 ± 1.5	60.8 ± 8.2
80 wt% MEPCM	3Devo Single Screw (1x)	19.4 ± 0.1	51.8 ± 2.1	23.0 ± 0.1	38.7 ± 1.1
50 wt% MEPCM	Twin Screw (1x)	19.6 ± 0.2	60.7 ± 15.8	22.8 ± 0.1	59.0 ± 15.5
50 wt% MEPCM	3Devo Single Screw (1x)	19.5 ±0.1	36.9 ± 2.5	20.1 ± 0.2	28.1 ± 1.1
60 wt% MEPCM	Twin Screw (2x)	19.4 ± 0.3	42.5 ± 3.0	22.6 ± 0.2	36.3 ± 2.2
60 wt% MEPCM	3Devo Single Screw (1x)	19.5 ± 0.1	32.8 ± 1.9	22.9 ± 0.1	22.0 ± 1.0

ples were taken from each print to quantify the melt enthalpies after printing. The printed samples were found to print similarly to standard TPU and the quality of each sample and melt enthalpy for each weight percentage can be seen in Figure 4.8 and Table 4.4, respectively.

Table 4.3 Print settings for MEPCM-TPU filament

Nozzle Temperature [°C]	225
Bed Temperature [°C]	60
Print Speed [mm/sec]	25
Nozzle Diameter [mm]	0.4
Layer Height [mm]	0.2
# Layers	5

Table 4.4 Summarized Thermal Transition Properties of MEPCM-TPU printed samples.

Sample name	Onset T_m (C)	ΔH_m (J/g)	Onset T_c (C)	ΔH_c (J/g)
50 wt% MEPCM	19.4 ± 0.1	38.2 ± 0.2	20.8 ± 0.1	24.7 ± 0.2
60 wt% MEPCM	19.3 ± 0.1	35.1 ± 1.0	21.1 ± 0.2	20.5 ± 0.2

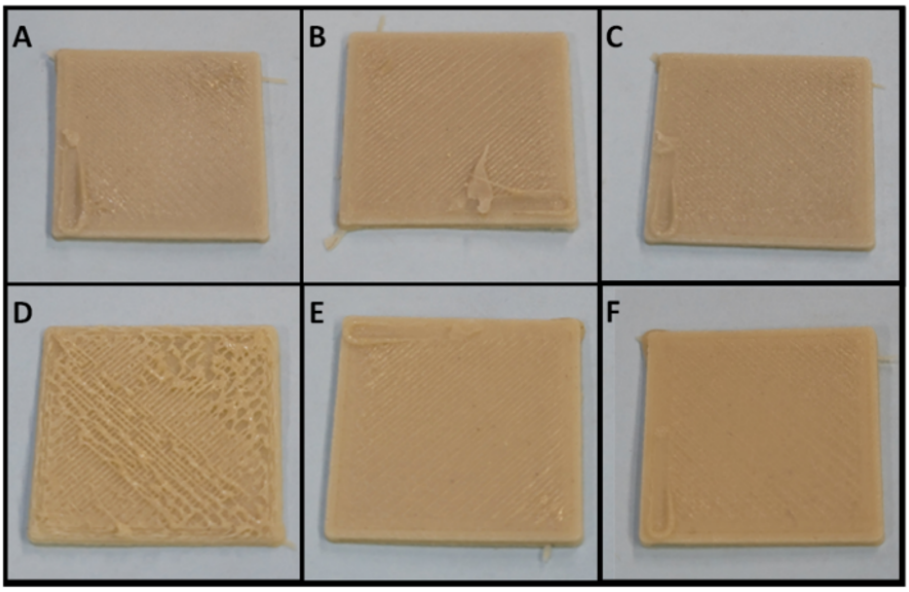

Figure 4.8 Printed samples of MEPCM-TPU. (A-C) 50wt% MEPCM and (D-F) 60wt%MEPCM

4.2 Characterization of MEPCM-TPU Powder and Filaments

4.2.1 Raw Materials

In this section, the composition and characterization of MEPCM with TPU powder is explored. The raw materials comprising the compound is 43D MEPCM from Microtek and TPU powder from STS inks. The MEPCM powder consist of particle sizes between 5 μ and 30 μ, while the TPU powder consist of particle sizes between 100 μ and 200 μ. SEM images of the individual particles can be seen in Figure 4.9

4.2.2 Single Screw Extusion of MEPCM-TPU Powder

MEPCM were compounded with a single screw exturder (3Devo 350 Precision) in weight percentages of 40wt%, 50wt%, 60wt%, and 70wt% of MEPCM in TPU powder. The extursion profile used can be seen in Figure 4.10. Images of filament surfaces can be seen in Figure 4.11. It can be seen in Figure 4.11(A-C) that surface of the filament is smooth at the surface, while in Figure 4.11(D) shows 70wt% of MEPCM leads to a rough surface quality.

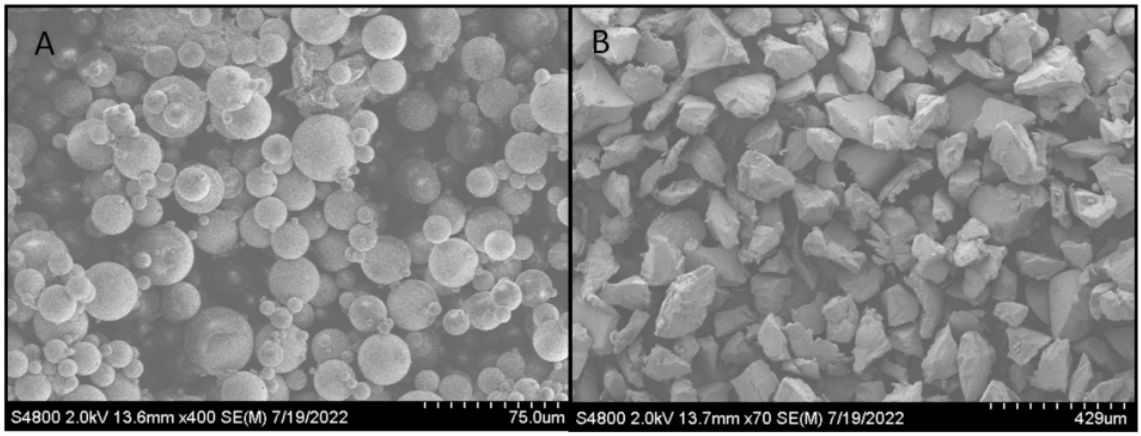

Figure 4.9 Micrographs of (A) MEPCM and (B) TPU powder

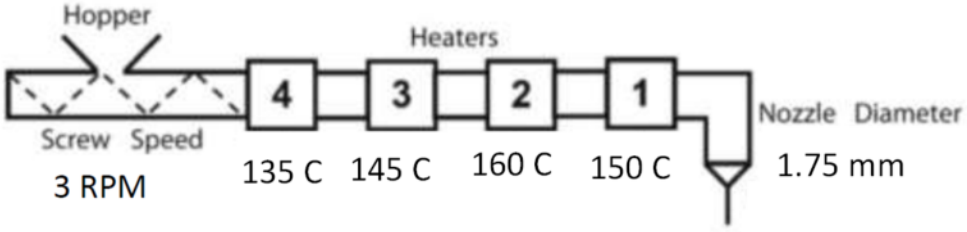

Figure 4.10 Extrusion profile for extruding MEPCM and TPU powder.

In Figure 4.12, the cross section of the 60wt% MEPCM filament can be seen. In the SEM image, the microcapsules can be seen packed together in the filament. Majoriety of the shells can be seen deformed from the contact with the other shells, but are mostly still intact. Compared to the micrographs of the extrusion with TPU pellets, it can be seen that the major contributor to the breaking of microcapsules can be attributed to the particle size of the polymer. If the particle size of the polymer is within the order of magnitude of the MEPCM particles, the MEPCM shell is less likely to rupture due to collison forces.

DSC data for the MEPCM powder, powder mixtures of MEPCM and TPU, the filament ratios, and printed samples can be seen in Table 4.5. Samples were taken 5 times for each material to get an average and standard deviation. It can be seen that the MEPCM powder has a base latent heat of fusion of 217 J/g $\pm$ 2.89

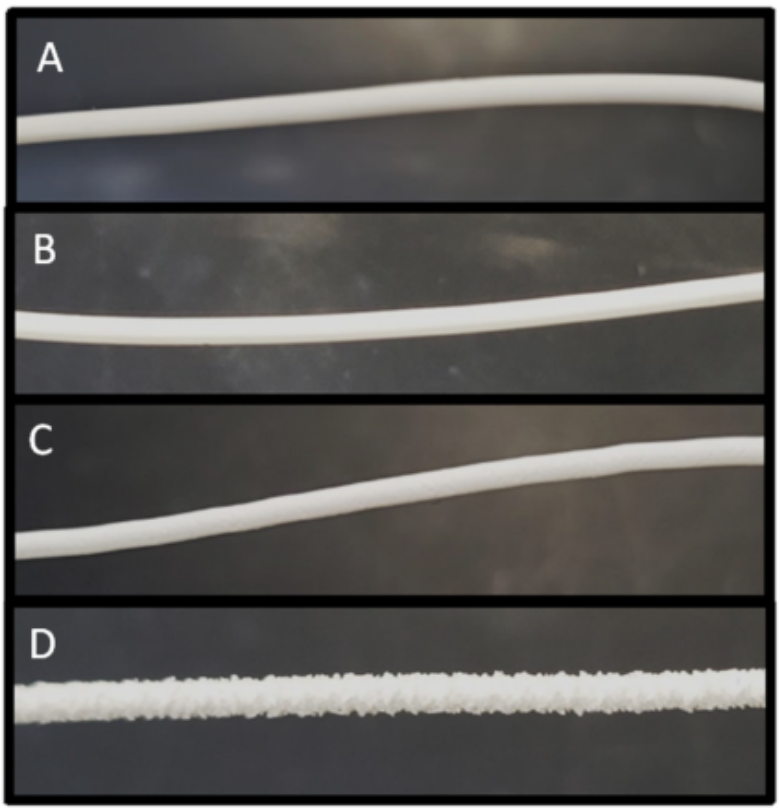

Figure 4.11 Surface images of (A) 40wt% MEPCM, (B) 50wt% MEPCM, (C) 60wt% MEPCM, and (D) 70wt% MEPCM

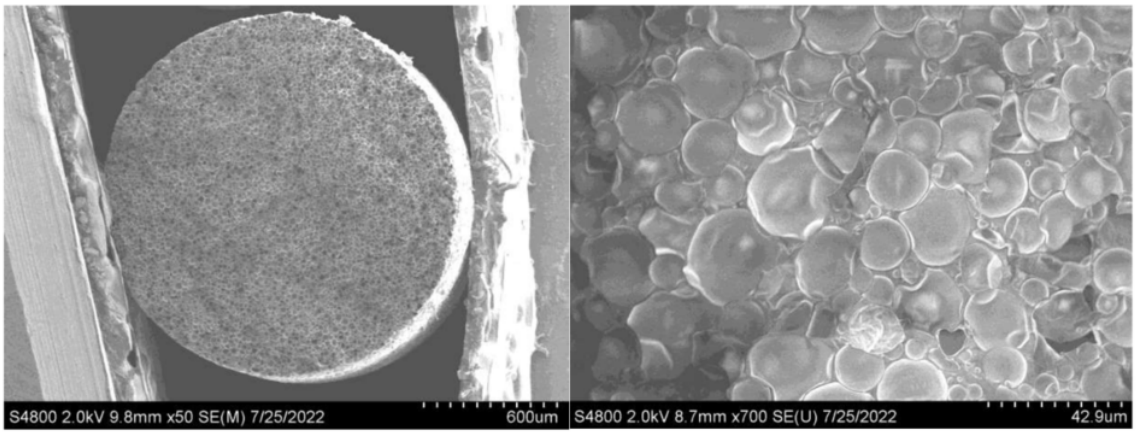

Figure 4.12 Micrographs of 60wt% MEPCM Filament

J/g. The ratios of powder mixtures and compounded filaments are compared to the base latent heat of fusion of the MEPCM powder. It can be seen that the powder mixtures have latent heat values very close to the measured weight percent-

Table 4.5 DSC characterization of MEPCM ratios of powder mixtures, filaments, and prints

Sample name	T_{onset} (°C)	Delta H_m (J/g)	Theo. wt% based on Delta H_m
43D MEPCM Powder	39.83 ± 0.77	217.10 ± 2.89	n/a
Powder Mixtures			
40 wt% 43D MEPCM	40.39 ± 0.46	85.88 ± 2.86	39.6%
50 wt% 43D MEPCM	39.82 ± 0.29	108.14 ± 2.30	49.8%
60 wt% 43D MEPCM	39.48 ± 0.23	132.71 ± 5.00	61.1%
70 wt% 43D MEPCM	39.52 ± 0.10	151.92 ± 4.89	69.9%
Filament			
40 wt% 43D MEPCM	39.24 ± 0.11	84.91 ± 2.55	39.1%
50 wt% 43D MEPCM	38.90 ± 0.10	107.83 ± 1.69	49.6%
60 wt% 43D MEPCM	38.84 ± 1.1	131.97 ± 0.13	60.8%
70 wt% 43D MEPCM	39.82 ± 0.62	149.65 ± 2.89	68.9%
Printed			
40 wt% 43D MEPCM	39.85 ± 0.72	82.79 ± 1.41	38.1%
50 wt% 43D MEPCM	39.60 ± 0.12	105.09 ± 3.34	48.4%
60 wt% 43D MEPCM	39.21 ± 0.18	127.02 ± 1.51	58.8%
70 wt% 43D MEPCM	n/a	n/a	n/a

ages. This can be expected, since the powder mixtures are not heated and do not have significant mechanical loading that could lead to broken microcapsules. The compounded filaments can be seen to have a minor decrease in latent heat values with losses of PCM at 1% or less. This is expected since the heating and shear effects of the single screw extruder can lead to the breaking of some microcapsules. Once the filament is printed, the latent heat values can be seen to slightly decrease again across all the ratios. This is also expected, since the printing process is another heated process with shear stress that can further break microcapsules.

5 Numerical Modeling for PCM Melting

In this chapter, the modeling and analysis of a shape-stabilized PCM is explored to observe the transient local heat transfer effects between a forced convection heat transfer fluid and the wall of a melting PCM. The transient local Nusselt is calculated using the transient wall temperature, wall heat flux, and bulk fluid temperature as the PCM is melting on the opposite side of the wall. These observations of transient local heat transfer can lead to a better understanding of how phase change processes can be better modeled, rather than relying on past heat transfer correlations that don't account for the phase change process effects at the wall.

5.1 Methodology

A PCM melting setup is modeled using two different schemes and boundary conditions along with a validation experiment. The setup involves the melting of two slabs of PCM sandwiching a microchannel fluid array. One model is a simplified model that incorporates a finite difference method (FDM), while the other model uses a commercial finite volume method (FVM). Both models were run using a constant power condition and a constant inlet temperature condition. The constant power condition involves the maintaining of a constant temperature difference across the test section, while the constant inlet temperature condition involves a traditional inlet temperature that is held constant. The validation experiment was run only in the constant power condition to validate the two models.

5.2 Finite-Volume Numerical Simulations

The numerical solutions were conducted using ANSYS FLUENT v2021 R2. The pressure–velocity coupling was solved with the SIMPLE scheme, PRESTO! for pressure, and second-order upwind for both momentum and energy. Least squares cell based for gradient was used for spatial discretization. The transient formulation utilized first-order upwind. The residuals for the convergence criteria were set to 1

$\times 10^{-6}$ for continuity, 1×10^{-6} for velocity, and 1×10^{-12} for energy. The under-relaxation factors were set to 0.3 for pressure, 1 for density, 1 for body forces, 0.7 for momentum, 0.9 for local liquid fraction, and 1 for energy.

5.2.1 Physical Model

An experimental setup was performed to validated the finite difference model and that data is used to validate the finite volume model[198]. In the experiment, rectangular slabs of tetradecane impregnated into a graphite matrix were placed on either side of a microchannel fluid array. The slabs were 45.7 cm in length, 25.4 cm in width, and 3.12 cm thick. The microchannel array was 45.7 cm in length, 25.4 cm in width, and a thickness of 0.30 cm. The wall thickness of the microchannel array was also 0.035 cm. These PCM slabs and microchannel array were insulated on all sides exposed to ambient air. A schematic of the experiment can be seen in Figure 5.1(a). Assumptions were made to simplify the physical model.

1. Three-dimensional effects are neglected.
2. The effects of natural convection in the PCM is negligible.
3. The PCM volume change is neglected.
4. The liquid and solid phases of the PCM have identical densities.
5. Contact resistance between the PCM and the fluid wall is not neglected.
6. The fluid flow is hydrodynamically developed, laminar and incompressible.
7. Microchannel fluid array is treated as a single square duct with the same wall thickness.

The boundaries between the different domains is handled as a conjugate boundary condition with a coupled relationship at the walls. The conjugate wall also has

added resistance of $1.6e^{-3}$ Km^2/W at the boundaries between the PCM and aluminum wall domains to better replicate the contact resistances that was experienced during the experiment. The location and dimensions of the domains can be seen in Figure 5.1(b), where the representative width is 0.254 meters.

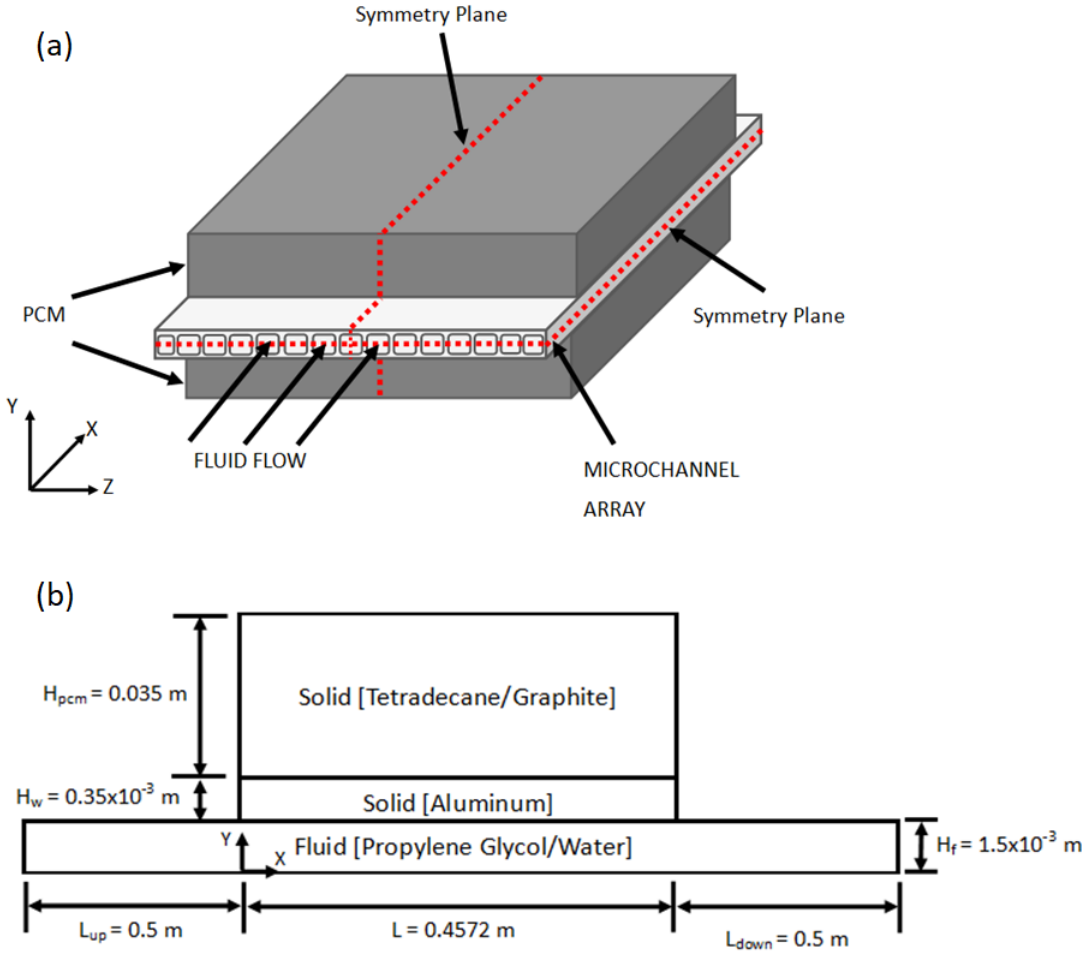

Figure 5.1 (a) 3D schematic of PCM test section with microchannel fluid array, (b) 2D domains and dimensions for FVM

The inlet velocity is 0.0264 m/s and the inlet temperature is 285.15 K (12 °C). No-slip and/or adiabatic conditions are applied to all boundaries except for the boundaries between the fluid/solid domains and between the two solid domains. The initial temperature of all domains were set to 273.15 K (0 °C). The initial pressure and velocities were set to 0 Pa and 0 m/s, respectively.

Material Properties

The PCM domain was modeled after a tetradecane graphite composite[198]. The tetradecane is impregnated into an expanded graphite matrix and has anisotropic thermal conductivity. The material properties for the PCM can be seen in Table 5.1.

Table 5.1 PCM Material Properties

Property	Value
k_{xx} [W/mK]	18
k_{yy} [W/mK]	10
ρ_s [kg/m^3]	836
h_{sl} [J/kg]	167978
c_{p_l} [J/kgK]	1888
c_{p_s} [J/kgK]	1424
T_m [K]	277.75
T_{on} [K]	277.5
T_{end} [K]	278
T_{ref} [K]	278.25
h_{ref} [J/kg]	387731.18

The specific heat of the PCM was applied to the Fluent model through the linear discretization of the specific heat versus temperature curve, represented in Figure 5.2.

The solid domain representing the wall between the fluid and PCM domain was modeled using standard aluminum properties. The material properties for the aluminum can be seen in Table 5.2.

Table 5.2 Aluminum Material Properties

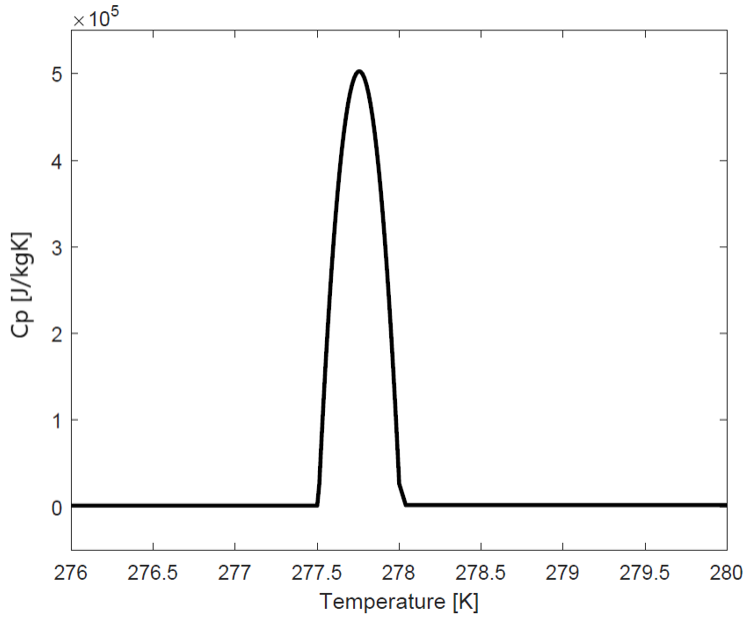

Figure 5.2 Tetradecane graphite matrix specific heat as a function of temperature

Property	Value
$c_{p,w}$ [J/kgK]	890
ρ_w [kg/m^3]	2710
k_w [W/mK]	200

The fluid domain was modeled based upon the material properties of a 20 percent concentration of propylene glycol in water. The fluid properties used in the fluid governing equations were modeled as a function of temperature using a discretized piece-wise linear function (similar to the specific heat of the PCM domian) and can be seen in Figure 5.3.

5.2.2 Governing Equations

In the present study, the governing equations used to model the fluid domain for 2D, laminar, incompressible flow of a Newtonian fluid with no additional source terms. The continuity equation is,

$$\nabla \cdot \overrightarrow{v_f} = 0 \tag{5.1}$$

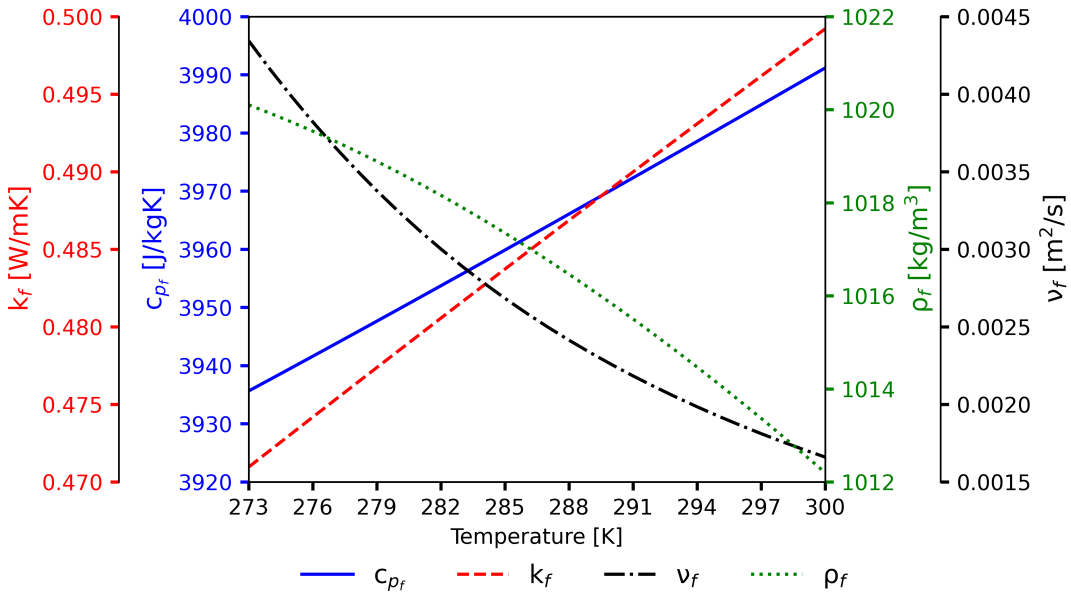

Figure 5.3 Material Properties of 20% concentration of propylene glycol in water as a function of temperature.

where, $\overrightarrow{v_f}$ is the 2-D velocity vector for the fluid domain.

The momentum equations for transient flow with no gravitational or external forces can be seen as,

$$\rho\left(\frac{\partial\overrightarrow{v_f}}{\partial t}+(\overrightarrow{v_f}\cdot\nabla)\overrightarrow{v_f}\right)=-\nabla p+\mu_f\nabla^2\overrightarrow{v_f} \tag{5.2}$$

where, $\overrightarrow{v_f}$ is the 2-D velocity vector, p is the static pressure, ρ is the density, and μ_f is the viscosity of the fluid.

The energy equation is solved separately for both the fluid and solid domains. The energy equation for the fluid domain is,

$$\rho_f c_{p_f}\frac{DT_f}{Dt}=k_f\nabla^2T_f \tag{5.3}$$

where, ρ_f, c_{p_f}, and k_f are the density, specific heat, and thermal conductivity of the fluid domain, respectively. T_f is the temperature in the fluid domain.

The energy equation for the solid domains is,

$$\rho_s \frac{\partial h}{\partial t} = \nabla \cdot (k_{eff} \nabla T_s) \tag{5.4}$$

where, ρ_s is the density of the solid, $\frac{\partial h}{\partial t}$ is the transient change in enthalpy of the solid, and $\nabla \cdot (k_{eff} \nabla T)$ represent the conduction in the solid domain. In the conduction term, k_{eff} is the anisotropic thermal conductivity that is defined as,

$$k_{eff} = k_{ij} = \begin{bmatrix} k_{xx} & k_{xy} \\ k_{yx} & k_{yy} \end{bmatrix} \tag{5.5}$$

where, k_{xx} and k_{yy} are the parallel (k_{para}) and perpendicular (k_{perp}) thermal conductivity, respectively. In Fluent, the enthalpy is defined as,

$$h = \int_{T_{ref}}^{T} c_{p_s} \, dT + h_{ref} \tag{5.6}$$

where, h_{ref} is the reference enthalpy at a reference temperature T_{ref}, and $c_{p,s}$ is the specific heat of the solid. The specific heat of the PCM is defined in Fluent using a piecewise-linear function with respect to temperature.

$$c_{p,s}(T) = c_{p_n} + \frac{c_{p_{n+1}} - c_{p_n}}{T_{n+1} - T_n}(T - T_n) \tag{5.7}$$

The specific heat for the aluminum solid domain uses a constant specific heat and isotropic thermal conductivity, while the PCM solid domain uses the piece-wise linear specific heat and anisotropic thermal conductivity.

5.2.3 Mesh and Time-Step Size

The mesh was created using Pointwise v18.0 with 2D structured cells for all the domains. The mesh had a total cell count of 1,971,919 cells with xy node dimensions of 4572x350 (1,595,279 cell count) for the PCM domain, 4562x30 (132,559 cell count) for the fluid domain, 4572x10 (41,139 cell count) for the aluminum wall domain, and 3500x30 (101,471 cell count) for both the upstream and downstream

fluid domains. Additional mesh sizes with a total cell count of 5,000,000 and 10,000,000 were evaluated and the outlet temperature with respect to time for all three cases were less than 1% difference. The total cell count of 1,971,919 cell was used for the final solution. The timestep was set to 0.1 seconds and a max iterations per timestep of 25. Additional timestep sizes were evaluated at 0.05 and 0.01 seconds. The outlet temperature with respect to time for all three timesteps were less than 1% difference and the final timestep size of 0.1 seconds was used for the final solution.

5.3 Finite Difference Model

The finite difference model used is a simplified melting and solidification model that solves the transient temperature and enthalpy response of a 2D PCM domain along with a 1D fluid domain[198]. The 2D PCM domain is discretized with a nodal map of 40 equidistant nodes in the x direction and 10 equidistant nodes in the y direction. The 1D fluid domain is discretized with nodes consisting of 40 equidistant nodes in the x direction. The amount of nodes for both the PCM domain and the fluid domain can be increased or decreased depending on the resolution required to be mesh independent and the amount of nodes in the PCM domain and the fluid domain were proven to be adequate based on validation to the experimental setup.

The change in enthalpy of the PCM domain nodes is calculated using Equation 1. This equation calculates the change in enthalpy for each timestep $(\frac{dh_{i,j}}{dt})$ using a central difference scheme at each node based upon the temperature of the surrounding nodes.

$$\frac{dh_{i,j}}{dt} = \frac{W}{m_{pcm}} \left[\frac{k_{para}\Delta y}{\Delta x}(T_{i,j-1} + T_{i,j+1} - 2T_{i,j}) + \frac{k_{perp}\Delta x}{\Delta y}(T_{i-1,j} + T_{i+1,j} - 2T_{i,j}) \right] \tag{5.8}$$

The total power $(\dot{Q}_{i,1})$ into or out of each of the PCM nodes at the wall ad-

jacent to the the fluid is calculated using Equation 2. This equation uses the temperature of the fluid node and the PCM node that share the same x position, along with a calculated thermal resistance (R_{f-PCM}) that can be seen in Equation 3.

$$\dot{Q}_{i,1} = \frac{T_{f,i} - T_{w,i}}{R_{f-PCM}} \tag{5.9}$$

$$R_{f-PCM} = \frac{\Delta y}{2k_{perp}W\Delta x} + \frac{R_{contact}}{W\Delta x} + \frac{t_{wall}}{k_w W\Delta x} + \frac{1}{htc_f W\Delta x} \tag{5.10}$$

The first term in the resistance equation (Equation 3) is the conduction through the PCM. The second term is the contact resistance between the PCM and the wall. The third term is the conduction resistance through the wall material that is existent in the experiment to separate the PCM and fluid. The fourth term is the convective resistance from the fluid to the wall. Any other resistances that are not shown in the equation are considered negligible.

The temperature at each fluid node for each timestep is calculated using Equation 4. This equation calculates the temperature change at each fluid node based upon the temperature of the fluid before and after the node, along with power ($\dot{Q}_i$) into or out of the PCM.

$$\frac{dT_{f,i}}{dt} = \frac{1}{\bar{c}_{p_f}\dot{m}_f}\left[\dot{m}_f\bar{c}_{p_f}(T_{f,in} - T_{f,i}) - 2\dot{Q}_i + \bar{k}_f(H_f W)\frac{T_{f,i+1} - T_{f,i}}{\Delta x}\right] \tag{5.11}$$

5.3.1 Heat Transfer Coefficient

The local heat transfer coefficient that is used in the resistance equation (Equation 3) is determined through the use of Nusselt number correlations.

$$htc_f = \bar{Nu}\frac{k_f}{D_h} \tag{5.12}$$

where htc_f is the local heat transfer coefficient, k_f is the thermal conductivity of the fluid, D_h is the hydraulic diameter of the fluid channel, and $\bar{Nus}$ is the average Nusselt number.

The average Nusselt number is determined by taking the average between the Nusselt number for a constant wall temperature (Nus_T) and constant wall heat flux (Nus_H) condition, as seen in Equation 6.

$$\bar{Nu} = \frac{Nu_T + Nu_H}{2} \tag{5.13}$$

The Nusselt number for a constant wall temperature and constant wall heat flux in a square duct for all four walls is defined using the approximation equation in the Handbook of single-phase convective heat transfer[373] can be seen in Equation 14 and 15,

$$Nu_T = 7.541\left[1 - 2.610\left(\frac{H_f}{W}\right) + 4.970\left(\frac{H_f}{W}\right)^2 - 5.119\left(\frac{H_f}{W}\right)^3 + 2.702\left(\frac{H_f}{W}\right)^4 - 0.548\left(\frac{H_f}{W}\right)^5\right] \tag{5.14}$$

$$Nu_H = 8.235\left[1 - 2.042\left(\frac{H_f}{W}\right) + 3.085\left(\frac{H_f}{W}\right)^2 - 2.477\left(\frac{H_f}{W}\right)^3 + 1.058\left(\frac{H_f}{W}\right)^4 - 0.186\left(\frac{H_f}{W}\right)^5\right] \tag{5.15}$$

where H_f is the height of the fluid channel and W is the width of the fluid channel.

5.4 Results

5.4.1 Validation with imposed constant power

The comparison of outlet temperatures between the experimental setup, the finite difference model and the finite volume model can be seen in Figure 5.4. These outlet temperatures are from the constant power cases to better compare with the experiment that was under constant power. The finite volume model is 6.45% difference of the finite difference model and 11.97% difference from the experimen-

tal data. This will serve as the validation for the finite volume model in both the constant temperature difference case and the constant inlet temperature case. Differences between the experiment and both numerical models outlet temperatures can be attributed to the assumptions made to the numerical models to simplify the computational intensity.

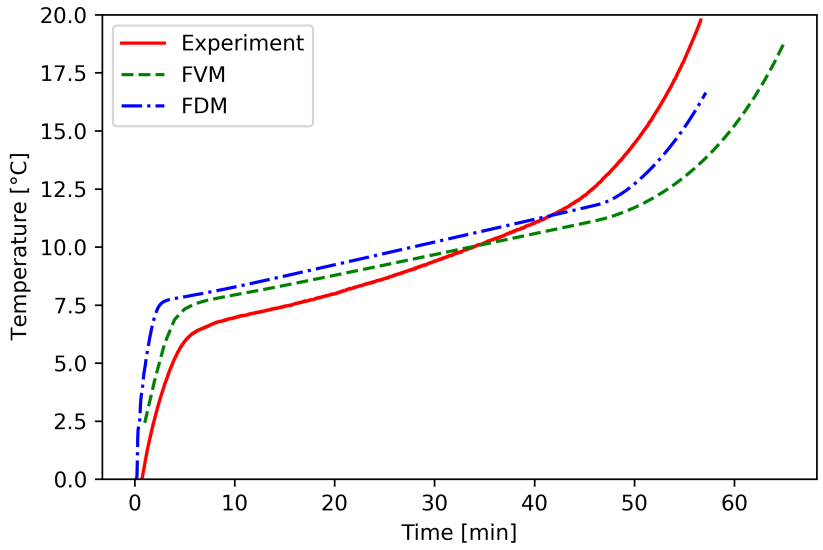

Figure 5.4 Outlet temperature for experiment, finite difference, and finite volume with the constant power setup

5.4.2 Constant Inlet Temperature Condition

It can be seen in Figures 5.5-5.7 contour plots early in the melt (Figure 5.5), middle of the melt (Figure 5.6), and near the end of the melt (Figure 5.7). In these figures a comparison can be seen between the finite difference model and the finite volume model, for both the contour plots of the melt front and local temperatures/wall heat flux for the fluid side. The wall temperatures, bulk temperatures, and wall heat fluxes show very similar compliance between both models early and in the middle of the melt. Near the end of the melt shows the temperatures and wall heat fluxes start to separate as the melt front start to differ between the two models. It can also be seen that early and near the middle of the melt, the fluent

model is melting faster closer to X/L=0, while the finite difference model is melting faster closer to X/L=1. This becomes more obvious near the end of the melt, when the amount of solid PCM is only near X/L=1. This causes the finite difference model to start melting faster than the finite volume model near the end of the melt.

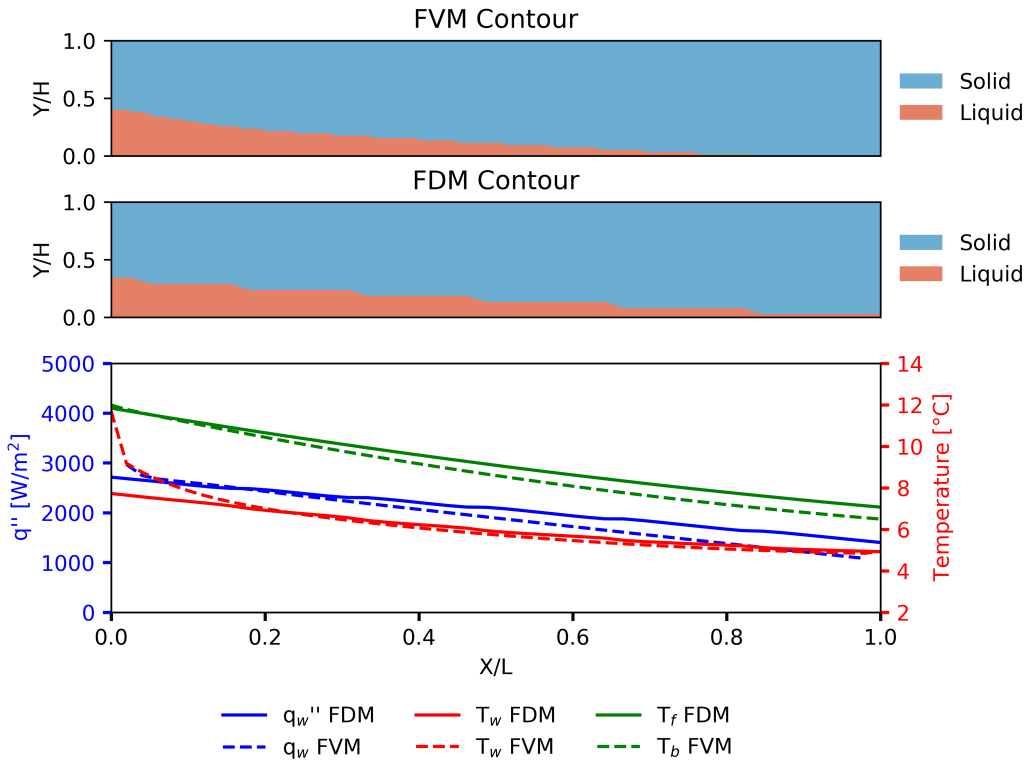

Figure 5.5 Comparison of Matlab and Fluent model with contour plots of melt front and local wall and fluid data at 10 minutes.

The local Nusselt numbers throughout various timesteps for the entire melt can be seen in Figure 5.8. In this figure you can see the local Nusselt number early in the melt that gradually increases in value towards the middle of the melt, when the melt front is moving away from the fluid wall. Once the melt front reaches the far wall around 33 mins, the start of the inactive zone begins. The inactive zone can be defined as the region of the PCM that is fully liquid for all y locations in a given region of x. This starts at X/L=0, when the melt front reaches Y/L=1 and

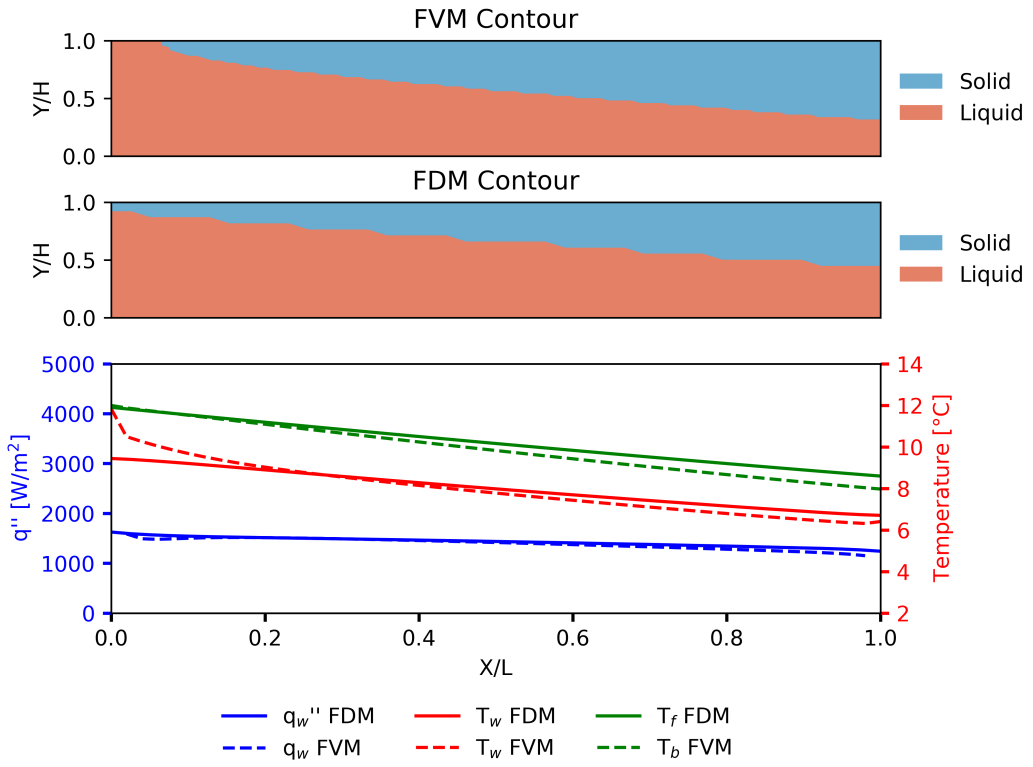

Figure 5.6 Comparison of Matlab and Fluent model with contour plots of melt front and local wall and fluid data at 35 minutes.

begins to grow downstream until the PCM is fully melted. A demonstrative figure can be seen in Figure 5.9. Within the inactive zone, the bulk fluid temperature, wall temperature and also the liquid PCM begin to reach isothermal temperatures equal to the inlet temperature. Also, at the inactive zone, the wall heat flux decreases to a near zero heat flux along with the wall and bulk temperatures becoming equal. As the inactive zone grows and the amount of solid PCM decreases, these effects can be more clearly seen in Figure 5.7.

After the inactive zone begins, a sudden increase in the local Nusselt number can be seen and a new maximum Nusselt number can be seen around a value of 10. In Figure 5.10, it can be seen that the sudden change from a high to low local Nusselt number occurs near the boundary of the inactive zone and the melt front. As the melt front moves and the inactive zone grows, this sudden change in local Nus-

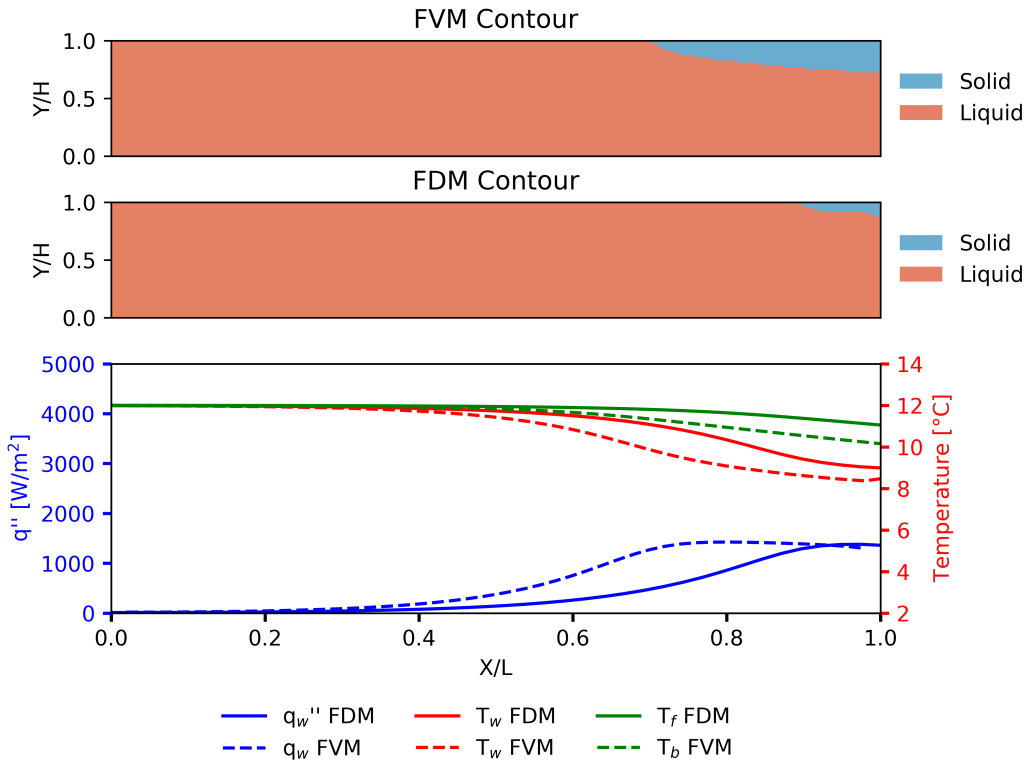

Figure 5.7 Comparison of Matlab and Fluent model with contour plots of melt front and local wall and fluid data at 60 minutes.

selt number will move accordingly with that boundary. Despite the sudden increase in local Nusselt number left of the melt front, the amount of heat transfer occurring at the wall is rapidly decreasing based upon the bulk temperature, wall temperature, and wall heat flux in that area. Therefore, the higher local Nusselt number left of the melt front is more likely a mathematical error with the difference in the bulk and wall temperatures and the wall heat flux approaching zero in that area.

It can be seen in Figure 5.11, the local Nusselt numbers for the various timesteps in comparison to the corresponding Nusselt number correlations given in Equations 14 and 15. In Figure 5.11(a), the timesteps associated with the melting of PCM before the formation on an inactive zone. These timesteps show an increase of the local Nusselt number as time progresses, which is associated with the movement of the melt front away from the wall the heat transfer fluid. The local Nusselt num-

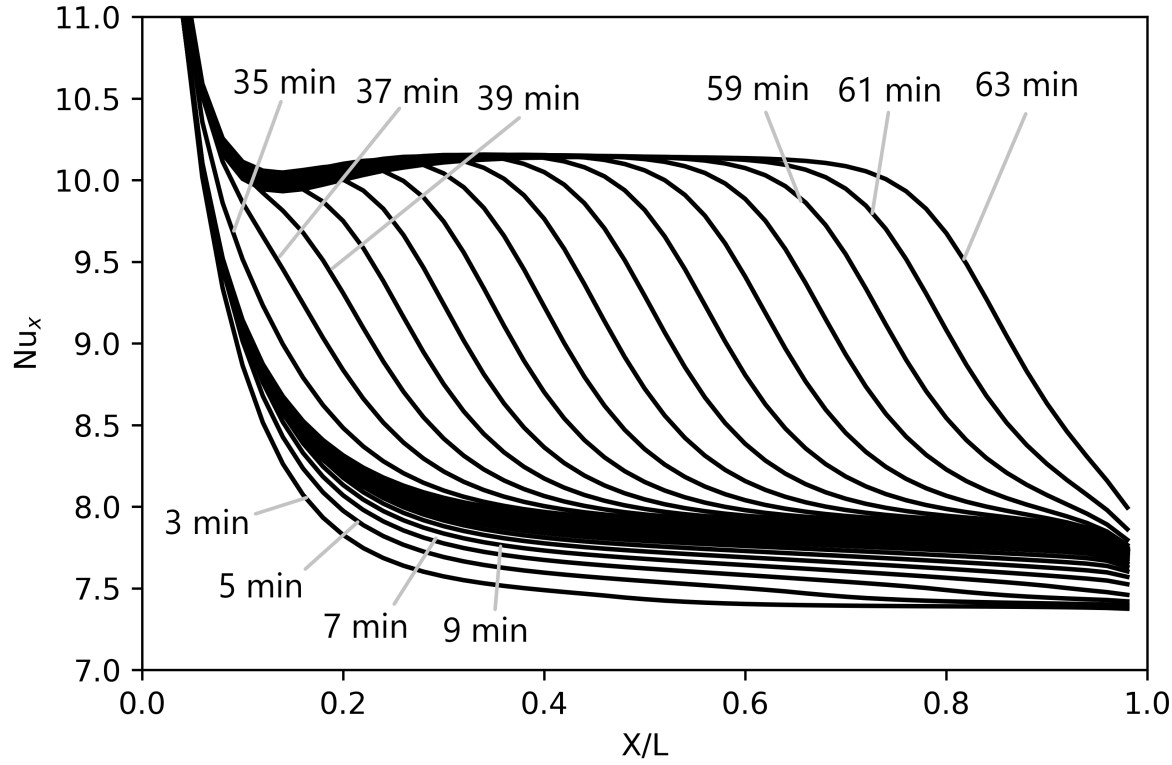

Figure 5.8 All local nusselt numbers for constant inlet temperature case in fluent model.

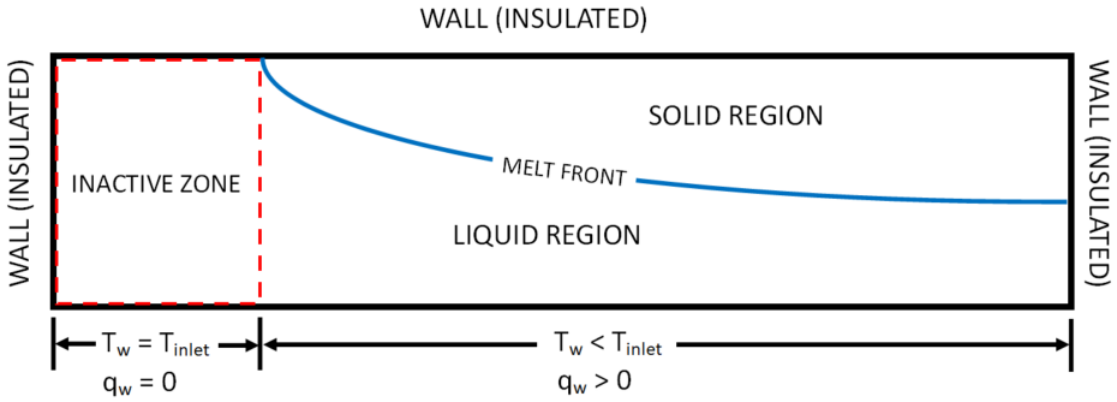

Figure 5.9 Illustration of inactive zone for melting of PCM.

bers within these timesteps show the same shape as a local Nusselt number with a developing and fully developed region, first starting near the constant wall temperature correlation and progressing up toward the constant wall heat flux correlation.

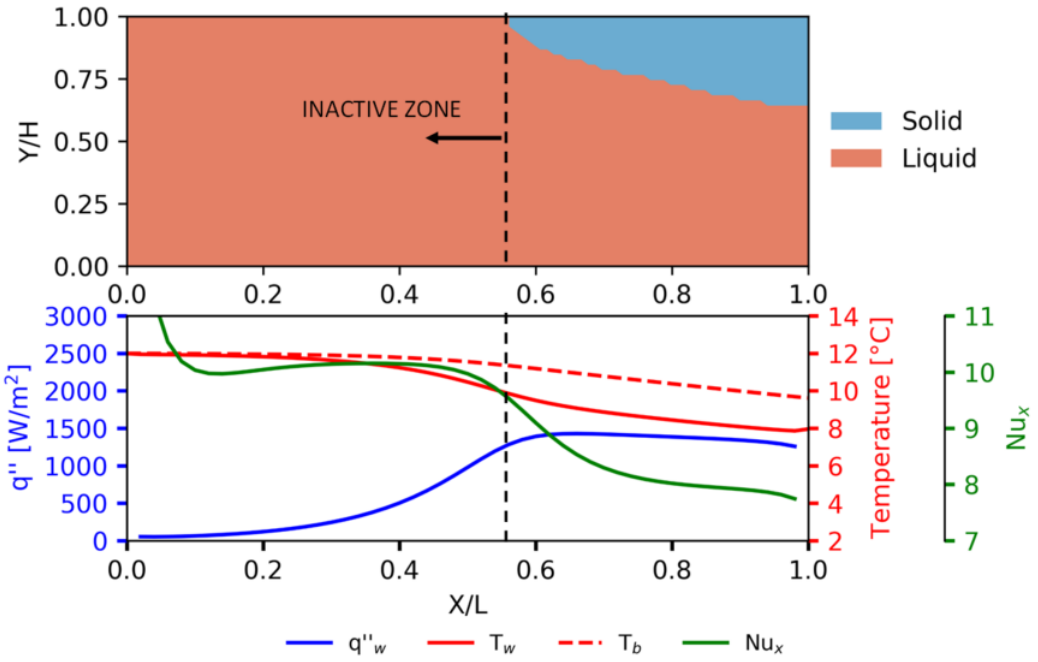

Figure 5.10 Local Nusselt number, wall temperature, bulk temperature, and wall heat flux from Fluent model with corresponding contour plot of PCM domain at time = 55 min.

As the timesteps increase, the local Nusselt number appears to be converging to one location. Once the inactive zone begins (after time = 33min), in Figure 5.11(b) the local Nusselt number can be seen to change shape drastically. This change can be directly attributed to the formation of an inactive zone and the final stages of the PCM melt front.

To the right of the inactive zone where solid PCM is still melting, the local Nusselt number is similar to the trend for a constant wall heat flux condition as if the start of a thermal boundary layer begins near the boundary of the inactive zone and the melt front. A demonstration of this effect can be seen illustrated in Figure 5.12. One explanation for this complex local Nusselt number is a potential superposition of two different thermal boundary layers. One thermal boundary layer that has a traditional starting position at the inlet of the fluid section and another thermal boundary layer that is progressively moving with the growth of inactive zone.

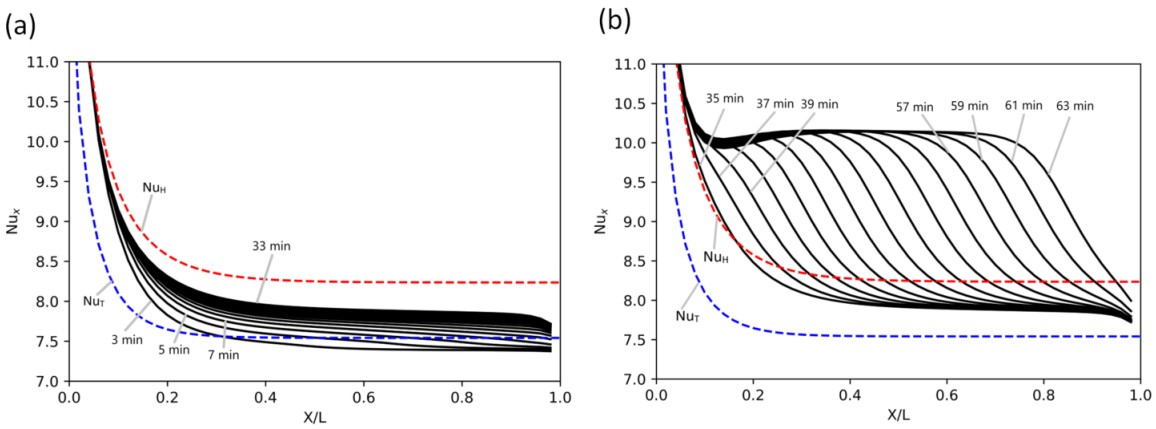

Figure 5.11 Local Nusselt number for various timesteps with contant wall temperature and constant wall heat flux correlations, (a) timesteps at 33min and below (pre-inactive zone), (b) timesteps at 35min and above (post-inactive zone)

The first thermal boundary layer at the entrance to the fluid region is more subtle as the temperature gradients in that region are progressively reaching a more isothermal state. The second thermal boundary layer that is moving, has more significant temperature gradients that would be seen in a stationary boundary layer. The movement and transient change in temperature gradients can be directly attributed to the influence of the melt front in that region that is actively moving as more PCM melts.

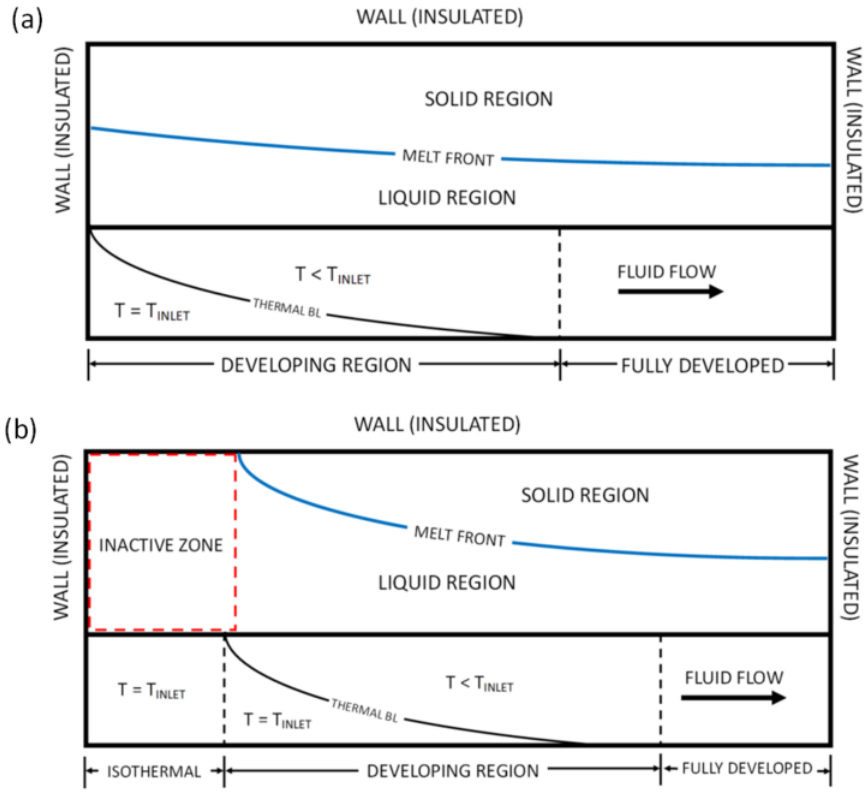

Figure 5.12 (a) Demonstrative figure for thermal boundary layer development with melt front spanning full length of fluid channel, (b) Demonstrative figure for thermal boundary layer development with simultaneous movement of melt front and inactive zone

6 Conclusions

6.1 HDPE/PCM Composite

A shape-stabilized PCM/HDPE functional composite has been printed using FFF for the first time. A composite comprising 40% PCM42 by mass was mixed with HDPE and extruded to make filament that is capable of thermal energy storage. It was determined through DSC testing that the thermal storage capability of the resultant filament effectively behaved as if there was 31.8% of the PCM42 in the composite. Furthermore, the filament was printed into sample specimens for further thermal testing. Utilizing SEM, the microstructures of the PCM42/HDPE composite material were investigated after the first extrusion(filament making) and after the second extrusion (printing), and it was found that the material retained the same form after multiple extrusions. A heated HDPE build plate and heated enclosure were used to improve the print process of HDPE and the composite. Although there are many known difficulties in printing pure HDPE, the added PCM helped make the process easier. Phase-change temperature, effective latent heat of fusion, and thermal conductivity were measured and reported.

The results are promising, especially since the ability to directly print PCM, "encapsulated" in a polymer, can potentially revolutionize the manufacturing of thermal energy storage and management systems. Further work needs to be done to evaluate thermal cycling for long-term stability and leakage issues. In general, it has been shown that HDPE and PCM have the potential for long-term compatibility, and leakage issues can hopefully be mitigated with epoxy coatings. In addition, mechanical property testing including, but not limited to, tensile and flexure testing of specimens extracted from 3D printed samples of different raster orientations will be conducted in future work.

To show that an organic-based PCM shape stabilized with HDPE has very little affinity for moisture (i.e., they are extremely non-hygroscopic materials). Dif-

ferent compositions of the samples have been prepared to determine if the composition can impact the steady-state and transient moisture adsorption and desorption behaviour. While some distinction between the various compositions and operating temperatures was observed, the moisture adsorption and desorption diffusivities indicate that the materials will not be impacted by the presence of moisture. This is a highly promising outcome since it helps justify the use of these materials in various thermal energy storage applications where the presence of moisture is anticipated.

6.2 MEPCM/TPU Composite

The results of the composition of a microencapsulated PCM with a powder TPU polymer shows outstanding retention of PCM by relying on the microencapsulation of the PCM for sealing and using the polymer as a binding matrix for 3D printing. Successful compounding of MEPCM into a polymer relies on the polymer particle size be smaller than the typical polymer pellet size of around 2mm. Large particle size of polymer leads to the destruction of microcapsules during the extrusion process, while using powder polymer leads to successful compounding of MEPCM and polymer. Up to 60wt.% of MEPCM was successfully compounded in TPU with excellent filament quality and less than 1% loss of PCM after filament extrusion. After 3D printing, the total loss of PCM was less than 2%. Characterization of filaments and prints were performed using DSC for thermal storage capacity and at 60wt.% of MEPCM, the thermal storage capacity was measured to be about 130 J/g. Further characterization in the future includes thermal conductivity and mechanical strength of compounded materials and prints.

6.3 Numerical Modeling

A transient finite volume model was used to explore the coupled heat transfer effects at the wall boundary between a shape-stabilized PCM and a laminar forced convection heat transfer fluid. It was found that the local Nusselt number is di-

rectly influenced by the location of the melt front within the PCM. Early in the melting of the PCM, the local Nusselt number is close to the local Nusselt number for the same fluid geometry with a constant wall temperature condition. As the melt front progresses away from the wall of the heat transfer fluid, the local Nusselt number transitions from a constant wall temperature condition towards the local Nusselt number for a constant wall heat flux condition. Later in the melt, the local Nusselt number greatly changes when an inactive zone starts to develop. This causes the local heat transfer within the inactive zone at the wall to transition to an isothermal condition and causes a movement of the thermal development length to follow the remaining solid PCM that is melting. This discovery can lead to a better understanding of the heat transfer effects that occur at the heat transfer surface during the melting of PCM.

REFERENCES

[1] Garimella, S., Lockyear, K., Pharis, D., El Chawa, O., Hughes, M. T., and Kini, G., "Realistic pathways to decarbonization of building energy systems," *Joule*, Vol. 6, No. 5, 2022, pp. 956–971. https://doi.org/10.1016/j.joule.2022.04.003, URL https://www.sciencedirect.com/science/article/pii/S2542435122001416.

[2] Henry, A., Prasher, R., and Majumdar, A., "Five thermal energy grand challenges for decarbonization," *Nature Energy*, Vol. 5, No. 9, 2020, pp. 635–637. https://doi.org/10.1038/s41560-020-0675-9, URL https://www.nature.com/articles/s41560-020-0675-9, number: 9 Publisher: Nature Publishing Group.

[3] Odukomaiya, A., Woods, J., James, N., Kaur, S., Gluesenkamp, K. R., Kumar, N., Mumme, S., Jackson, R., and Prasher, R., "Addressing energy storage needs at lower cost via on-site thermal energy storage in buildings," *Energy & Environmental Science*, Vol. 14, No. 10, 2021, pp. 5315–5329. https://doi.org/10.1039/D1EE01992A, URL https://pubs.rsc.org/en/content/articlelanding/2021/ee/d1ee01992a, publisher: The Royal Society of Chemistry.

[4] Akhmetov, B., Georgiev, A., Kaltayev, A., Dzhomartov, A., Popov, R., and Tungatarova, M., "Thermal energy storage systems - Review," *Bulgarian Chemical Communications*, Vol. 48, 2016, pp. 31–40. URL https://www.scopus.com/inward/record.uri?eid=2-s2.0-85063556109&partnerID=40&md5=52ca41805263dc0b3d6bb09605afc024.

[5] Al-Abidi, A., Bin Mat, S., Sopian, K., Sulaiman, M., Lim, C., and Th, A., "Review of thermal energy storage for air conditioning systems," *Renewable and Sustainable Energy Reviews*, Vol. 16, No. 8, 2012, pp. 5802–5819. https://doi.org/10.1016/j.rser.2012.05.030, URL https://www.scopus.com/

inward/record.uri?eid=2-s2.0-84864521197&doi=10.1016%2fj.rser.2012.05.030&partnerID=40&md5=dedefc015b1e302ec9466e44b4708451.

[6] Alkilani, M., Sopian, K., Alghoul, M., Sohif, M., and Ruslan, M., "Review of solar air collectors with thermal storage units," *Renewable and Sustainable Energy Reviews*, Vol. 15, No. 3, 2011, pp. 1476–1490. https://doi.org/10.1016/j.rser.2010.10.019, URL https://www.scopus.com/inward/record.uri?eid=2-s2.0-78651078966&doi=10.1016%2fj.rser.2010.10.019&partnerID=40&md5=dd8bfec2773e9513b0084f453bd8efaf.

[7] Ben Romdhane, S., Amamou, A., Ben Khalifa, R., Saïd, N., Younsi, Z., and Jemni, A., "A review on thermal energy storage using phase change materials in passive building applications," *Journal of Building Engineering*, Vol. 32, 2020. https://doi.org/10.1016/j.jobe.2020.101563, URL https://www.scopus.com/inward/record.uri?eid=2-s2.0-85091553858&doi=10.1016%2fj.jobe.2020.101563&partnerID=40&md5=c6ff89b408fac37603908afb5436f5cc.

[8] Koçak, B., Fernandez, A. I., and Paksoy, H., "Review on sensible thermal energy storage for industrial solar applications and sustainability aspects," *Solar Energy*, Vol. 209, 2020, pp. 135–169. https://doi.org/10.1016/j.solener.2020.08.081, URL https://www.sciencedirect.com/science/article/pii/S0038092X20309208.

[9] Pielichowska, K., and Pielichowski, K., "Phase change materials for thermal energy storage," *Progress in Materials Science*, Vol. 65, 2014, pp. 67–123. https://doi.org/10.1016/j.pmatsci.2014.03.005, URL https://www.sciencedirect.com/science/article/pii/S0079642514000358.

[10] Fallahi, A., Guldentops, G., Tao, M., Granados-Focil, S., and Van Dessel, S., "Review on solid-solid phase change materials for thermal energy

storage: Molecular structure and thermal properties," *Applied Thermal Engineering*, Vol. 127, 2017, pp. 1427–1441. https://doi.org/10.1016/j.applthermaleng.2017.08.161, URL https://www.sciencedirect.com/science/article/pii/S1359431117329939.

[11] Carrillo, A. J., González-Aguilar, J., Romero, M., and Coronado, J. M., "Solar Energy on Demand: A Review on High Temperature Thermochemical Heat Storage Systems and Materials," *Chemical Reviews*, Vol. 119, No. 7, 2019, pp. 4777–4816. https://doi.org/10.1021/acs.chemrev.8b00315, URL https://doi.org/10.1021/acs.chemrev.8b00315, publisher: American Chemical Society.

[12] Scapino, L., Zondag, H. A., Van Bael, J., Diriken, J., and Rindt, C. C. M., "Sorption heat storage for long-term low-temperature applications: A review on the advancements at material and prototype scale," *Applied Energy*, Vol. 190, 2017, pp. 920–948. https://doi.org/10.1016/j.apenergy.2016.12.148, URL https://www.sciencedirect.com/science/article/pii/S0306261916319316.

[13] Solé, A., Martorell, I., and Cabeza, L. F., "State of the art on gas–solid thermochemical energy storage systems and reactors for building applications," *Renewable and Sustainable Energy Reviews*, Vol. 47, 2015, pp. 386–398. https://doi.org/10.1016/j.rser.2015.03.077, URL https://www.sciencedirect.com/science/article/pii/S1364032115002300.

[14] Yang, T., King, W. P., and Miljkovic, N., "Phase change material-based thermal energy storage," *Cell Reports Physical Science*, Vol. 2, No. 8, 2021, p. 100540. https://doi.org/10.1016/j.xcrp.2021.100540, URL https://www.sciencedirect.com/science/article/pii/S2666386421002514.

[15] Hirano, S., "Thermal Energy Storage and Transport," *Handbook of Climate*

Change Mitigation, edited by W.-Y. Chen, J. Seiner, T. Suzuki, and M. Lackner, Springer US, New York, NY, 2012, pp. 669–700. https://doi.org/10.1007/978-1-4419-7991-9_20, URL https://doi.org/10.1007/978-1-4419-7991-9_20.

[16] Leffler, A. J., and Weinstein, D. I., "CONSIDERATIONS IN THE USE OF SOLID-SOLID PHASE TRANSITIONS FOR THERMAL ENERGY STORAGE," *Sun: Mankind's Future Source of Energy*, edited by F. de Winter and M. Cox, Pergamon, 1978, pp. 507–510. https://doi.org/10.1016/B978-1-4832-8407-1.50099-4, URL https://www.sciencedirect.com/science/article/pii/B9781483284071500994.

[17] Fukai, J., Hamada, Y., Morozumi, Y., and Miyatake, O., "Effect of carbon-fiber brushes on conductive heat transfer in phase change materials," *International Journal of Heat and Mass Transfer*, Vol. 45, No. 24, 2002, pp. 4781–4792. https://doi.org/10.1016/S0017-9310(02)00179-5, URL https://www.sciencedirect.com/science/article/pii/S0017931002001795.

[18] Mhike, W., Focke, W. W., Mofokeng, J. P., and Luyt, A. S., "Thermally conductive phase-change materials for energy storage based on low-density polyethylene, soft Fischer–Tropsch wax and graphite," *Thermochimica Acta*, Vol. 527, 2012, pp. 75–82. https://doi.org/10.1016/j.tca.2011.10.008, URL https://www.sciencedirect.com/science/article/pii/S0040603111005077.

[19] Yang, X., Yang, X., Ding, J., Shao, Y., Qin, F. G. F., and Jiang, R., "Criteria for performance improvement of a molten salt thermocline storage system," *Applied Thermal Engineering*, Vol. 48, 2012, pp. 24–31. https://doi.org/10.1016/j.applthermaleng.2012.04.046, URL https://www.sciencedirect.com/science/article/pii/S135943111200289X.

[20] Sarier, N., and Onder, E., "Organic phase change materials and their textile

applications: An overview," *Thermochimica Acta*, Vol. 540, 2012, pp. 7–60. https://doi.org/10.1016/j.tca.2012.04.013, URL https://www.sciencedirect.com/science/article/pii/S0040603112001773.

[21] Tomassetti, S., Aquilanti, A., Muciaccia, P. F., Coccia, G., Mankel, C., Koenders, E. A. B., and Di Nicola, G., "A review on thermophysical properties and thermal stability of sugar alcohols as phase change materials," *Journal of Energy Storage*, Vol. 55, 2022, p. 105456. https://doi.org/10.1016/j.est.2022.105456, URL https://www.sciencedirect.com/science/article/pii/S2352152X22014487.

[22] Rozanna, D., Chuah, T. G., Salmiah, A., Choong, T. S. Y., and Sa'ari, M., "Fatty Acids as Phase Change Materials (PCMs) for Thermal Energy Storage: A Review," *International Journal of Green Energy*, Vol. 1, No. 4, 2005, pp. 495–513. https://doi.org/10.1081/GE-200038722, URL https://doi.org/10.1081/GE-200038722, publisher: Taylor & Francis _eprint: https://doi.org/10.1081/GE-200038722.

[23] Li, Q., Li, C., Du, Z., Jiang, F., and Ding, Y., "A review of performance investigation and enhancement of shell and tube thermal energy storage device containing molten salt based phase change materials for medium and high temperature applications," *Applied Energy*, Vol. 255, 2019, p. 113806. https://doi.org/10.1016/j.apenergy.2019.113806, URL https://www.sciencedirect.com/science/article/pii/S030626191931493X.

[24] Xie, N., Huang, Z., Luo, Z., Gao, X., Fang, Y., and Zhang, Z., "Inorganic Salt Hydrate for Thermal Energy Storage," *Applied Sciences*, Vol. 7, No. 12, 2017, p. 1317. https://doi.org/10.3390/app7121317, URL http://www.mdpi.com/2076-3417/7/12/1317.

[25] Shamberger, P. J., and Bruno, N. M., "Review of metallic phase change materials for high heat flux transient thermal management applications," *Applied Energy*, Vol. 258, 2020, p. 113955. https://doi.org/10.1016/j.apenergy.2019.113955, URL https://www.sciencedirect.com/science/article/pii/S0306261919316423.

[26] Singh, P., Sharma, R. K., Ansu, A. K., Goyal, R., Sarı, A., and Tyagi, V. V., "A comprehensive review on development of eutectic organic phase change materials and their composites for low and medium range thermal energy storage applications," *Solar Energy Materials and Solar Cells*, Vol. 223, 2021, p. 110955. https://doi.org/10.1016/j.solmat.2020.110955, URL https://www.sciencedirect.com/science/article/pii/S0927024820305493.

[27] Wieckowski, M., and Królikowski, M., "Designing and Characterization of Low-Temperature Eutectic Phase Change Materials Based on Alkanes," *Journal of Chemical & Engineering Data*, Vol. 67, No. 3, 2022, pp. 727–738. https://doi.org/10.1021/acs.jced.1c00783, URL https://doi.org/10.1021/acs.jced.1c00783, publisher: American Chemical Society.

[28] Safari, A., Saidur, R., Sulaiman, F. A., Xu, Y., and Dong, J., "A review on supercooling of Phase Change Materials in thermal energy storage systems," *Renewable and Sustainable Energy Reviews*, Vol. 70, 2017, pp. 905–919. https://doi.org/10.1016/j.rser.2016.11.272, URL https://www.sciencedirect.com/science/article/pii/S136403211631053X.

[29] Mohamed, S. A., Al-Sulaiman, F. A., Ibrahim, N. I., Zahir, M. H., Al-Ahmed, A., Saidur, R., Yılbaş, B. S., and Sahin, A. Z., "A review on current status and challenges of inorganic phase change materials for thermal energy storage systems," *Renewable and Sustainable Energy Reviews*, Vol. 70, 2017,

pp. 1072–1089. https://doi.org/10.1016/j.rser.2016.12.012, URL https://www.sciencedirect.com/science/article/pii/S1364032116310632.

[30] He, B., Martin, V., and Setterwall, F., "Phase transition temperature ranges and storage density of paraffin wax phase change materials," *Energy*, Vol. 29, No. 11, 2004, pp. 1785–1804. https://doi.org/10.1016/j.energy.2004.03.002, URL https://www.sciencedirect.com/science/article/pii/S0360544204000775.

[31] He, B., and Setterwall, F., "Technical grade paraffin waxes as phase change materials for cool thermal storage and cool storage systems capital cost estimation," *Energy Conversion and Management*, Vol. 43, No. 13, 2002, pp. 1709–1723. https://doi.org/10.1016/S0196-8904(01)00005-X, URL https://www.sciencedirect.com/science/article/pii/S019689040100005X.

[32] HIMRAN, S., SUWONO, A., and MANSOORI, G. A., "Characterization of Alkanes and Paraffin Waxes for Application as Phase Change Energy Storage Medium," *Energy Sources*, Vol. 16, No. 1, 1994, pp. 117–128. https://doi.org/10.1080/00908319408909065, URL https://doi.org/10.1080/00908319408909065, publisher: Taylor & Francis _eprint: https://doi.org/10.1080/00908319408909065.

[33] Fang, G., Li, H., Yang, F., Liu, X., and Wu, S., "Preparation and characterization of nano-encapsulated n-tetradecane as phase change material for thermal energy storage," *Chemical Engineering Journal*, Vol. 153, No. 1, 2009, pp. 217–221. https://doi.org/10.1016/j.cej.2009.06.019, URL https://www.sciencedirect.com/science/article/pii/S1385894709004525.

[34] Kalaiselvam, S., Veerappan, M., Arul Aaron, A., and Iniyan, S., "Experimental and analytical investigation of solidification and melting characteristics of PCMs inside cylindrical encapsulation," *International Journal of Ther-*

mal Sciences, Vol. 47, No. 7, 2008, pp. 858–874. https://doi.org/10.1016/j.ijthermalsci.2007.07.003, URL https://www.sciencedirect.com/science/article/pii/S1290072907001688.

[35] Vélez, C., Khayet, M., and Ortiz de Zárate, J. M., "Temperature-dependent thermal properties of solid/liquid phase change even-numbered n-alkanes: n-Hexadecane, n-octadecane and n-eicosane," *Applied Energy*, Vol. 143, 2015, pp. 383–394. https://doi.org/10.1016/j.apenergy.2015.01.054, URL https://www.sciencedirect.com/science/article/pii/S0306261915000707.

[36] Sarı, A., Alkan, C., and Karaipekli, A., "Preparation, characterization and thermal properties of PMMA/n-heptadecane microcapsules as novel solid–liquid microPCM for thermal energy storage," *Applied Energy*, Vol. 87, No. 5, 2010, pp. 1529–1534. https://doi.org/10.1016/j.apenergy.2009.10.011, URL https://www.sciencedirect.com/science/article/pii/S0306261909004395.

[37] Li, H., Liu, X., and Fang, G., "Preparation and characteristics of n-nonadecane/cement composites as thermal energy storage materials in buildings," *Energy and Buildings*, Vol. 42, No. 10, 2010, pp. 1661–1665. https://doi.org/10.1016/j.enbuild.2010.04.009, URL https://www.sciencedirect.com/science/article/pii/S0378778810001386.

[38] Sarı, A., Alkan, C., and Biçer, A., "Thermal energy storage characteristics of micro-nanoencapsulated heneicosane and octacosane with poly(methylmethacrylate) shell," *Journal of Microencapsulation*, Vol. 33, No. 3, 2016, pp. 221–228. https://doi.org/10.3109/02652048.2016.1144820, URL https://doi.org/10.3109/02652048.2016.1144820, publisher: Taylor & Francis _eprint: https://doi.org/10.3109/02652048.2016.1144820.

[39] Alkan, C., "Enthalpy of melting and solidification of sulfonated paraffins as

phase change materials for thermal energy storage," *Thermochimica Acta*, Vol. 451, No. 1, 2006, pp. 126–130. https://doi.org/10.1016/j.tca.2006.09.010, URL https://www.sciencedirect.com/science/article/pii/S0040603106004928.

[40] Sarı, A., and Karaipekli, A., "Thermal conductivity and latent heat thermal energy storage characteristics of paraffin/expanded graphite composite as phase change material," *Applied Thermal Engineering*, Vol. 27, No. 8, 2007, pp. 1271–1277. https://doi.org/10.1016/j.applthermaleng.2006.11.004, URL https://www.sciencedirect.com/science/article/pii/S1359431106004030.

[41] Weng, Y.-C., Cho, H.-P., Chang, C.-C., and Chen, S.-L., "Heat pipe with PCM for electronic cooling," *Applied Energy*, Vol. 88, No. 5, 2011, pp. 1825–1833. https://doi.org/10.1016/j.apenergy.2010.12.004, URL https://www.sciencedirect.com/science/article/pii/S0306261910005118.

[42] Sarı, A., Alkan, C., Döğüşcü, D. K., and Kızıl, , "Micro/nano encapsulated n-tetracosane and n-octadecane eutectic mixture with polystyrene shell for low-temperature latent heat thermal energy storage applications," *Solar Energy*, Vol. 115, 2015, pp. 195–203. https://doi.org/10.1016/j.solener.2015.02.035, URL https://www.sciencedirect.com/science/article/pii/S0038092X1500105X.

[43] Naikwadi, A. T., Samui, A. B., and Mahanwar, P. A., "Melamine-formaldehyde microencapsulated n-Tetracosane phase change material for solar thermal energy storage in coating," *Solar Energy Materials and Solar Cells*, Vol. 215, 2020, p. 110676. https://doi.org/10.1016/j.solmat.2020.110676, URL https://www.sciencedirect.com/science/article/pii/S0927024820302774.

[44] Dhandayuthabani, M., Jegadheeswaran, S., Vijayan, V., and Antony, A. G., "Investigation of latent heat storage system using graphite micro-particle en-

hancement," *Journal of Thermal Analysis and Calorimetry*, Vol. 139, No. 3, 2020, pp. 2181–2186. https://doi.org/10.1007/s10973-019-08625-7, URL https://doi.org/10.1007/s10973-019-08625-7.

[45] Huang, J., Wang, T., Wang, C., and Rao, Z., "Molecular Dynamics Simulations of Melting Behaviour of n-Hexacosane as Phase Change Material for Thermal Energy Storage," *Asian Journal of Chemistry*, Vol. 25, No. 4, 2013, pp. 1839–1841. https://doi.org/10.14233/ajchem.2013.13180, URL http://www.asianjournalofchemistry.co.in/User/ViewFreeArticle.aspx?ArticleID=25_4_17.

[46] Paneliya, S., Khanna, S., Utsav, Makani, N. H., Banerjee, R., and Mukhopadhyay, I., "Highly stable n-hexacosane loaded exfoliated graphite nanosheets for enhanced thermal energy storage application," *Journal of Energy Storage*, Vol. 48, 2022, p. 103903. https://doi.org/10.1016/j.est.2021.103903, URL https://www.sciencedirect.com/science/article/pii/S2352152X21015681.

[47] Yatağanbaba, A., and Kurtbaş, , "Effect of Heating Position on Thermal Energy Storage in Cavity With/Without Open-cell Metallic Foams," *Experimental Heat Transfer*, Vol. 29, No. 3, 2016, pp. 355–377. https://doi.org/10.1080/08916152.2014.989376, URL https://doi.org/10.1080/08916152.2014.989376, publisher: Taylor & Francis _eprint: https://doi.org/10.1080/08916152.2014.989376.

[48] Sarı, A., Alkan, C., Karaipekli, A., and Uzun, O., "Microencapsulated n-octacosane as phase change material for thermal energy storage," *Solar Energy*, Vol. 83, No. 10, 2009, pp. 1757–1763. https://doi.org/10.1016/j.solener.2009.05.008, URL https://www.sciencedirect.com/science/article/pii/S0038092X09001157.

[49] Zhu, Y., Chi, Y., Liang, S., Luo, X., Chen, K., Tian, C., Wang, J., and Zhang, L., "Novel metal coated nanoencapsulated phase change materials with high thermal conductivity for thermal energy storage," *Solar Energy Materials and Solar Cells*, Vol. 176, 2018, pp. 212–221. https://doi.org/10.1016/j.solmat.2017.12.006, URL https://www.sciencedirect.com/science/article/pii/S0927024817306542.

[50] Fang, Y., Liu, X., Liang, X., Liu, H., Gao, X., and Zhang, Z., "Ultrasonic synthesis and characterization of polystyrene/n-dotriacontane composite nanoencapsulated phase change material for thermal energy storage," *Applied Energy*, Vol. 132, 2014, pp. 551–556. https://doi.org/10.1016/j.apenergy.2014.06.056, URL https://www.sciencedirect.com/science/article/pii/S0306261914006382.

[51] Pawar, V. R., and Sobhansarbandi, S., "CFD modeling of a thermal energy storage based heat pipe evacuated tube solar collector," *Journal of Energy Storage*, Vol. 30, 2020, p. 101528. https://doi.org/10.1016/j.est.2020.101528, URL https://www.sciencedirect.com/science/article/pii/S2352152X20301195.

[52] Pawar, V. R., and Sobhansarbandi, S., "Performance Optimization of Thermal Energy Storage Based Solar Collector," American Society of Mechanical Engineers Digital Collection, 2021. https://doi.org/10.1115/POWER2021-64127, URL https://asmedigitalcollection.asme.org/POWER/proceedings/POWER2021/85109/V001T12A005/1115981.

[53] Sharma, A., Tyagi, V. V., Chen, C. R., and Buddhi, D., "Review on thermal energy storage with phase change materials and applications," *Renewable and Sustainable Energy Reviews*, Vol. 13, No. 2, 2009, pp. 318–345. https://doi.org/10.1016/j.rser.2007.10.005, URL https://www.sciencedirect.com/science/article/pii/S1364032107001402.

[54] Pielichowski, K., and Flejtuch, K., "Differential scanning calorimetry studies on poly(ethylene glycol) with different molecular weights for thermal energy storage materials," *Polymers for Advanced Technologies*, Vol. 13, No. 10-12, 2002, pp. 690–696. https://doi.org/10.1002/pat.276, URL https://onlinelibrary.wiley.com/doi/abs/10.1002/pat.276, _eprint: https://onlinelibrary.wiley.com/doi/pdf/10.1002/pat.276.

[55] Pielichowski, K., and Flejtuch, K., "Binary blends of polyethers with fatty acids: A thermal characterization of the phase transitions," *Journal of Applied Polymer Science*, Vol. 90, No. 3, 2003, pp. 861–870. https://doi.org/10.1002/app.12775, URL https://onlinelibrary.wiley.com/doi/10.1002/app.12775.

[56] Nguyen, X. V., "Fabrication and Performance Evaluation of Cold Thermal Energy Storage Tanks Operating in Water Chiller Air Conditioning System," *Energies*, Vol. 14, No. 14, 2021, p. 4159. https://doi.org/10.3390/en14144159, URL https://www.mdpi.com/1996-1073/14/14/4159, number: 14 Publisher: Multidisciplinary Digital Publishing Institute.

[57] Zuo, J., Li, W., and Weng, L., "Thermal performance of caprylic acid/1-dodecanol eutectic mixture as phase change material (PCM)," *Energy and Buildings*, Vol. 43, No. 1, 2011, pp. 207–210. https://doi.org/10.1016/j.enbuild.2010.09.008, URL https://www.sciencedirect.com/science/article/pii/S037877881000318X.

[58] Ali Memon, S., Yiu Lo, T., Shi, X., Barbhuiya, S., and Cui, H., "Preparation, characterization and thermal properties of Lauryl alcohol/Kaolin as novel form-stable composite phase change material for thermal energy storage in buildings," *Applied Thermal Engineering*, Vol. 59, No. 1, 2013, pp. 336–347. https://doi.org/10.1016/j.applthermaleng.2013.05.015, URL https://www.sciencedirect.com/science/article/pii/S1359431113003633.

[59] Kumar, R., Vyas, S., and Dixit, A., "Fatty acids/1-dodecanol binary eutectic phase change materials for low temperature solar thermal applications: Design, development and thermal analysis," *Solar Energy*, Vol. 155, 2017, pp. 1373–1379. https://doi.org/10.1016/j.solener.2017.07.082, URL https://www.sciencedirect.com/science/article/pii/S0038092X17306679.

[60] Philip, N., Raam Dheep, G., and Sreekumar, A., "Cold thermal energy storage with lauryl alcohol and cetyl alcohol eutectic mixture: Thermophysical studies and experimental investigation," *Journal of Energy Storage*, Vol. 27, 2020, p. 101060. https://doi.org/10.1016/j.est.2019.101060, URL https://www.sciencedirect.com/science/article/pii/S2352152X1931120X.

[61] Zuo, J., Li, W., and Weng, L., "Thermal properties of lauric acid/1-tetradecanol binary system for energy storage," *Applied Thermal Engineering*, Vol. 31, No. 6, 2011, pp. 1352–1355. https://doi.org/10.1016/j.applthermaleng.2011.01.008, URL https://www.sciencedirect.com/science/article/pii/S1359431111000172.

[62] Ayaz, H., Chinnasamy, V., Jeon, Y., and Cho, H., "Thermo-physical studies and corrosion analysis of caprylic acid–cetyl alcohol binary mixture as novel phase change material for refrigeration systems," *Energy Reports*, Vol. 8, 2022, pp. 7143–7153. https://doi.org/10.1016/j.egyr.2022.05.239, URL https://www.sciencedirect.com/science/article/pii/S235248472201085X.

[63] Aydın, A. A., and Aydın, A., "High-chain fatty acid esters of 1-hexadecanol for low temperature thermal energy storage with phase change materials," *Solar Energy Materials and Solar Cells*, Vol. 96, 2012, pp. 93–100. https://doi.org/10.1016/j.solmat.2011.09.013, URL https://www.sciencedirect.com/science/article/pii/S0927024811004995.

[64] Veerakumar, C., and Sreekumar, A., "Preparation, Thermophysical Studies, and Corrosion Analysis of a Stable Capric Acid/Cetyl Alcohol Binary Eutectic Phase Change Material for Cold Thermal Energy Storage," *Energy Technology*, Vol. 6, No. 2, 2018, pp. 397–405. https://doi.org/10.1002/ente.201700540, URL https://onlinelibrary.wiley.com/doi/abs/10.1002/ente.201700540, _eprint: https://onlinelibrary.wiley.com/doi/pdf/10.1002/ente.201700540.

[65] Han, S., Kim, C., and Kwon, D., "Thermal/oxidative degradation and stabilization of polyethylene glycol," *Polymer*, Vol. 38, No. 2, 1997, pp. 317–323. https://doi.org/10.1016/S0032-3861(97)88175-X, URL https://www.sciencedirect.com/science/article/pii/S003238619788175X.

[66] Karaman, S., Karaipekli, A., Sarı, A., and Biçer, A., "Polyethylene glycol (PEG)/diatomite composite as a novel form-stable phase change material for thermal energy storage," *Solar Energy Materials and Solar Cells*, Vol. 95, No. 7, 2011, pp. 1647–1653. https://doi.org/10.1016/j.solmat.2011.01.022, URL https://www.sciencedirect.com/science/article/pii/S0927024811000365.

[67] Paberit, R., Rilby, E., Göhl, J., Swenson, J., Refaa, Z., Johansson, P., and Jansson, H., "Cycling Stability of Poly(ethylene glycol) of Six Molecular Weights: Influence of Thermal Conditions for Energy Applications," *ACS Applied Energy Materials*, Vol. 3, No. 11, 2020, pp. 10578–10589. https://doi.org/10.1021/acsaem.0c01621, URL https://pubs.acs.org/doi/10.1021/acsaem.0c01621.

[68] Kou, Y., Wang, S., Luo, J., Sun, K., Zhang, J., Tan, Z., and Shi, Q., "Thermal analysis and heat capacity study of polyethylene glycol (PEG) phase change materials for thermal energy storage applications," *The Journal of Chemical Thermodynamics*, Vol. 128, 2019, pp. 259–274. https://doi.org/

10.1016/j.jct.2018.08.031, URL https://linkinghub.elsevier.com/retrieve/pii/S0021961418304294.

[69] Wang, Y., Tang, B., and Zhang, S., "Single-Walled Carbon Nanotube/Phase Change Material Composites: Sunlight-Driven, Reversible, Form-Stable Phase Transitions for Solar Thermal Energy Storage," *Advanced Functional Materials*, Vol. 23, No. 35, 2013, pp. 4354–4360. https://doi.org/10.1002/adfm.201203728, URL https://onlinelibrary.wiley.com/doi/abs/10.1002/adfm.201203728, _eprint: https://onlinelibrary.wiley.com/doi/pdf/10.1002/adfm.201203728.

[70] Saeed, R. M., Schlegel, J. P., Castano, C., Sawafta, R., and Kuturu, V., "Preparation and thermal performance of methyl palmitate and lauric acid eutectic mixture as phase change material (PCM)," *Journal of Energy Storage*, Vol. 13, 2017, pp. 418–424. https://doi.org/10.1016/j.est.2017.08.005, URL https://www.sciencedirect.com/science/article/pii/S2352152X16301621.

[71] Zhang, H., Zhang, L., Li, Q., Huang, C., Guo, H., Xiong, L., and Chen, X., "Preparation and characterization of methyl palmitate/palygorskite composite phase change material for thermal energy storage in buildings," *Construction and Building Materials*, Vol. 226, 2019, pp. 212–219. https://doi.org/10.1016/j.conbuildmat.2019.07.152, URL https://www.sciencedirect.com/science/article/pii/S0950061819318252.

[72] Hekimoğlu, G., Sarı, A., Kar, T., Keleş, S., Kaygusuz, K., Tyagi, V. V., Sharma, R. K., Al-Ahmed, A., Al-Sulaiman, F. A., and Saleh, T. A., "Walnut shell derived bio-carbon/methyl palmitate as novel composite phase change material with enhanced thermal energy storage properties," *Journal of Energy Storage*, Vol. 35, 2021, p. 102288. https://doi.org/10.1016/j.est.2021.102288, URL https://www.sciencedirect.com/science/article/pii/S2352152X21000529.

[73] Yıldırım, A., "An Ionic Liquid Promoted Clean and Direct Conversion of Triglycerides into Bio-Based Thermal Energy Storage Materials," *European Journal of Lipid Science and Technology*, Vol. 124, No. 6, 2022, p. 2200032. https://doi.org/10.1002/ejlt.202200032, URL https://onlinelibrary.wiley.com/doi/abs/10.1002/ejlt.202200032, _eprint: https://onlinelibrary.wiley.com/doi/pdf/10.1002/ejlt.202200032.

[74] Salman, M., Girault, Y., Balbi, N., and Elegant, L., "Calorimetric study of the reaction between formic acid and N,N,N,N-tetramethylethylenediamine from the aspect of thermal energy storage," *Journal of thermal analysis*, Vol. 37, No. 10, 1991, pp. 2389–2394. https://doi.org/10.1007/BF01913740, URL https://doi.org/10.1007/BF01913740.

[75] Elegant, L., Salman, M., and Schwob, Y., "Calorimetric study of some carboxylic acids lewis-bases complexes in view of thermal energy storage," *Thermochimica Acta*, Vol. 130, 1988, pp. 149–154. https://doi.org/10.1016/0040-6031(88)87060-6, URL https://www.sciencedirect.com/science/article/pii/0040603188870606.

[76] Karaipekli, A., and Sarı, A., "Capric–myristic acid/vermiculite composite as form-stable phase change material for thermal energy storage," *Solar Energy*, Vol. 83, No. 3, 2009, pp. 323–332. https://doi.org/10.1016/j.solener.2008.08.012, URL https://www.sciencedirect.com/science/article/pii/S0038092X08002089.

[77] Wang, L., and Meng, D., "Fatty acid eutectic/polymethyl methacrylate composite as form-stable phase change material for thermal energy storage," *Applied Energy*, Vol. 87, No. 8, 2010, pp. 2660–2665. https://doi.org/10.1016/j.apenergy.2010.01.010, URL https://www.sciencedirect.com/science/article/pii/S0306261910000127.

[78] Keleş, S., Kaygusuz, K., and Sarı, A., "Lauric and myristic acids eutectic mixture as phase change material for low-temperature heating applications," *International Journal of Energy Research*, Vol. 29, No. 9, 2005, pp. 857–870. https://doi.org/10.1002/er.1111, URL https://onlinelibrary.wiley.com/doi/abs/10.1002/er.1111, _eprint: https://onlinelibrary.wiley.com/doi/pdf/10.1002/er.1111.

[79] Lv, Y., Jin, W., Yang, Y., Zhang, H., Zhang, X., Ding, F., and Zhou, W., "Experimental thermal storage research of organic binary phase change materials in building environment," *International Journal of Green Energy*, Vol. 14, No. 11, 2017, pp. 916–924. https://doi.org/10.1080/15435075.2017.1339042, URL https://doi.org/10.1080/15435075.2017.1339042, publisher: Taylor & Francis _eprint: https://doi.org/10.1080/15435075.2017.1339042.

[80] Genc, Z. K., Canbay, C. A., Acar, S. S., Sekerci, M., and Genc, M., "Preparation and thermal properties of heterogeneous composite phase change materials based on camphene–palmitic acid," *Journal of Thermal Analysis and Calorimetry*, Vol. 120, No. 3, 2015, pp. 1679–1688. https://doi.org/10.1007/s10973-015-4478-3, URL https://doi.org/10.1007/s10973-015-4478-3.

[81] Hoseini, Z., and Nikje, M. M. A., "The Preparation of Novel Microcapsules Based on Palmitic Acid Core and Waterborne Polyurethane/Silane Shell as Phase Change Materials for Thermal Energy Storage," *Journal of Polymers and the Environment*, Vol. 29, No. 3, 2021, pp. 821–828. https://doi.org/10.1007/s10924-020-01916-3, URL https://doi.org/10.1007/s10924-020-01916-3.

[82] Jaya Krishna, D., and Kochar, S., "The Metallographic Study of Corrosion of Metals with Latent Heat Storage Materials Suitable for Solar Hot Water System," *Transactions of the Indian Ceramic Society*, Vol. 76, No. 2, 2017, pp. 133–141. https://doi.org/10.1080/0371750X.2016.1268072, URL https://

doi.org/10.1080/0371750X.2016.1268072, publisher: Taylor & Francis _eprint: https://doi.org/10.1080/0371750X.2016.1268072.

[83] Canbay, C. A., Genc, Z. K., Acar, S. S., Sekerci, M., and Genc, M., "Preparation and Thermodynamic Properties of Camphene/Stearic Acid Composites as Phase-Change Materials in Buildings," *International Journal of Thermophysics*, Vol. 35, No. 8, 2014, pp. 1526–1537. https://doi.org/10.1007/s10765-014-1724-z, URL https://doi.org/10.1007/s10765-014-1724-z.

[84] Ma, G., Wang, Z., Xie, S., Sun, J., Jia, Y., Jing, Y., and Du, G., "Preparation and Properties of Stearic Acid–Acetanilide Eutectic Mixture/Expanded Graphite Composite Phase-Change Material for Thermal Energy Storage," *Energy Technology*, Vol. 6, No. 1, 2018, pp. 153–160. https://doi.org/10.1002/ente.201700352, URL https://onlinelibrary.wiley.com/doi/abs/10.1002/ente.201700352, _eprint: https://onlinelibrary.wiley.com/doi/pdf/10.1002/ente.201700352.

[85] Ma, G., Sun, J., Zhang, Y., Jing, Y., and Jia, Y., "A novel low-temperature phase change material based on stearic acid and hexanamide eutectic mixture for thermal energy storage," *Chemical Physics Letters*, Vol. 714, 2019, pp. 166–171. https://doi.org/10.1016/j.cplett.2018.11.003, URL https://www.sciencedirect.com/science/article/pii/S0009261418309175.

[86] Ma, G., Sun, J., Zhang, Y., Jing, Y., and Jia, Y., "Preparation and thermal properties of stearic acid-benzamide eutectic mixture/expanded graphite composites as phase change materials for thermal energy storage," *Powder Technology*, Vol. 342, 2019, pp. 131–140. https://doi.org/10.1016/j.powtec.2018.09.074, URL https://www.sciencedirect.com/science/article/pii/S0032591018308015.

[87] Mishra, A. K., Lahiri, B. B., and Philip, J., "Thermal conductivity enhancement in organic phase change material (phenol-water system) upon addition of Al2O3, SiO2 and TiO2 nano-inclusions," *Journal of Molecular Liquids*, Vol. 269, 2018, pp. 47–63. https://doi.org/10.1016/j.molliq.2018.08.001, URL https://www.sciencedirect.com/science/article/pii/S0167732218327831.

[88] Ganapathi, G. B., and Wirz, R., "High Density Thermal Energy Storage With Supercritical Fluids," American Society of Mechanical Engineers Digital Collection, 2013, pp. 699–707. https://doi.org/10.1115/ES2012-91008, URL https://turbomachinery.asmedigitalcollection.asme.org/ES/proceedings/ES2012/44816/699/232235.

[89] Yang, L., Peng, H., Ling, X., and Dong, H., "Numerical analysis on performance of naphthalene phase change thermal storage system in aluminum plate-fin unit," *Heat and Mass Transfer*, Vol. 51, No. 2, 2015, pp. 195–207. https://doi.org/10.1007/s00231-014-1400-7, URL https://doi.org/10.1007/s00231-014-1400-7.

[90] Dinker, A., Agarwal, M., and Agarwal, G. D., "Modelling and Simulation of Helical Coil Embedded Heat Storage Unit Using Beeswax/Expanded Graphite Composite as Phase Change Material," *Mathematical Modeling, Computational Intelligence Techniques and Renewable Energy*, edited by M. Sahni, J. M. Merigó, B. K. Jha, and R. Verma, Springer, Singapore, 2021, pp. 411–423. https://doi.org/10.1007/978-981-15-9953-8_36.

[91] Wang, J., Han, W., Ge, C., Guan, H., Yang, H., and Zhang, X., "Form-stable oxalic acid dihydrate/glycolic acid-based composite PCMs for thermal energy storage," *Renewable Energy*, Vol. 136, 2019, pp. 657–663. https://doi.org/10.1016/j.renene.2019.01.063, URL https://www.sciencedirect.com/science/article/pii/S0960148119300631.

[92] Lennartson, A., Roffey, A., and Moth-Poulsen, K., "Designing photoswitches for molecular solar thermal energy storage," *Tetrahedron Letters*, Vol. 56, No. 12, 2015, pp. 1457–1465. https://doi.org/10.1016/j.tetlet.2015.01.187, URL https://www.sciencedirect.com/science/article/pii/S0040403915002373.

[93] Raam Dheep, G., and Sreekumar, A., "Thermal reliability and corrosion characteristics of an organic phase change materials for solar space heating applications," *Journal of Energy Storage*, Vol. 23, 2019, pp. 98–105. https://doi.org/10.1016/j.est.2019.03.009, URL https://www.sciencedirect.com/science/article/pii/S2352152X19300520.

[94] Wang, A., Chen, C., and Xu, G., "Silica/Acetamide Composite as Form-Stable Phase Change Material for Latent Heat Thermal Energy Storage," *Journal of Advanced Microscopy Research*, Vol. 7, No. 4, 2012, pp. 286–291. https://doi.org/10.1166/jamr.2012.1128.

[95] Xia, L., and Zhang, P., "Thermal property measurement and heat transfer analysis of acetamide and acetamide/expanded graphite composite phase change material for solar heat storage," *Solar Energy Materials and Solar Cells*, Vol. 95, No. 8, 2011, pp. 2246–2254. https://doi.org/10.1016/j.solmat.2011.03.031, URL https://www.sciencedirect.com/science/article/pii/S092702481100184X.

[96] Dheep, G. R., and Sreekumar, A., "Investigation on thermal reliability and corrosion characteristics of glutaric acid as an organic phase change material for solar thermal energy storage applications," *Applied Thermal Engineering*, Vol. 129, 2018, pp. 1189–1196. https://doi.org/10.1016/j.applthermaleng.2017.10.133, URL https://www.sciencedirect.com/science/article/pii/S1359431117317337.

[97] Purohit, K., Murty, V. V. S., Dixit, R. C., and Sharma, A., "Development of an acetanilide/benzoic acid eutectic phase change material based thermal energy storage unit for a passive water heating system," *Bulletin of Materials Science*, Vol. 42, No. 3, 2019, p. 119. https://doi.org/10.1007/s12034-019-1731-6, URL https://doi.org/10.1007/s12034-019-1731-6.

[98] Saini, G., Singh, H., Saini, K., and Yadav, A., "Experimental investigation of the solar cooker during sunshine and off-sunshine hours using the thermal energy storage unit based on a parabolic trough collector," *International Journal of Ambient Energy*, Vol. 37, No. 6, 2016, pp. 597–608. https://doi.org/10.1080/01430750.2015.1023836, URL https://doi.org/10.1080/01430750.2015.1023836, publisher: Taylor & Francis _eprint: https://doi.org/10.1080/01430750.2015.1023836.

[99] Raam Dheep, G., and Sreekumar, A., "Influence of accelerated thermal charging and discharging cycles on thermo-physical properties of organic phase change materials for solar thermal energy storage applications," *Energy Conversion and Management*, Vol. 105, 2015, pp. 13–19. https://doi.org/10.1016/j.enconman.2015.07.040, URL https://www.sciencedirect.com/science/article/pii/S0196890415006913.

[100] Myers, P. D., and Goswami, D. Y., "Thermal energy storage using chloride salts and their eutectics," *Applied Thermal Engineering*, Vol. 109, 2016, pp. 889–900. https://doi.org/10.1016/j.applthermaleng.2016.07.046, URL https://www.sciencedirect.com/science/article/pii/S1359431116311759.

[101] Jiang, Y., Liu, M., and Sun, Y., "Review on the development of high temperature phase change material composites for solar thermal energy storage," *Solar Energy Materials and Solar Cells*, Vol. 203, 2019, p. 110164.

https://doi.org/10.1016/j.solmat.2019.110164, URL https://linkinghub.elsevier.com/retrieve/pii/S0927024819304933.

[102] Jiang, Y., Sun, Y., Liu, M., Bruno, F., and Li, S., "Eutectic Na2CO3–NaCl salt: A new phase change material for high temperature thermal storage," *Solar Energy Materials and Solar Cells*, Vol. 152, 2016, pp. 155–160. https://doi.org/10.1016/j.solmat.2016.04.002, URL https://linkinghub.elsevier.com/retrieve/pii/S0927024816300149.

[103] Liu, M., Gomez, J., Turchi, C., Tay, N., Saman, W., and Bruno, F., "Determination of thermo-physical properties and stability testing of high-temperature phase-change materials for CSP applications," *Solar Energy Materials and Solar Cells*, Vol. 139, 2015, pp. 81–87. https://doi.org/10.1016/j.solmat.2015.03.014, URL https://linkinghub.elsevier.com/retrieve/pii/S0927024815001257.

[104] Kenisarin, M. M., "High-temperature phase change materials for thermal energy storage," *Renewable and Sustainable Energy Reviews*, Vol. 14, No. 3, 2010, pp. 955–970. https://doi.org/10.1016/j.rser.2009.11.011, URL https://linkinghub.elsevier.com/retrieve/pii/S1364032109002731.

[105] Hasnain, S. M., "Review on sustainable thermal energy storage technologies, Part I: heat storage materials and techniques," *Energy Conversion and Management*, Vol. 39, No. 11, 1998, pp. 1127–1138. https://doi.org/10.1016/S0196-8904(98)00025-9, URL https://www.sciencedirect.com/science/article/pii/S0196890498000259.

[106] Beaupere, N., Soupremanien, U., and Zalewski, L., "Nucleation triggering methods in supercooled phase change materials (PCM), a review," *Ther-*

mochimica Acta, Vol. 670, 2018, pp. 184–201. https://doi.org/10.1016/j.tca.2018.10.009.

[107] Belton, G., and Ajami, F., "Thermochemistry of salt hydrates," Tech. rep., United States, May 1973. URL https://www.osti.gov/biblio/5102836.

[108] Günther, E., Mehling, H., and Werner, M., "Melting and nucleation temperatures of three salt hydrate phase change materials under static pressures up to 800 MPa," *Journal of Physics D: Applied Physics*, Vol. 40, No. 15, 2007, pp. 4636–4641. https://doi.org/10.1088/0022-3727/40/15/042, URL https://iopscience.iop.org/article/10.1088/0022-3727/40/15/042.

[109] Ryu, H. W., Woo, S. W., Shin, B. C., and Kim, S. D., "Prevention of supercooling and stabilization of inorganic salt hydrates as latent heat storage materials," *Solar Energy Materials and Solar Cells*, Vol. 27, No. 2, 1992, pp. 161–172. https://doi.org/10.1016/0927-0248(92)90117-8, URL https://www.sciencedirect.com/science/article/pii/0927024892901178.

[110] Byung Chul Shin, Sang Done Kim, and Won-Hoon, P., "Phase separation and supercooling of a latent heat-storage material," *Energy*, Vol. 14, No. 12, 1989, pp. 921–930. https://doi.org/10.1016/0360-5442(89)90047-9, URL https://www.sciencedirect.com/science/article/pii/0360544289900479.

[111] Li, M., Wang, W., Zhang, Z., He, F., Yan, S., Yan, P.-J., Xie, R., Ju, X.-J., Liu, Z., and Chu, L.-Y., "Monodisperse Na $_2$ SO $_4$ ·10H $_2$ O@SiO $_2$ Microparticles against Supercooling and Phase Separation during Phase Change for Efficient Energy Storage," *Industrial & Engineering Chemistry Research*, Vol. 56, No. 12, 2017, pp. 3297–3308. https://doi.org/10.1021/acs.iecr.7b00231, URL https://pubs.acs.org/doi/10.1021/acs.iecr.7b00231.

[112] Marks, S., "An investigation of the thermal energy storage capacity of

Glauber's salt with respect to thermal cycling," *Solar Energy*, Vol. 25, No. 3, 1980, pp. 255–258. https://doi.org/10.1016/0038-092X(80)90332-1, URL https://www.sciencedirect.com/science/article/pii/0038092X80903321.

[113] Naumann, R., and Emons, H.-H., "Results of thermal analysis for investigation of salt hydrates as latent heat-storage materials," *Journal of Thermal Analysis*, Vol. 35, No. 3, 1989, pp. 1009–1031. https://doi.org/10.1007/BF02057256.

[114] Khudhair, A. M., and Farid, M. M., "A review on energy conservation in building applications with thermal storage by latent heat using phase change materials," *Energy Conversion and Management*, Vol. 45, No. 2, 2004, pp. 263–275. https://doi.org/10.1016/S0196-8904(03)00131-6, URL https://www.sciencedirect.com/science/article/pii/S0196890403001316.

[115] PARIS, J., FALARDEAU, M., and VILLENEUVE, C., "Thermal Storage by Latent Heat: A Viable Option for Energy Conservation in Buildings," *Energy Sources*, Vol. 15, No. 1, 1993, pp. 85–93. https://doi.org/10.1080/00908319308909014, URL https://doi.org/10.1080/00908319308909014, publisher: Taylor & Francis _eprint: https://doi.org/10.1080/00908319308909014.

[116] Nagano, K., Mochida, T., Takeda, S., Domański, R., and Rebow, M., "Thermal characteristics of manganese (II) nitrate hexahydrate as a phase change material for cooling systems," *Applied Thermal Engineering*, Vol. 23, No. 2, 2003, pp. 229–241. https://doi.org/10.1016/S1359-4311(02)00161-8, URL https://www.sciencedirect.com/science/article/pii/S1359431102001618.

[117] Cabeza, L. F., Svensson, G., Hiebler, S., and Mehling, H., "Thermal performance of sodium acetate trihydrate thickened with different materials as phase change energy storage material," *Applied Thermal Engineering*, Vol. 23,

No. 13, 2003, pp. 1697–1704. https://doi.org/10.1016/S1359-4311(03)00107-8, URL https://www.sciencedirect.com/science/article/pii/S1359431103001078.

[118] Medrano, M., Yilmaz, S., Sheth, F. K., Martorell, I., Paksoy, H. O., and Cabeza, L. F., "Salt Water Solutions as PCM for Cooling Applications," *Proceedings of the EuroSun 2010 Conference*, International Solar Energy Society, Graz, Austria, 2010, pp. 1–8. https://doi.org/10.18086/eurosun.2010.16.20, URL http://proceedings.ises.org/citation?doi=eurosun.2010.16.20.

[119] Mo, S., Chen, Y., Jia, L., and Luo, X., "Reduction of supercooling of water by TiO2 nanoparticles as observed using differential scanning calorimeter," *Journal of Experimental Nanoscience*, Vol. 8, No. 4, 2013, pp. 533–539. https://doi.org/10.1080/17458080.2011.572085, URL https://doi.org/10.1080/17458080.2011.572085, publisher: Taylor & Francis _eprint: https://doi.org/10.1080/17458080.2011.572085.

[120] Lee, J.-H., Hwang, K. S., Jang, S. P., Lee, B. H., Kim, J. H., Choi, S. U. S., and Choi, C. J., "Effective viscosities and thermal conductivities of aqueous nanofluids containing low volume concentrations of Al2O3 nanoparticles," *International Journal of Heat and Mass Transfer*, Vol. 51, No. 11, 2008, pp. 2651–2656. https://doi.org/10.1016/j.ijheatmasstransfer.2007.10.026, URL https://www.sciencedirect.com/science/article/pii/S0017931007006680.

[121] Zhu, S., Nguyen, M. T., and Yonezawa, T., "Micro- and nano-encapsulated metal and alloy-based phase-change materials for thermal energy storage," *Nanoscale Advances*, Vol. 3, No. 16, 2021, pp. 4626–4645. https://doi.org/10.1039/D0NA01008A, URL http://xlink.rsc.org/?DOI=D0NA01008A.

[122] Pan, A., Wang, J., and Zhang, X., "Prediction of Melting Temperature and Latent Heat for Low-melting Metal PCMs," *Rare Metal Materials and En-*

gineering, Vol. 45, No. 4, 2016, pp. 874–880. https://doi.org/10.1016/S1875-5372(16)30091-1, URL https://www.sciencedirect.com/science/article/pii/S1875537216300911.

[123] Ge, H., Li, H., Mei, S., and Liu, J., "Low melting point liquid metal as a new class of phase change material: An emerging frontier in energy area," *Renewable and Sustainable Energy Reviews*, Vol. 21, No. C, 2013, pp. 331–346. URL https://ideas.repec.org/a/eee/rensus/v21y2013icp331-346.html, publisher: Elsevier.

[124] Su, W., Darkwa, J., and Kokogiannakis, G., "Review of solid-liquid phase change materials and their encapsulation technologies," *Faculty of Engineering and Information Sciences - Papers: Part A*, 2015, pp. 373–391. https://doi.org/10.1016/j.rser.2015.04.044, URL https://ro.uow.edu.au/eispapers/3985.

[125] Manasijević, I., Balanović, L., Grgurić, T. H., Minić, D., and Gorgievski, M., "Study of Microstructure and Thermal Properties of the Low Melting Bi-In-Sn Eutectic Alloys," *Materials Research*, Vol. 21, 2018. https://doi.org/10.1590/1980-5373-MR-2018-0501, URL http://www.scielo.br/j/mr/a/5dqMfGQGmqvvvyzzbMNgt3F/?lang=en, publisher: ABM, ABC, ABPol.

[126] Wang, Q.-M., Cheng, X.-M., Li, Y.-Y., Yu, G.-M., and Liu, Z., "Microstructures and thermal properties of Sn–Bi–Pb–Zn alloys as heat storage and transfer materials," *Rare Metals*, Vol. 38, No. 4, 2019, pp. 350–358. https://doi.org/10.1007/s12598-019-01206-5, URL https://doi.org/10.1007/s12598-019-01206-5.

[127] "Lead, Pb," , ????. URL https://www.matweb.com/search/DataSheet.aspx?MatGUID=ebd6d2cdfdca4fc285885cc4749c36b1&ckck=1.

[128] "Cadmium, Cd," , ????. URL https://www.matweb.com/search/datasheet.aspx?matguid=ca862f5c59594be3b9a2d250460d2dba&n=1.

[129] Raud, R., Jacob, R., Bruno, F., Will, G., and Steinberg, T. A., "A critical review of eutectic salt property prediction for latent heat energy storage systems," *Renewable and Sustainable Energy Reviews*, Vol. 70, 2017, pp. 936–944. https://doi.org/10.1016/j.rser.2016.11.274, URL https://www.sciencedirect.com/science/article/pii/S1364032116310553.

[130] Hadiya, J., and Shukla, A. K. N., "Thermal energy storage using phase change materials: a way forward," *International Journal of Global Energy Issues*, Vol. 41, No. 1-4, 2018, pp. 108–127. https://doi.org/10.1504/IJGEI.2018.092311, URL https://www.inderscienceonline.com/doi/abs/10.1504/IJGEI.2018.092311, publisher: Inderscience Publishers.

[131] Li, D., Wu, Y., Wang, B., Liu, C., and Arıcı, M., "Optical and thermal performance of glazing units containing PCM in buildings: A review," *Construction and Building Materials*, Vol. 233, 2020, p. 117327. https://doi.org/10.1016/j.conbuildmat.2019.117327, URL https://www.sciencedirect.com/science/article/pii/S0950061819327795.

[132] Diarce, G., Quant, L., Campos-Celador, , Sala, J. M., and García-Romero, A., "Determination of the phase diagram and main thermophysical properties of the erythritol–urea eutectic mixture for its use as a phase change material," *Solar Energy Materials and Solar Cells*, Vol. 157, 2016, pp. 894–906. https://doi.org/10.1016/j.solmat.2016.08.016, URL https://www.sciencedirect.com/science/article/pii/S0927024816303075.

[133] Heckenkamp, J., and Baumann, H., "Latentwärmespeicher," *Sonderdruck Aus Nachrichten*, Vol. 11, 1997, pp. 1075–1081.

[134] Bland, A., Khzouz, M., Statheros, T., and Gkanas, E. I., "PCMs for Residential Building Applications: A Short Review Focused on Disadvantages and Proposals for Future Development," *Buildings*, Vol. 7, No. 3, 2017, p. 78. https://doi.org/10.3390/buildings7030078, URL https://www.mdpi.com/2075-5309/7/3/78, number: 3 Publisher: Multidisciplinary Digital Publishing Institute.

[135] Kalnæs, S. E., and Jelle, B. P., "Phase change materials and products for building applications: A state-of-the-art review and future research opportunities," *Energy and Buildings*, Vol. 94, 2015, pp. 150–176. https://doi.org/10.1016/j.enbuild.2015.02.023, URL https://www.sciencedirect.com/science/article/pii/S0378778815001188.

[136] Mavrigiannaki, A., and Ampatzi, E., "Latent heat storage in building elements: A systematic review on properties and contextual performance factors," *Renewable and Sustainable Energy Reviews*, Vol. 60, 2016, pp. 852–866. https://doi.org/10.1016/j.rser.2016.01.115, URL https://www.sciencedirect.com/science/article/pii/S1364032116001453.

[137] Akeiber, H., Nejat, P., Majid, M. Z. A., Wahid, M. A., Jomehzadeh, F., Zeynali Famileh, I., Calautit, J. K., Hughes, B. R., and Zaki, S. A., "A review on phase change material (PCM) for sustainable passive cooling in building envelopes," *Renewable and Sustainable Energy Reviews*, Vol. 60, 2016, pp. 1470–1497. https://doi.org/10.1016/j.rser.2016.03.036, URL https://www.sciencedirect.com/science/article/pii/S1364032116002719.

[138] Paranjothi, G., Odukomaiya, A., Cui, S., and Bulk, A., "Evaluation of

phase change plaster/paste composites for building envelopes," *Energy and Buildings*, Vol. 253, 2021, p. 111372. https://doi.org/10.1016/j.enbuild.2021.111372, URL https://www.sciencedirect.com/science/article/pii/S0378778821006563.

[139] Arumugam, P., Ramalingam, V., and Vellaichamy, P., "Effective PCM, insulation, natural and/or night ventilation techniques to enhance the thermal performance of buildings located in various climates – A review," *Energy and Buildings*, Vol. 258, 2022, p. 111840. https://doi.org/10.1016/j.enbuild.2022.111840, URL https://www.sciencedirect.com/science/article/pii/S0378778822000111.

[140] Mukram, T. A., and Daniel, J., "A review of novel methods and current developments of phase change materials in the building walls for cooling applications," *Sustainable Energy Technologies and Assessments*, Vol. 49, 2022, p. 101709. https://doi.org/10.1016/j.seta.2021.101709, URL https://www.sciencedirect.com/science/article/pii/S2213138821007232.

[141] Buswell, R. A., Leal de Silva, W. R., Jones, S. Z., and Dirrenberger, J., "3D printing using concrete extrusion: A roadmap for research," *Cement and Concrete Research*, Vol. 112, 2018, pp. 37–49. https://doi.org/10.1016/j.cemconres.2018.05.006, URL https://www.sciencedirect.com/science/article/pii/S0008884617311924.

[142] Gencel, O., Sarı, A., Kaplan, G., Ustaoglu, A., Hekimoğlu, G., Bayraktar, O. Y., and Ozbakkaloglu, T., "Properties of eco-friendly foam concrete containing PCM impregnated rice husk ash for thermal management of buildings," *Journal of Building Engineering*, Vol. 58, 2022, p. 104961. https://doi.org/10.1016/j.jobe.2022.104961, URL https://www.sciencedirect.com/science/article/pii/S235271022200972X.

[143] Omara, A. A. M., Mohammed, H. A., Al Rikabi, I. J., Abuelnour, M. A., and Abuelnuor, A. A. A., "Performance improvement of solar chimneys using phase change materials: A review," *Solar Energy*, Vol. 228, 2021, pp. 68–88. https://doi.org/10.1016/j.solener.2021.09.037, URL https://www.sciencedirect.com/science/article/pii/S0038092X21007945.

[144] Teamah, H. M., and Teamah, M., "Integration of phase change material in flat plate solar water collector: A state of the art, opportunities, and challenges," *Journal of Energy Storage*, Vol. 54, 2022, p. 105357. https://doi.org/10.1016/j.est.2022.105357, URL https://www.sciencedirect.com/science/article/pii/S2352152X22013512.

[145] Kośny, J., Biswas, K., Miller, W., and Kriner, S., "Field thermal performance of naturally ventilated solar roof with PCM heat sink," *Solar Energy*, Vol. 86, No. 9, 2012, pp. 2504–2514. https://doi.org/10.1016/j.solener.2012.05.020, URL https://www.sciencedirect.com/science/article/pii/S0038092X12001983.

[146] Tan, P., Lindberg, P., Eichler, K., Löveryd, P., Johansson, P., and Kalagasidis, A. S., "Thermal energy storage using phase change materials: Techno-economic evaluation of a cold storage installation in an office building," *Applied Energy*, Vol. 276, 2020, p. 115433. https://doi.org/10.1016/j.apenergy.2020.115433, URL https://www.sciencedirect.com/science/article/pii/S0306261920309454.

[147] Goyal, A., Kozubal, E., Woods, J., Nofal, M., and Al-Hallaj, S., "Design and performance evaluation of a dual-circuit thermal energy storage module for air conditioners," *Applied Energy*, Vol. 292, 2021, p. 116843. https://doi.org/10.1016/j.apenergy.2021.116843, URL https://www.sciencedirect.com/science/article/pii/S030626192100338X.

[148] Cui, S., Odukomaiya, A., and Vidal, J., "Materials research and development needs to enable efficient and electrified buildings," *MRS Bulletin*, Vol. 46, No. 12, 2021, pp. 1176–1186. https://doi.org/10.1557/s43577-021-00241-x, URL https://doi.org/10.1557/s43577-021-00241-x.

[149] Aljehani, A., Razack, S. A. K., Nitsche, L., and Al-Hallaj, S., "Design and optimization of a hybrid air conditioning system with thermal energy storage using phase change composite," *Energy Conversion and Management*, Vol. 169, 2018, pp. 404–418. https://doi.org/10.1016/j.enconman.2018.05.040, URL https://www.sciencedirect.com/science/article/pii/S019689041830517X.

[150] Ding, Z., Wu, W., and Leung, M., "Advanced/hybrid thermal energy storage technology: material, cycle, system and perspective," *Renewable and Sustainable Energy Reviews*, Vol. 145, 2021, p. 111088. https://doi.org/10.1016/j.rser.2021.111088, URL https://www.sciencedirect.com/science/article/pii/S1364032121003762.

[151] Rasouli, E., Fricke, E., and Narayanan, V., "High efficiency 3-D printed microchannel polymer heat exchangers for air conditioning applications," *Science and Technology for the Built Environment*, Vol. 28, No. 3, 2022, pp. 289–306. https://doi.org/10.1080/23744731.2022.2026693, URL https://doi.org/10.1080/23744731.2022.2026693, publisher: Taylor & Francis _eprint: https://doi.org/10.1080/23744731.2022.2026693.

[152] Wang, F., Maidment, G., Missenden, J., and Tozer, R., "The novel use of phase change materials in refrigeration plant. Part 1: Experimental investigation," *Applied Thermal Engineering*, Vol. 27, No. 17, 2007, pp. 2893–2901. https://doi.org/10.1016/j.applthermaleng.2005.06.011, URL https://www.sciencedirect.com/science/article/pii/S1359431105001948.

[153] Barzin, R., Chen, J. J. J., Young, B. R., and Farid, M. M., "Application of PCM underfloor heating in combination with PCM wallboards for space heating using price based control system," *Applied Energy*, Vol. 148, 2015, pp. 39–48. https://doi.org/10.1016/j.apenergy.2015.03.027, URL https://www.sciencedirect.com/science/article/pii/S0306261915003116.

[154] Arsana, M. E., Temaja, I. W., Widiantara, I. B. G., and Sukadana, I. B. P., "Corn oil phase change material (PCM) in frozen food cooling machine to improve energy efficiency," *Journal of Physics: Conference Series*, Vol. 1450, No. 1, 2020, p. 012107. https://doi.org/10.1088/1742-6596/1450/1/012107, URL https://dx.doi.org/10.1088/1742-6596/1450/1/012107, publisher: IOP Publishing.

[155] Nair, A. M., Wilson, C., Huang, M. J., Griffiths, P., and Hewitt, N., "Phase change materials in building integrated space heating and domestic hot water applications: A review," *Journal of Energy Storage*, Vol. 54, 2022, p. 105227. https://doi.org/10.1016/j.est.2022.105227, URL https://www.sciencedirect.com/science/article/pii/S2352152X22012269.

[156] Faraj, K., Faraj, J., Hachem, F., Bazzi, H., Khaled, M., and Castelain, C., "Analysis of underfloor electrical heating system integrated with coconut oil-PCM plates," *Applied Thermal Engineering*, Vol. 158, 2019, p. 113778. https://doi.org/10.1016/j.applthermaleng.2019.113778, URL https://www.sciencedirect.com/science/article/pii/S1359431119309779.

[157] Zhou, G., and He, J., "Thermal performance of a radiant floor heating system with different heat storage materials and heating pipes," *Applied Energy*, Vol. 138, 2015, pp. 648–660. https://doi.org/10.1016/j.apenergy.2014.10.058, URL https://www.sciencedirect.com/science/article/pii/S0306261914011088.

[158] Lu, S., Xu, B., and Tang, X., "Experimental study on double pipe PCM floor heating system under different operation strategies," *Renewable Energy*, Vol. 145, 2020, pp. 1280–1291. https://doi.org/10.1016/j.renene.2019.06.086, URL https://www.sciencedirect.com/science/article/pii/S0960148119309255.

[159] Cabeza, L. F., Ibáñez, M., Solé, C., Roca, J., and Nogués, M., "Experimentation with a water tank including a PCM module," *Solar Energy Materials and Solar Cells*, Vol. 90, No. 9, 2006, pp. 1273–1282. https://doi.org/10.1016/j.solmat.2005.08.002, URL https://www.sciencedirect.com/science/article/pii/S0927024805002461.

[160] Mehling, H., Cabeza, L. F., Hippeli, S., and Hiebler, S., "PCM-module to improve hot water heat stores with stratification," *Renewable Energy*, Vol. 28, No. 5, 2003, pp. 699–711. https://doi.org/10.1016/S0960-1481(02)00108-8, URL https://www.sciencedirect.com/science/article/pii/S0960148102001088.

[161] Wang, Z., Zhang, H., Dou, B., Zhang, G., Wu, W., and Zhou, L., "An experimental study for the enhancement of stratification in heat-storage tank by equalizer and PCM module," *Journal of Energy Storage*, Vol. 27, 2020, p. 101010. https://doi.org/10.1016/j.est.2019.101010, URL https://www.sciencedirect.com/science/article/pii/S2352152X19303718.

[162] Long, J.-Y., and Zhu, D.-S., "Numerical and experimental study on heat pump water heater with PCM for thermal storage," *Energy and Buildings*, Vol. 40, No. 4, 2008, pp. 666–672. https://doi.org/10.1016/j.enbuild.2007.05.001, URL https://www.sciencedirect.com/science/article/pii/S0378778807001508.

[163] da Cunha, J. P., and Eames, P., "Compact latent heat storage decarbonisation potential for domestic hot water and space heating applications in

the UK," *Applied Thermal Engineering*, Vol. 134, 2018, pp. 396–406. https://doi.org/10.1016/j.applthermaleng.2018.01.120, URL https://www.sciencedirect.com/science/article/pii/S135943111733586X.

[164] Fadl, M., and Eames, P. C., "An experimental investigation of the heat transfer and energy storage characteristics of a compact latent heat thermal energy storage system for domestic hot water applications," *Energy*, Vol. 188, 2019, p. 116083. https://doi.org/10.1016/j.energy.2019.116083, URL https://www.sciencedirect.com/science/article/pii/S0360544219317785.

[165] Gluesenkamp, K. R., and Sultan, S., "Heat Pumping Technologies Magazine - The State of Art of Heat-Pump integrated Thermal Energy Storage for Demand Response," 2021. https://doi.org/10.23697/62TR-NT79, URL https://heatpumpingtechnologies.org/publications/the-state-of-art-of-heat-pump-integrated-thermal-energy-storage-for-demand-response/, publisher: Heat Pump Centre.

[166] Ling, Z., Zhang, Z., Shi, G., Fang, X., Wang, L., Gao, X., Fang, Y., Xu, T., Wang, S., and Liu, X., "Review on thermal management systems using phase change materials for electronic components, Li-ion batteries and photovoltaic modules," *Renewable and Sustainable Energy Reviews*, Vol. 31, 2014, pp. 427–438. https://doi.org/10.1016/j.rser.2013.12.017, URL https://www.sciencedirect.com/science/article/pii/S1364032113008319.

[167] E. Green, C., G. Fedorov, A., and K. Joshi, Y., "Time scale matching of dynamically operated devices using composite thermal capacitors," *Microelectronics Journal*, Vol. 45, No. 8, 2014, pp. 1069–1078. https://doi.org/10.1016/j.mejo.2014.05.013, URL https://www.sciencedirect.com/science/article/pii/S0026269214001724.

[168] Babu Sanker, S., and Baby, R., "Phase change material based thermal management of lithium ion batteries: A review on thermal performance of various thermal conductivity enhancers," *Journal of Energy Storage*, Vol. 50, 2022, p. 104606. https://doi.org/10.1016/j.est.2022.104606, URL https://www.sciencedirect.com/science/article/pii/S2352152X22006223.

[169] Mills, A., Farid, M., Selman, J. R., and Al-Hallaj, S., "Thermal conductivity enhancement of phase change materials using a graphite matrix," *Applied Thermal Engineering*, Vol. 26, No. 14, 2006, pp. 1652–1661. https://doi.org/10.1016/j.applthermaleng.2005.11.022, URL https://www.sciencedirect.com/science/article/pii/S1359431105004072.

[170] Mathew, J., and Krishnan, S., "A Review on Transient Thermal Management of Electronic Devices," *Journal of Electronic Packaging*, Vol. 144, No. 1, 2021. https://doi.org/10.1115/1.4050002, URL https://doi.org/10.1115/1.4050002.

[171] Humphries, W. R., and Griggs, E. I., "A design handbook for phase change thermal control and energy storage devices," , Nov. 1977. URL https://ntrs.nasa.gov/citations/19780007491, nTRS Author Affiliations: NASA Marshall Space Flight Center NTRS Report/Patent Number: NASA-TP-1074 NTRS Document ID: 19780007491 NTRS Research Center: Legacy CDMS (CDMS).

[172] Xu, J., Tarau, C., Ellis, M., and Alvarez-Hernandez, A., "Design of an Additively Manufactured Vapor Chamber Heat Exchanger for Space Applications," *2021 20th IEEE Intersociety Conference on Thermal and Thermomechanical Phenomena in Electronic Systems (iTherm)*, 2021, pp. 1091–1097. https://doi.org/10.1109/ITherm51669.2021.9503233, iSSN: 2694-2135.

[173] Nafis, B. M., Whitt, R., Iradukunda, A.-C., and Huitink, D., "Additive Manufacturing for Enhancing Thermal Dissipation in Heat Sink Implementa-

tion: A Review," *Heat Transfer Engineering*, Vol. 42, No. 12, 2021, pp. 967–984. https://doi.org/10.1080/01457632.2020.1766246, URL https://doi.org/10.1080/01457632.2020.1766246, publisher: Taylor & Francis _eprint: https://doi.org/10.1080/01457632.2020.1766246.

[174] Ho, J. Y., See, Y. S., Leong, K. C., and Wong, T. N., "An experimental investigation of a PCM-based heat sink enhanced with a topology-optimized tree-like structure," *Energy Conversion and Management*, Vol. 245, 2021, p. 114608. https://doi.org/10.1016/j.enconman.2021.114608, URL https://www.sciencedirect.com/science/article/pii/S0196890421007846.

[175] Zhao, Y., Zhang, X., Xu, X., and Zhang, S., "Development of composite phase change cold storage material and its application in vaccine cold storage equipment," *Journal of Energy Storage*, Vol. 30, 2020, p. 101455. https://doi.org/10.1016/j.est.2020.101455, URL https://www.sciencedirect.com/science/article/pii/S2352152X20304564.

[176] Huang, L., and Piontek, U., "Improving Performance of Cold-Chain Insulated Container with Phase Change Material: An Experimental Investigation," *Applied Sciences*, Vol. 7, No. 12, 2017, p. 1288. https://doi.org/10.3390/app7121288, URL https://www.mdpi.com/2076-3417/7/12/1288, number: 12 Publisher: Multidisciplinary Digital Publishing Institute.

[177] Alehosseini, E., and Jafari, S. M., "Micro/nano-encapsulated phase change materials (PCMs) as emerging materials for the food industry," *Trends in Food Science & Technology*, Vol. 91, 2019, pp. 116–128. https://doi.org/10.1016/j.tifs.2019.07.003, URL https://www.sciencedirect.com/science/article/pii/S0924224418307179.

[178] Prakash, R., Ravindra, M. R., Pushpadass, H. A., Sivaram, M., Jeyaku-

mar, S., and Rao, K. J., "Milk chilling using nanoparticle enhanced phase change material capsuled inside a jacketed cylindrical module: A numerical and experimental study," *Innovative Food Science & Emerging Technologies*, Vol. 81, 2022, p. 103112. https://doi.org/10.1016/j.ifset.2022.103112, URL https://www.sciencedirect.com/science/article/pii/S1466856422001977.

[179] Ma, K., Zhang, X., Ji, J., Han, L., Ding, X., and Xie, W., "Application and research progress of phase change materials in biomedical field," *Biomaterials Science*, Vol. 9, No. 17, 2021, pp. 5762–5780. https://doi.org/10.1039/D1BM00719J, URL https://pubs.rsc.org/en/content/articlelanding/2021/bm/d1bm00719j, publisher: The Royal Society of Chemistry.

[180] Salaün, F., Devaux, E., Bourbigot, S., and Rumeau, P., "Development of Phase Change Materials in Clothing Part I: Formulation of Microencapsulated Phase Change," *Textile Research Journal*, Vol. 80, No. 3, 2010, pp. 195–205. https://doi.org/10.1177/0040517509093436, URL https://doi.org/10.1177/0040517509093436, publisher: SAGE Publications Ltd STM.

[181] Iqbal, K., Khan, A., Sun, D., Ashraf, M., Rehman, A., Safdar, F., Basit, A., and Maqsood, H. S., "Phase change materials, their synthesis and application in textiles—a review," *The Journal of The Textile Institute*, Vol. 110, No. 4, 2019, pp. 625–638. https://doi.org/10.1080/00405000.2018.1548088, URL https://doi.org/10.1080/00405000.2018.1548088, publisher: Taylor & Francis _eprint: https://doi.org/10.1080/00405000.2018.1548088.

[182] De Boer, R., Smeding, S. F., Bach, P. W., and De Joode, G., "Heat storage systems for use in an industrial batch process. (Results of) a case study," 2006. URL https://www.osti.gov/etdeweb/biblio/20838416.

[183] Arie, M. A., Shooshtari, A. H., Tiwari, R., Dessiatoun, S. V., Ohadi, M. M.,

and Pearce, J. M., "Experimental characterization of heat transfer in an additively manufactured polymer heat exchanger," *Applied Thermal Engineering*, Vol. 113, 2017, pp. 575–584. https://doi.org/10.1016/j.applthermaleng.2016.11.030, URL https://www.sciencedirect.com/science/article/pii/S1359431116330630.

[184] Ma, Q., Luo, L., Wang, R. Z., and Sauce, G., "A review on transportation of heat energy over long distance: Exploratory development," *Renewable and Sustainable Energy Reviews*, Vol. 13, No. 6, 2009, pp. 1532–1540. https://doi.org/10.1016/j.rser.2008.10.004, URL https://www.sciencedirect.com/science/article/pii/S136403210800169X.

[185] Jankowski, N. R., and McCluskey, F. P., "A review of phase change materials for vehicle component thermal buffering," *Applied Energy*, Vol. 113, 2014, pp. 1525–1561. https://doi.org/10.1016/j.apenergy.2013.08.026, URL https://www.sciencedirect.com/science/article/pii/S0306261913006612.

[186] Kim, K.-b., Choi, K.-w., Kim, Y.-j., Lee, K.-h., and Lee, K.-s., "Feasibility study on a novel cooling technique using a phase change material in an automotive engine," *Energy*, Vol. 35, No. 1, 2010, pp. 478–484. https://doi.org/10.1016/j.energy.2009.10.015, URL https://www.sciencedirect.com/science/article/pii/S0360544209004484.

[187] LaClair, T. J., Gao, Z., Abdelaziz, O., Wang, M., Wolfe, E., and Craig, T., "Thermal Storage System for Electric Vehicle Cabin Heating - Component and System Analysis," SAE Technical Paper 2016-01-0244, SAE International, Warrendale, PA, Apr. 2016. https://doi.org/10.4271/2016-01-0244, URL https://www.sae.org/publications/technical-papers/content/2016-01-0244/, iSSN: 0148-7191, 2688-3627.

[188] Du, K., Calautit, J., Wang, Z., Wu, Y., and Liu, H., "A review of the applications of phase change materials in cooling, heating and power generation in different temperature ranges," *Applied Energy*, Vol. 220, 2018, pp. 242–273. https://doi.org/10.1016/j.apenergy.2018.03.005, URL https://www.sciencedirect.com/science/article/pii/S0306261918303349.

[189] Liu, M., Saman, W., and Bruno, F., "Review on storage materials and thermal performance enhancement techniques for high temperature phase change thermal storage systems," *Renewable and Sustainable Energy Reviews*, Vol. 16, No. 4, 2012, pp. 2118–2132. https://doi.org/10.1016/j.rser.2012.01.020, URL https://www.sciencedirect.com/science/article/pii/S1364032112000214.

[190] Chauhan, V. K., Shukla, S. K., and Rathore, P. K. S., "A systematic review for performance augmentation of solar still with heat storage materials: A state of art," *Journal of Energy Storage*, Vol. 47, 2022, p. 103578. https://doi.org/10.1016/j.est.2021.103578, URL https://www.sciencedirect.com/science/article/pii/S2352152X21012573.

[191] Ma, C., Zhang, Y., Chen, X., Song, X., and Tang, K., "Experimental Study of an Enhanced Phase Change Material of Paraffin/Expanded Graphite/Nano-Metal Particles for a Personal Cooling System," *Materials*, Vol. 13, No. 4, 2020, p. 980. https://doi.org/10.3390/ma13040980, URL https://www.mdpi.com/1996-1944/13/4/980.

[192] Frusteri, F., Leonardi, V., Vasta, S., and Restuccia, G., "Thermal conductivity measurement of a PCM based storage system containing carbon fibers," *Applied Thermal Engineering*, Vol. 25, No. 11, 2005, pp. 1623–1633. https://doi.org/10.1016/j.applthermaleng.2004.10.007, URL https://www.sciencedirect.com/science/article/pii/S1359431104002984.

[193] Wang, J., Li, Y., Zheng, D., Mikulčić, H., Vujanović, M., and Sundén, B., "Preparation and thermophysical property analysis of nanocomposite phase change materials for energy storage," *Renewable and Sustainable Energy Reviews*, Vol. 151, 2021, p. 111541. https://doi.org/10.1016/j.rser.2021.111541, URL https://www.sciencedirect.com/science/article/pii/S1364032121008194.

[194] Khademi, A., Shank, K., Mehrjardi, S. A. A., Tiari, S., Sorrentino, G., Said, Z., Chamkha, A. J., and Ushak, S., "A brief review on different hybrid methods of enhancement within latent heat storage systems," *Journal of Energy Storage*, Vol. 54, 2022, p. 105362. https://doi.org/10.1016/j.est.2022.105362, URL https://linkinghub.elsevier.com/retrieve/pii/S2352152X22013561.

[195] Aramesh, M., and Shabani, B., "Metal foams application to enhance the thermal performance of phase change materials: A review of experimental studies to understand the mechanisms," *Journal of Energy Storage*, Vol. 50, 2022, p. 104650. https://doi.org/10.1016/j.est.2022.104650, URL https://www.sciencedirect.com/science/article/pii/S2352152X22006648.

[196] Barako, M. T., Lingamneni, S., Katz, J. S., Liu, T., Goodson, K. E., and Tice, J., "Optimizing the design of composite phase change materials for high thermal power density," *Journal of Applied Physics*, Vol. 124, No. 14, 2018, p. 145103. https://doi.org/10.1063/1.5031914, URL http://aip.scitation.org/doi/10.1063/1.5031914.

[197] Yazawa, K., Shamberger, P. J., and Fisher, T. S., "Ragone Relations for Thermal Energy Storage Technologies," *Frontiers in Mechanical Engineering*, Vol. 5, 2019, p. 29. https://doi.org/10.3389/fmech.2019.00029, URL https://www.frontiersin.org/article/10.3389/fmech.2019.00029/full.

[198] Woods, J., Mahvi, A., Goyal, A., Kozubal, E., Odukomaiya, A., and Jack-

son, R., "Rate capability and Ragone plots for phase change thermal energy storage," *Nature Energy*, Vol. 6, No. 3, 2021, pp. 295–302. https://doi.org/10.1038/s41560-021-00778-w, URL http://www.nature.com/articles/s41560-021-00778-w.

[199] Boetcher, S. K. S., "Cool Thermal Energy Storage: Water and Ice to Alternative Phase Change Materials," *Solid-Liquid Thermal Energy Storage*, CRC Press, 2022. Num Pages: 14.

[200] Freeman, T. B., Spitzer, D., Currier, P. N., Rollin, V., and Boetcher, S. K., "Phase-Change Materials/HDPE Composite Filament: A First Step Toward Use With 3D Printing for Thermal Management Applications," *Journal of Thermal Science and Engineering Applications*, Vol. 11, No. 5, 2019. https://doi.org/10.1115/1.4042592, URL https://doi.org/10.1115/1.4042592.

[201] Freeman, T. B., Messenger, M. A., Troxler, C. J., Nawaz, K., Rodriguez, R. M., and Boetcher, S. K., "Fused filament fabrication of novel phase-change material functional composites," *Additive Manufacturing*, Vol. 39, 2021, p. 101839. https://doi.org/10.1016/j.addma.2021.101839, URL https://linkinghub.elsevier.com/retrieve/pii/S221486042100004X.

[202] Nawaz, K., Freeman, T. B., Rodriguez, R. M., and Boetcher, S. K. S., "Moisture affinity of HDPE/phase-change material composites for thermal energy storage applications," *RSC Advances*, Vol. 11, No. 49, 2021, pp. 30569–30573. https://doi.org/10.1039/D1RA03618A, URL https://pubs.rsc.org/en/content/articlelanding/2021/ra/d1ra03618a, publisher: The Royal Society of Chemistry.

[203] Freeman, T. B., Nabutola, K., Spitzer, D., Currier, P. N., and Boetcher, S. K. S., "3D-Printed PCM/HDPE Composites for Battery Thermal Man-

agement," *Volume 8B: Heat Transfer and Thermal Engineering*, American Society of Mechanical Engineers, Pittsburgh, Pennsylvania, USA, 2018, p. V08BT10A041. https://doi.org/10.1115/IMECE2018-86081, URL https://asmedigitalcollection.asme.org/IMECE/proceedings/IMECE2018/52125/Pittsburgh,%20Pennsylvania,%20USA/275475.

[204] Singh, P., Odukomaiya, A., Smith, M. K., Aday, A., Cui, S., and Mahvi, A., "Processing of phase change materials by fused deposition modeling: Toward efficient thermal energy storage designs," *Journal of Energy Storage*, Vol. 55, 2022, p. 105581. https://doi.org/10.1016/j.est.2022.105581, URL https://linkinghub.elsevier.com/retrieve/pii/S2352152X22015699.

[205] Freeman, T. B., Nawaz, K., Rodriguez, R. M., Boetcher, S. K. S., and Manglik, R. M., "Additively Manufactured Polymer- Encapsulated Phase-Change Material Heat Exchangers for Residential Thermal Energy Storage," *2021 ASHRAE Annual Conference*, 2021, pp. 400–408.

[206] Moon, H., Miljkovic, N., and King, W. P., "High power density thermal energy storage using additively manufactured heat exchangers and phase change material," *International Journal of Heat and Mass Transfer*, Vol. 153, 2020, p. 119591. https://doi.org/10.1016/j.ijheatmasstransfer.2020.119591, URL https://www.sciencedirect.com/science/article/pii/S0017931019359526.

[207] Ma, J., Ma, T., Cheng, J., and Zhang, J., "Polymer Encapsulation Strategy toward 3D Printable, Sustainable, and Reliable Form-Stable Phase Change Materials for Advanced Thermal Energy Storage," *ACS Applied Materials & Interfaces*, Vol. 14, No. 3, 2022, pp. 4251–4264. https://doi.org/10.1021/acsami.1c23972, URL https://pubs.acs.org/doi/10.1021/acsami.1c23972.

[208] Nofal, M., Pan, Y., and Al-Hallaj, S., "Selective Laser Sintering of Phase

Change Materials for Thermal Energy Storage Applications," *Procedia Manufacturing*, Vol. 10, 2017, pp. 851–865. https://doi.org/10.1016/j.promfg.2017.07.071, URL https://linkinghub.elsevier.com/retrieve/pii/S2351978917302536.

[209] Nofal, M., Al-Hallaj, S., and Pan, Y., "Experimental investigation of phase change materials fabricated using selective laser sintering additive manufacturing," *Journal of Manufacturing Processes*, Vol. 44, 2019, pp. 91–101. https://doi.org/10.1016/j.jmapro.2019.05.043, URL https://www.sciencedirect.com/science/article/pii/S1526612518302196.

[210] Nofal, M., Al-Hallaj, S., and Pan, Y., "Thermal management of lithium-ion battery cells using 3D printed phase change composites," *Applied Thermal Engineering*, Vol. 171, 2020, p. 115126. https://doi.org/10.1016/j.applthermaleng.2020.115126, URL https://www.sciencedirect.com/science/article/pii/S1359431119323956.

[211] Wei, P., Cipriani, C. E., and Pentzer, E. B., "Thermal energy regulation with 3D printed polymer-phase change material composites," *Matter*, Vol. 4, No. 6, 2021, pp. 1975–1989. https://doi.org/10.1016/j.matt.2021.03.019, URL https://www.sciencedirect.com/science/article/pii/S2590238521001260.

[212] Hatakenaka, R., Sugita, H., Kinjo, T., Saitoh, M., and Yamamoto, T., "Heat-transfer Characteristics of a Light-weight, Fin- integrated PCM Unit manufactured by Additive Manufacturing," 2017, p. 11.

[213] Wild, D., Schrezenmeier, J., Czupalla, M., and Förstner, M., "Thermal Characterization of additive manufactured Integral Structures for Phase Change Applications," 2020. URL https://ttu-ir.tdl.org/handle/2346/86394.

[214] Zhang, Y., Ma, G., Wang, J., Liu, S., and Kang, S., "Numerical and experimental study of phase-change temperature controller containing graded

cellular material fabricated by additive manufacturing," *Applied Thermal Engineering*, Vol. 150, 2019, pp. 1297–1305. https://doi.org/10.1016/j.applthermaleng.2019.01.066, URL https://linkinghub.elsevier.com/retrieve/pii/S135943111835141X.

[215] Cao, M., Huang, J., and Liu, Z., "The Enhanced Performance of Phase-Change Materials via 3D Printing with Prickly Aluminum Honeycomb for Thermal Management of Ternary Lithium Batteries," *Advances in Materials Science and Engineering*, Vol. 2020, 2020, pp. 1–11. https://doi.org/10.1155/2020/8167386, URL https://www.hindawi.com/journals/amse/2020/8167386/.

[216] Hirano, S., and Kawanami, T., "Thermal Characteristics and Development of a Phase Change Material for Thermal Energy Storage Media as Thermo-Functional Fluids," *Tetsu-to-Hagane*, Vol. 106, No. 8, 2020, pp. 581–590. https://doi.org/10.2355/tetsutohagane.TETSU-2019-127, URL https://www.jstage.jst.go.jp/article/tetsutohagane/106/8/106_TETSU-2019-127/_article/-char/ja/.

[217] Qureshi, Z. A., Al-Omari, S. A. B., Elnajjar, E., Al-Ketan, O., and Abu Al-Rub, R., "Nature-inspired triply periodic minimal surface-based structures in sheet and solid configurations for performance enhancement of a low-thermal-conductivity phase-change material for latent-heat thermal-energy-storage applications," *International Journal of Thermal Sciences*, Vol. 173, 2022, p. 107361. https://doi.org/10.1016/j.ijthermalsci.2021.107361, URL https://linkinghub.elsevier.com/retrieve/pii/S1290072921005184.

[218] Dong, Y., Wang, F., Zhang, Y., Shi, X., Zhang, A., and Shuai, Y., "Experimental and numerical study on flow characteristic and thermal performance of macro-capsules phase change material with biomimetic oval structure," *En-*

ergy, Vol. 238, 2022, p. 121830. https://doi.org/10.1016/j.energy.2021.121830, URL https://linkinghub.elsevier.com/retrieve/pii/S0360544221020788.

[219] Zhou, H., Zhang, X., Zeng, H., Yang, H., Lei, H., Li, X., and Wang, Y., "Lightweight structure of a phase-change thermal controller based on lattice cells manufactured by SLM," *Chinese Journal of Aeronautics*, Vol. 32, No. 7, 2019, pp. 1727–1732. https://doi.org/10.1016/j.cja.2018.08.017, URL https://linkinghub.elsevier.com/retrieve/pii/S1000936118302851.

[220] Tamraparni, A., Hoe, A., Deckard, M., Zhang, C., Elwany, A., Shamberger, P. J., and Felts, J. R., "Experimental Validation of Composite Phase Change Material Optimized for Thermal Energy Storage," *2021 20th IEEE Intersociety Conference on Thermal and Thermomechanical Phenomena in Electronic Systems (iTherm)*, IEEE, San Diego, CA, USA, 2021, pp. 551–555. https://doi.org/10.1109/ITherm51669.2021.9503204, URL https://ieeexplore.ieee.org/document/9503204/.

[221] Tamraparni, A., Hoe, A., Deckard, M., Zhang, C., Malone, N., Elwany, A., Shamberger, P. J., and Felts, J., "Design and Optimization of Composite Phase Change Material for Cylindrical Thermal Energy Storage," *SSRN Electronic Journal*, 2022. https://doi.org/10.2139/ssrn.4172028, URL https://www.ssrn.com/abstract=4172028.

[222] Guo, Y., Yang, H., Fu, W., Bai, L., and Miao, J., "Temperature control of star sensor baffle using 3D printing and PCM thermal energy storage technology," *International Journal of Heat and Mass Transfer*, Vol. 165, 2021, p. 120644. https://doi.org/10.1016/j.ijheatmasstransfer.2020.120644, URL https://linkinghub.elsevier.com/retrieve/pii/S0017931020335808.

[223] Yang, Z., Jia, S., Niu, Y., Lv, X., Fu, H., Zhang, Y., Liu, D., Wang, B., and

Li, Q., "Bean-Pod-Inspired 3D-Printed Phase Change Microlattices for Solar-Thermal Energy Harvesting and Storage," *Small*, Vol. 17, No. 30, 2021, p. 2101093. https://doi.org/10.1002/smll.202101093, URL https://onlinelibrary.wiley.com/doi/10.1002/smll.202101093.

[224] Wang, C., and Liu, C., "Additive Manufacturing of Shape-Stabilized Composite Phase Change Materials Via Ultraviolet Curing," *SSRN Electronic Journal*, 2022. https://doi.org/10.2139/ssrn.4173655, URL https://www.ssrn.com/abstract=4173655.

[225] Yang, Z., Ma, Y., Jia, S., Zhang, C., Li, P., Zhang, Y., and Li, Q., "3D-Printed Flexible Phase-Change Nonwoven Fabrics toward Multifunctional Clothing," *ACS Applied Materials & Interfaces*, Vol. 14, No. 5, 2022, pp. 7283–7291. https://doi.org/10.1021/acsami.1c21778, URL https://pubs.acs.org/doi/10.1021/acsami.1c21778.

[226] Yang, W., Zhou, F., Chen, X., and Zhang, Y., "Performance analysis of axial air cooling system with shark-skin bionic structure containing phase change material," *Energy Conversion and Management*, Vol. 250, 2021, p. 114921. https://doi.org/10.1016/j.enconman.2021.114921, URL https://linkinghub.elsevier.com/retrieve/pii/S0196890421010979.

[227] Yazdani, M. R., Laitinen, A., Helaakoski, V., Farnas, L. K., Kukko, K., Saari, K., and Vuorinen, V., "Efficient storage and recovery of waste heat by phase change material embedded within additively manufactured grid heat exchangers," *International Journal of Heat and Mass Transfer*, Vol. 181, 2021, p. 121846. https://doi.org/10.1016/j.ijheatmasstransfer.2021.121846, URL https://www.sciencedirect.com/science/article/pii/S0017931021009510.

[228] Vargas, A., Huitink, D., Iradukunda, A.-C., and Eddy, C., "Topology Opti-

mized Phase Change Material Integrated Heat sinks and Validation," *2020 19th IEEE Intersociety Conference on Thermal and Thermomechanical Phenomena in Electronic Systems (ITherm)*, IEEE, Orlando, FL, USA, 2020, pp. 703–707. https://doi.org/10.1109/ITherm45881.2020.9190539, URL https://ieeexplore.ieee.org/document/9190539/.

[229] Iradukunda, A.-C., "Transient thermal performance using phase change material integrated topology optimized heat sinks," *Applied Thermal Engineering*, 2020, p. 8. https://doi.org/https://doi.org/10.1016/j.applthermaleng.2020.115723.

[230] Gasca-Tirado, J., Manzano-Ramírez, A., Velázquez-Castillo, R. R., Gómez-Luna, B., Nava-Mendoza, R., López-Romero, J., Apátiga-Castro, L. M., and Rivera-Muñoz, E. M., "Porous geopolymer as a possible template for a phase change material," *Materials Chemistry and Physics*, Vol. 236, 2019, p. 121785. https://doi.org/10.1016/j.matchemphys.2019.121785, URL https://linkinghub.elsevier.com/retrieve/pii/S0254058419305759.

[231] Gogoi, P., Li, Z., Guo, Z., Khuje, S., An, L., Hu, Y., Chang, S., Zhou, C., and Ren, S., "Ductile cooling phase change material," *Nanoscale Advances*, Vol. 2, No. 9, 2020, pp. 3900–3905. https://doi.org/10.1039/D0NA00465K, URL https://pubs.rsc.org/en/content/articlelanding/2020/na/d0na00465k, publisher: RSC.

[232] Righetti, G., Doretti, L., Zilio, C., Longo, G. A., and Mancin, S., "Experimental investigation of phase change of medium/high temperature paraffin wax embedded in 3D periodic structure," *International Journal of Thermofluids*, Vol. 5-6, 2020, p. 100035. https://doi.org/10.1016/j.ijft.2020.100035, URL https://linkinghub.elsevier.com/retrieve/pii/S2666202720300227.

[233] Salgado-Pizarro, R., Padilla, J. A., Xuriguera, E., Barreneche, C., and Fernández, A. I., "Novel Shape-Stabilized Phase Change Material with Cascade Character: Synthesis, Performance and Shaping Evaluation," *Energies*, Vol. 14, No. 9, 2021, p. 2621. https://doi.org/10.3390/en14092621, URL https://www.mdpi.com/1996-1073/14/9/2621.

[234] Ayat, S., Daguse, B., and Khazaka, R., "Design Considerations of Windings formed with Hollow Conductors Cooled with Phase Change Material," *2019 IEEE Energy Conversion Congress and Exposition (ECCE)*, IEEE, Baltimore, MD, USA, 2019, pp. 5652–5658. https://doi.org/10.1109/ECCE.2019.8912762, URL https://ieeexplore.ieee.org/document/8912762/.

[235] ElIdi, M., Karkri, M., AbdouTankari, M., and Vincent, S., "Hybrid cooling based battery thermal management using composite phase change materials and forced convection," *Journal of Energy Storage*, Vol. 41, 2021, p. 102946. https://doi.org/10.1016/j.est.2021.102946, URL https://linkinghub.elsevier.com/retrieve/pii/S2352152X21006629.

[236] Righetti, G., Zilio, C., Doretti, L., Longo, G. A., and Mancin, S., "On the design of Phase Change Materials based thermal management systems for electronics cooling," *Applied Thermal Engineering*, Vol. 196, 2021, p. 117276. https://doi.org/10.1016/j.applthermaleng.2021.117276, URL https://linkinghub.elsevier.com/retrieve/pii/S1359431121007122.

[237] Ge, R., "Additive manufacturing of a topology-optimised multi-tube energy storage device_ Experimental tests and numerical analysis," *Applied Thermal Engineering*, 2020, p. 12. https://doi.org/https://doi.org/10.1016/j.applthermaleng.2020.115878.

[238] Qureshi, Z. A., Al Omari, S. A. B., Elnajjar, E., Mahmoud, F., Al-Ketan, O.,

and Al-Rub, R. A., "Thermal characterization of 3D-Printed lattices based on triply periodic minimal surfaces embedded with organic phase change material," *Case Studies in Thermal Engineering*, Vol. 27, 2021, p. 101315. https://doi.org/10.1016/j.csite.2021.101315, URL https://www.sciencedirect.com/science/article/pii/S2214157X21004780.

[239] Almonti, D., Mingione, E., Tagliaferri, V., and Ucciardello, N., "Design and analysis of compound structures integrated with bio-based phase change materials and lattices obtained through additive manufacturing," *The International Journal of Advanced Manufacturing Technology*, Vol. 119, No. 1-2, 2022, pp. 149–161. https://doi.org/10.1007/s00170-021-08110-2, URL https://link.springer.com/10.1007/s00170-021-08110-2.

[240] Dudon, J. P., Bosse, J., Atinsounon, P., Raynaud, M., Valentini, D., Ferrier, M., and Blanc, G., "Optimized Phase Change Material Module for Thermal Regulation of Cycled Dissipative Units," *49th International Conference on Environmental Systems*, 2019, p. 17.

[241] Kumar, N., and Banerjee, D., "Experimental Validation of Numerical Predictions for the Transient Performance of a Simple Latent Heat Storage Unit (LHSU) Utilizing Phase Change Material (PCM) and 3-D Printing," *Volume 1: Aerospace Heat Transfer; Computational Heat Transfer; Education; Environmental Heat Transfer; Fire and Combustion Systems; Gas Turbine Heat Transfer; Heat Transfer in Electronic Equipment; Heat Transfer in Energy Systems*, American Society of Mechanical Engineers, Bellevue, Washington, USA, 2017, p. V001T09A017. https://doi.org/10.1115/HT2017-5045, URL https://asmedigitalcollection.asme.org/HT/proceedings/HT2017/57885/Bellevue,%20Washington,%20USA/289358.

[242] Kabir, M., Gemeda, T., Preller, E., and Xu, J., "Design and Development

of a PCM-Based Two-Phase Heat Exchanger Manufactured Additively for Spacecraft Thermal Management Systems," *International Journal of Heat and Mass Transfer*, Vol. 180, 2021, p. 121782. https://doi.org/10.1016/j.ijheatmasstransfer.2021.121782, URL https://www.sciencedirect.com/science/article/pii/S0017931021008875.

[243] Hu, X., and Gong, X., "Experimental study on the thermal response of PCM-based heat sink using structured porous material fabricated by 3D printing," *Case Studies in Thermal Engineering*, Vol. 24, 2021, p. 100844. https://doi.org/10.1016/j.csite.2021.100844, URL https://linkinghub.elsevier.com/retrieve/pii/S2214157X21000071.

[244] Ge, R., Li, Q., Li, C., and Liu, Q., "Evaluation of different melting performance enhancement structures in a shell-and-tube latent heat thermal energy storage system," *Renewable Energy*, Vol. 187, 2022, pp. 829–843. https://doi.org/10.1016/j.renene.2022.01.097, URL https://linkinghub.elsevier.com/retrieve/pii/S0960148122001082.

[245] Hu, X., and Gong, X., "Experimental and numerical investigation on thermal performance enhancement of phase change material embedding porous metal structure with cubic cell," *Applied Thermal Engineering*, Vol. 175, 2020, p. 115337. https://doi.org/10.1016/j.applthermaleng.2020.115337, URL https://linkinghub.elsevier.com/retrieve/pii/S1359431119384388.

[246] Diani, A., Moro, L., and Rossetto, L., "Melting of Paraffin Waxes Embedded in a Porous Matrix Made by Additive Manufacturing," *Applied Sciences*, Vol. 11, No. 12, 2021, p. 5396. https://doi.org/10.3390/app11125396, URL https://www.mdpi.com/2076-3417/11/12/5396.

[247] Righetti, G., "Experimental study of phase change material (PCM) embedded

in 3D periodic structures realized via additive manufacturing," *International Journal of Thermal Sciences*, 2020, p. 12. https://doi.org/https://doi.org/10.1016/j.ijthermalsci.2020.106376.

[248] Sharma, S., Micheli, L., Chang, W., Tahir, A., Reddy, K., and Mallick, T., "Nano-enhanced Phase Change Material for thermal management of BICPV," *Applied Energy*, Vol. 208, 2017, pp. 719–733. https://doi.org/10.1016/j.apenergy.2017.09.076, URL https://linkinghub.elsevier.com/retrieve/pii/S0306261917313582.

[249] Rigotti, D., Dorigato, A., and Pegoretti, A., "3D printable thermoplastic polyurethane blends with thermal energy storage/release capabilities," *Materials Today Communications*, Vol. 15, 2018, pp. 228–235. https://doi.org/10.1016/j.mtcomm.2018.03.009, URL https://linkinghub.elsevier.com/retrieve/pii/S2352492818300606.

[250] Sharar, D. J., Wilson, A. A., Leff, A., Smith, A., Atli, K. C., Elwany, A., Arroyave, R., and Karaman, I., "Additively Manufacturing Nitinol as a Solid-State Phase Change Material," *2020 19th IEEE Intersociety Conference on Thermal and Thermomechanical Phenomena in Electronic Systems (ITherm)*, IEEE, Orlando, FL, USA, 2020, pp. 821–826. https://doi.org/10.1109/ITherm45881.2020.9190336, URL https://ieeexplore.ieee.org/document/9190336/.

[251] Confalonieri, C., and Gariboldi, E., "Al-Sn Miscibility Gap Alloy produced by Power Bed Laser Melting for application as Phase Change Material," *Journal of Alloys and Compounds*, Vol. 881, 2021, p. 160596. https://doi.org/10.1016/j.jallcom.2021.160596, URL https://linkinghub.elsevier.com/retrieve/pii/S0925838821020053.

[252] Ma, J., Ma, T., Cheng, J., and Zhang, J., "3D Printable, Recyclable and Adjustable Comb/Bottlebrush Phase Change Polysiloxane Networks toward Sustainable Thermal Energy Storage," *Energy Storage Materials*, Vol. 39, 2021, p. 11. https://doi.org/doi.org/10.1016/j.ensm.2021.04.033.

[253] Wilts, E. M., "Structure-Property-Processing Relationships Between Polymeric Solutions and Additive Manufacturing for Biomedical Applications," Ph.D. thesis, Virginia Polytechnic Institute, Blacksburg, VA, Sep. 2020.

[254] Mao, Y., Miyazaki, T., Sakai, K., Gong, J., Zhu, M., and Ito, H., "A 3D Printable Thermal Energy Storage Crystalline Gel Using Mask-Projection Stereolithography," *Polymers*, Vol. 10, No. 10, 2018, p. 1117. https://doi.org/10.3390/polym10101117, URL https://www.ncbi.nlm.nih.gov/pmc/articles/PMC6404010/.

[255] Kiziroglou, M. E., Becker, T., Wright, S. W., Yeatman, E. M., Evans, J. W., and Wright, P. K., "Three-Dimensional Printed Insulation For Dynamic Thermoelectric Harvesters With Encapsulated Phase Change Materials," *IEEE Sensors Letters*, Vol. 1, No. 4, 2017, pp. 1–4. https://doi.org/10.1109/LSENS.2017.2720960, URL http://ieeexplore.ieee.org/document/7961248/.

[256] Saadi, M. A. S. R., Maguire, A., Pottackal, N. T., Thakur, M. S. H., Ikram, M. M., Hart, A. J., Ajayan, P. M., and Rahman, M. M., "Direct Ink Writing: A 3D Printing Technology for Diverse Materials," *Advanced Materials*, Vol. 34, No. 28, 2022, p. 2108855. https://doi.org/10.1002/adma.202108855, URL https://onlinelibrary.wiley.com/doi/10.1002/adma.202108855.

[257] Hao, L., Xiao, J., Sun, J., Xia, B., and Cao, W., "Thermal conductivity of 3D printed concrete with recycled fine aggregate composite phase change materials," *Journal of Cleaner Production*, Vol. 364, 2022, p. 132598. https:

//doi.org/10.1016/j.jclepro.2022.132598, URL https://linkinghub.elsevier.com/retrieve/pii/S0959652622021977.

[258] Cui, H., Yu, S., Cao, X., and Yang, H., "Evaluation of Printability and Thermal Properties of 3D Printed Concrete Mixed with Phase Change Materials," *Energies*, Vol. 15, No. 6, 2022, p. 1978. https://doi.org/10.3390/en15061978, URL https://www.mdpi.com/1996-1073/15/6/1978.

[259] Wu, Z., Xu, Y., and Šavija, B., "Mechanical Properties of Lightweight Cementitious Cellular Composites Incorporating Micro-Encapsulated Phase Change Material," 2021, p. 24.

[260] Wei, C., and Dong, J., "Development and Modeling of Melt Electrohydrodynamic-Jet Printing of Phase-Change Inks for High-Resolution Additive Manufacturing," *Journal of Manufacturing Science and Engineering*, Vol. 136, No. 6, 2014, p. 061010. https://doi.org/10.1115/1.4028483, URL https://asmedigitalcollection.asme.org/manufacturingscience/article/doi/10.1115/1.4028483/377619/Development-and-Modeling-of-Melt.

[261] Han, Y., Wei, C., and Dong, J., "Droplet formation and settlement of phase-change ink in high resolution electrohydrodynamic (EHD) 3D printing," *Journal of Manufacturing Processes*, Vol. 20, 2015, pp. 485–491. https://doi.org/10.1016/j.jmapro.2015.06.019, URL https://www.sciencedirect.com/science/article/pii/S152661251500064X.

[262] Hubert, R., Bou Matar, O., Foncin, J., Coquet, P., Tan, D., Li, H., Teo, E. H. T., Merlet, T., and Pernod, P., "An effective thermal conductivity model for architected phase change material enhancer: Theoretical and experimental investigations," *International Journal of Heat and Mass Transfer*, Vol. 176,

2021, p. 121364. https://doi.org/10.1016/j.ijheatmasstransfer.2021.121364, URL https://linkinghub.elsevier.com/retrieve/pii/S0017931021004671.

[263] Diani, A., Nonino, C., and Rossetto, L., "Melting of phase change materials inside periodic cellular structures fabricated by additive manufacturing: Experimental results and numerical simulations," *Applied Thermal Engineering*, Vol. 215, 2022, p. 118969. https://doi.org/10.1016/j.applthermaleng.2022.118969, URL https://linkinghub.elsevier.com/retrieve/pii/S1359431122009073.

[264] Han, Z., and Fina, A., "Thermal conductivity of carbon nanotubes and their polymer nanocomposites: A review," *Progress in Polymer Science*, Vol. 36, No. 7, 2011, pp. 914–944. https://doi.org/10.1016/j.progpolymsci.2010.11.004, URL https://www.sciencedirect.com/science/article/pii/S0079670010001243.

[265] Shemelya, C., De La Rosa, A., Torrado, A. R., Yu, K., Domanowski, J., Bonacuse, P. J., Martin, R. E., Juhasz, M., Hurwitz, F., Wicker, R. B., Conner, B., MacDonald, E., and Roberson, D. A., "Anisotropy of thermal conductivity in 3D printed polymer matrix composites for space based cube satellites," *Additive Manufacturing*, Vol. 16, 2017, pp. 186–196. https://doi.org/10.1016/j.addma.2017.05.012, URL https://www.sciencedirect.com/science/article/pii/S2214860417302324.

[266] Chen, J., Liu, X., Tian, Y., Zhu, W., Yan, C., Shi, Y., Kong, L. B., Qi, H. J., and Zhou, K., "3D-Printed Anisotropic Polymer Materials for Functional Applications," *Advanced Materials*, Vol. 34, No. 5, 2022, p. 2102877. https://doi.org/10.1002/adma.202102877, URL https://onlinelibrary.wiley.com/doi/abs/10.1002/adma.202102877, _eprint: https://onlinelibrary.wiley.com/doi/pdf/10.1002/adma.202102877.

[267] Ibrahim, Y., Elkholy, A., Schofield, J. S., Melenka, G. W., and Kempers, R., "Effective thermal conductivity of 3D-printed continuous fiber polymer composites," *Advanced Manufacturing: Polymer & Composites Science*, Vol. 6, No. 1, 2020, pp. 17–28. https://doi.org/10.1080/20550340.2019.1710023, URL https://doi.org/10.1080/20550340.2019.1710023, publisher: Taylor & Francis _eprint: https://doi.org/10.1080/20550340.2019.1710023.

[268] Jäger, A., Johannesmann, S., Claes, L., Webersen, M., Henning, B., and Kupnik, M., "Evaluating the influence of 3D-printing parameters on acoustic material properties," *2017 IEEE International Ultrasonics Symposium (IUS)*, 2017, pp. 1–4. https://doi.org/10.1109/ULTSYM.2017.8092398, iSSN: 1948-5727.

[269] Manoj Prabhakar, M., Saravanan, A. K., Haiter Lenin, A., Jerin leno, I., Mayandi, K., and Sethu Ramalingam, P., "A short review on 3D printing methods, process parameters and materials," *Materials Today: Proceedings*, Vol. 45, 2021, pp. 6108–6114. https://doi.org/10.1016/j.matpr.2020.10.225, URL https://www.sciencedirect.com/science/article/pii/S2214785320378317.

[270] Delfs, P., Tows, M., and Schmid, H. J., "Optimized build orientation of additive manufactured parts for improved surface quality and build time," *Additive Manufacturing*, Vol. 12, 2016, pp. 314–320. https://doi.org/10.1016/j.addma.2016.06.003, URL https://www.sciencedirect.com/science/article/pii/S2214860416301142.

[271] Arnold, C., Monsees, D., Hey, J., and Schweyen, R., "Surface Quality of 3D-Printed Models as a Function of Various Printing Parameters," *Materials*, Vol. 12, No. 12, 2019, p. 1970. https://doi.org/10.3390/ma12121970, URL https://www.mdpi.com/1996-1944/12/12/1970, number: 12 Publisher: Multidisciplinary Digital Publishing Institute.

[272] Wang, Z., Liu, P., Xiao, Y., Cui, X., Hu, Z., and Chen, L., "A Data-Driven Approach for Process Optimization of Metallic Additive Manufacturing Under Uncertainty," *Journal of Manufacturing Science and Engineering*, Vol. 141, No. 8, 2019. https://doi.org/10.1115/1.4043798, URL https://doi.org/10.1115/1.4043798.

[273] Almuallim, B., Harun, W. S. W., Al Rikabi, I. J., and Mohammed, H. A., "Thermally conductive polymer nanocomposites for filament-based additive manufacturing," *Journal of Materials Science*, Vol. 57, No. 6, 2022, pp. 3993–4019. https://doi.org/10.1007/s10853-021-06820-2, URL https://doi.org/10.1007/s10853-021-06820-2.

[274] Nguyen, T. K., and Lee, B.-K., "Post-processing of FDM parts to improve surface and thermal properties," *Rapid Prototyping Journal*, Vol. 24, No. 7, 2018, pp. 1091–1100. https://doi.org/10.1108/RPJ-12-2016-0207, URL https://doi.org/10.1108/RPJ-12-2016-0207, publisher: Emerald Publishing Limited.

[275] Prajapati, H., Ravoori, D., Woods, R. L., and Jain, A., "Measurement of anisotropic thermal conductivity and inter-layer thermal contact resistance in polymer fused deposition modeling (FDM)," *Additive Manufacturing*, Vol. 21, 2018, pp. 84–90. https://doi.org/10.1016/j.addma.2018.02.019, URL https://www.sciencedirect.com/science/article/pii/S2214860417305456.

[276] Ravoori, D., Alba, L., Prajapati, H., and Jain, A., "Investigation of process-structure-property relationships in polymer extrusion based additive manufacturing through in situ high speed imaging and thermal conductivity measurements," *Additive Manufacturing*, Vol. 23, 2018, pp. 132–139. https://doi.org/10.1016/j.addma.2018.07.011, URL https://www.sciencedirect.com/science/article/pii/S2214860418301210.

[277] Prajapati, H., Chalise, D., Ravoori, D., Taylor, R. M., and Jain, A., "Improvement in build-direction thermal conductivity in extrusion-based polymer additive manufacturing through thermal annealing," *Additive Manufacturing*, Vol. 26, 2019, pp. 242–249. https://doi.org/10.1016/j.addma.2019.01.004, URL https://www.sciencedirect.com/science/article/pii/S2214860418308716.

[278] Raza, G., Shi, Y., and Deng, Y., "Expanded graphite as thermal conductivity enhancer for paraffin wax being used in thermal energy storage systems," *2016 13th International Bhurban Conference on Applied Sciences and Technology (IBCAST)*, 2016, pp. 1–12. https://doi.org/10.1109/IBCAST.2016.7429846, iSSN: 2151-1411.

[279] Huang, X., Jiang, P., and Tanaka, T., "A review of dielectric polymer composites with high thermal conductivity," *IEEE Electrical Insulation Magazine*, Vol. 27, No. 4, 2011, pp. 8–16. https://doi.org/10.1109/MEI.2011.5954064, conference Name: IEEE Electrical Insulation Magazine.

[280] Wencke, Y. L., Kutlu, Y., Seefeldt, M., Esen, C., Ostendorf, A., and Luinstra, G. A., "Additive manufacturing of PA12 carbon nanotube composites with a novel laser polymer deposition process," *Journal of Applied Polymer Science*, Vol. 138, No. 19, 2021, p. 50395. https://doi.org/10.1002/app.50395, URL https://onlinelibrary.wiley.com/doi/abs/10.1002/app.50395, _eprint: https://onlinelibrary.wiley.com/doi/pdf/10.1002/app.50395.

[281] Tekinalp, H. L., Kunc, V., Velez-Garcia, G. M., Duty, C. E., Love, L. J., Naskar, A. K., Blue, C. A., and Ozcan, S., "Highly oriented carbon fiber–polymer composites via additive manufacturing," *Composites Science and Technology*, Vol. 105, 2014, pp. 144–150. https://doi.org/10.1016/j.compscitech.2014.10.009, URL https://www.sciencedirect.com/science/article/pii/S0266353814003716.

[282] Caminero, M. , Chacón, J. M., García-Plaza, E., Núñez, P. J., Reverte, J. M., and Becar, J. P., "Additive Manufacturing of PLA-Based Composites Using Fused Filament Fabrication: Effect of Graphene Nanoplatelet Reinforcement on Mechanical Properties, Dimensional Accuracy and Texture," *Polymers*, Vol. 11, No. 5, 2019, p. 799. https://doi.org/10.3390/polym11050799, URL https://www.mdpi.com/2073-4360/11/5/799, number: 5 Publisher: Multidisciplinary Digital Publishing Institute.

[283] "Carbon Black - Materials Handled - Flexicon Corporation," , ????. URL https://www.flexicon.com/Materials-Handled/Carbon-Black.html.

[284] Elements, A., "Carbon Nanotubes," , ???? URL https://www.americanelements.com/carbon-nanotubes-308068-56-6.

[285] Karaipekli, A., Sarı, A., and Kaygusuz, K., "Thermal conductivity improvement of stearic acid using expanded graphite and carbon fiber for energy storage applications," *Renewable Energy*, Vol. 32, No. 13, 2007, pp. 2201–2210. https://doi.org/10.1016/j.renene.2006.11.011, URL https://www.sciencedirect.com/science/article/pii/S0960148106003351.

[286] Kumanek, B., and Janas, D., "Thermal conductivity of carbon nanotube networks: a review," *Journal of Materials Science*, Vol. 54, No. 10, 2019, pp. 7397–7427. https://doi.org/10.1007/s10853-019-03368-0, URL https://doi.org/10.1007/s10853-019-03368-0.

[287] Colla, L., Fedele, L., Mancin, S., Danza, L., and Manca, O., "Nano-PCMs for enhanced energy storage and passive cooling applications," *Applied Thermal Engineering*, Vol. 110, 2017, pp. 584–589. https://doi.org/10.1016/j.applthermaleng.2016.03.161, URL https://www.sciencedirect.com/science/article/pii/S1359431116304707.

[288] Liao, G., Li, Z., Cheng, Y., Xu, D., Zhu, D., Jiang, S., Guo, J., Chen, X., Xu, G., and Zhu, Y., "Properties of oriented carbon fiber/polyamide 12 composite parts fabricated by fused deposition modeling," *Materials & Design*, Vol. 139, 2018, pp. 283–292. https://doi.org/10.1016/j.matdes.2017.11.027, URL https://www.sciencedirect.com/science/article/pii/S0264127517310584.

[289] Wang, F., Yang, Z., Hu, X., Pan, Y., Lu, Y., and Jiang, M., "Coaxial 3D printed anisotropic thermal conductive composite aerogel with aligned hierarchical porous carbon nanotubes and cellulose nanofibers," *Smart Materials and Structures*, Vol. 31, No. 4, 2022, p. 045002. https://doi.org/10.1088/1361-665X/ac4e4e, URL https://dx.doi.org/10.1088/1361-665X/ac4e4e, publisher: IOP Publishing.

[290] "Silicon Carbide SiC Material Properties," , ????. URL http://accuratus.com/silicar.html.

[291] "Boron Nitride | BN Material Properties," , ????. URL http://accuratus.com/boron.html.

[292] Wu, S., Yan, T., Kuai, Z., and Pan, W., "Corrigendum to: "Thermal conductivity enhancement on phase change materials for thermal energy storage: A review"," *Energy Storage Materials*, Vol. 33, 2020, p. 503. https://doi.org/10.1016/j.ensm.2020.06.019, URL https://www.sciencedirect.com/science/article/pii/S2405829720302397.

[293] Li, J., Leng, J., Jiang, Y., and Zhang, J., "Experimental characterization of 3D printed PP/h-BN thermally conductive composites with highly oriented h-BN and the effects of filler size," *Composites Part A: Applied Science and Manufacturing*, Vol. 150, 2021, p. 106586. https://doi.org/10.1016/

j.compositesa.2021.106586, URL https://www.sciencedirect.com/science/article/pii/S1359835X21003067.

[294] Sonsalla, T., Moore, A. L., Meng, W. J., Radadia, A. D., and Weiss, L., "3-D printer settings effects on the thermal conductivity of acrylonitrile butadiene styrene (ABS)," *Polymer Testing*, Vol. 70, 2018, pp. 389–395. https://doi.org/10.1016/j.polymertesting.2018.07.018, URL https://www.sciencedirect.com/science/article/pii/S0142941818305919.

[295] Elkholy, A., Rouby, M., and Kempers, R., "Characterization of the anisotropic thermal conductivity of additively manufactured components by fused filament fabrication," *Progress in Additive Manufacturing*, Vol. 4, No. 4, 2019, pp. 497–515. https://doi.org/10.1007/s40964-019-00098-2, URL https://doi.org/10.1007/s40964-019-00098-2.

[296] Wu, H., Li, Q., Bu, X., Liu, W., Cao, G., Li, X., and Wang, X., "Gas sensing performance of graphene-metal contact after thermal annealing," *Sensors and Actuators B: Chemical*, Vol. 282, 2019, pp. 408–416. https://doi.org/10.1016/j.snb.2018.11.066, URL https://www.sciencedirect.com/science/article/pii/S0925400518320215.

[297] Torrado, A. R., and Roberson, D. A., "Failure Analysis and Anisotropy Evaluation of 3D-Printed Tensile Test Specimens of Different Geometries and Print Raster Patterns," *Journal of Failure Analysis and Prevention*, Vol. 16, No. 1, 2016, pp. 154–164. https://doi.org/10.1007/s11668-016-0067-4, URL https://doi.org/10.1007/s11668-016-0067-4.

[298] Guo, Y., Yang, H., Lin, G., Jin, H., Shen, X., He, J., and Miao, J., "Thermal performance of a 3D printed lattice-structure heat sink packaging phase change material," *Chinese Journal of Aeronautics*, Vol. 34, No. 5, 2021, pp.

373–385. https://doi.org/10.1016/j.cja.2020.07.033, URL https://www.sciencedirect.com/science/article/pii/S1000936120303551.

[299] Mehling, H., Brütting, M., and Haussmann, T., "PCM products and their fields of application - An overview of the state in 2020/2021," *Journal of Energy Storage*, Vol. 51, 2022, p. 104354. https://doi.org/10.1016/j.est.2022.104354, URL https://www.sciencedirect.com/science/article/pii/S2352152X22003784.

[300] "Axiotherm PCM - products | Axiotherm GmbH - Innovative thermal storage systems," , ????. URL https://www.axiotherm.de/en/produkte/axiotherm-pcm/.

[301] "Phase Change Material | Boyd," , ????. URL https://www.boydcorp.com/thermal/conduction-cooling/phase-change-interface-materials.html.

[302] "PCM-ClimSel," , ????. URL https://www.climator.com/en/pcm-climsel.

[303] "Thermal energy storage | Energy Technologies," , ????. URL https://www.crodaenergytechnologies.com/en-gb/applications/thermal-energy-storage.

[304] "PCM Technology Applications," , ????. URL https://www.pcmtechnology.eu/en/applications/for-homes.

[305] "Parvan at ExxonMobil," , ????. URL https://www.exxonmobil.com/en/wax/wax-types/fully-refined-paraffin-wax.

[306] "Henkel Phase Change Materials," , ????. URL https://www.henkel-adhesives.com/us/en/products/thermal-management-materials/phase-change-material.html.

[307] "Honeywell Phase Change Materials," , ????. URL https:

//thermalmanagement.honeywell.com/us/en/products/thermal-interface-materials/phase-change-materials.

[308] "Insolcorp Phase Change Materials," , ????. URL https://insolcorp.com/services/.

[309] "Laird Phase Change Materials," , ????. URL https://www.laird.com/products/thermal-interface-materials/phase-change.

[310] "Microtek Phase Change Materials," , ????. URL https://www.microteklabs.com/phase-change-materials/.

[311] "Technology – BioPCM – Phase Change Solutions," , ????. URL https://phasechange.com/biopcm/.

[312] "savE® PCMs Product Range – PLUSS®," , ????. URL https://pluss.co.in/save-pcms-product-range/.

[313] PureTemp, "PureTemp," , ???? URL https://puretemp.com/?page_id=173.

[314] "Rubitherm GmbH," , ????. URL https://www.rubitherm.eu/en/productcategory/makroverkaspelung-w%C3%A4rmekissen.

[315] "Sasol Phase Change Materials," , ????. URL https://www.sasolnorthamerica.com/products/phase-change-materials-1/.

[316] "Sunamp | Global - World leading thermal storage technologies," , ????. URL https://sunamp.com/hot-water-thermino-overview/.

[317] "PCM Solutions - Tempered Entropy," , Nov. 2018. URL https://www.pcmgel.com/pcm-solutions/.

[318] "Ice Thermal Storage | Thermal Energy Storage | Baltimore Aircoil Company," , ????. URL https://baltimoreaircoil.com/products/ice-thermal-storage.

[319] "CALMAC® global leader in energy storage," , ????. URL http://www.calmac.com/.

[320] "Evapco Thermal Ice Storage," , Sep. 2016. URL http://www.evapco.com/products/product-featuresextras/thermal-ice-storage.

[321] "Sunamp | Global - World leading thermal storage technologies," , ????. URL https://sunamp.com/plentigrade/.

[322] "Products – ENRG Blanket – Phase Change Solutions," , ????. URL https://phasechange.com/enrgblanket/.

[323] "HeatSels® - products | Axiotherm GmbH - Innovative thermal storage systems," , ????. URL https://www.axiotherm.de/en/produkte/heatsels%C2%AE/.

[324] "HeatStaxx® Air - products | Axiotherm GmbH - Innovative thermal storage systems," , ????. URL https://www.axiotherm.de/en/produkte/heatstaxx%C2%AE-air/.

[325] peschel, "Collector with plastic cover," , Jun. 2016. URL https://www.sunwindenergy.com/solar-thermal/collector-plastic-cover.

[326] "PCM Heat Sinks Manufacturer | Custom Copper Heat Sink Design | Two Phase Heatsink," , ????. URL https://www.1-act.com/products/pcm-heat-sinks/.

[327] "Koolit Refrigerants," , ????. URL https://www.coldchaintech.com/koolit-refrigerants/.

[328] "Foam Bricks, Gel Packs, & Refrigerant Mats | Refrigerants | ThermoSafe," , ????. URL https://www.thermosafe.com/products/refrigerants/.

[329] "PCC Technology," , ????. URL https://www.allcelltech.com/pcc.

[330] "Cold Storage," , ????. URL https://www.vikingcold.com/cold-storage/.

[331] "Technology – PLUSS®," , ????. URL https://pluss.co.in/technology/.

[332] "Glacier Tek | Cooling Vests & Products," , ????. URL https://glaciertek.com/.

[333] "Inuteq - Keep your head cool," , ????. URL https://inuteq.com/bodycool-smart.

[334] "Outlast pcm material technology comfort climate heat management," , ????. URL https://www.outlast.com/en/.

[335] "Rubitherm GmbH," , ????. URL https://www.rubitherm.eu/en/productcategory/organische-pcm-rt.

[336] "Purchase Ice9™ Materials - TCPoly - Xpanels," , Feb. 2022. URL https://tcpoly.com/purchase-ice9-materials/.

[337] Lamé, G., and Clapeyron, B., "Mémoire sur la solidification par refroidissement d'un globe liquide," 1831, pp. 250–256. Issue: 1831.

[338] Carslaw, H. S., and Jaeger, J. C., "Conduction of heat in solids," *Conduction of heat in solids*, 1947.

[339] Stefan, J., "Über einige probleme der theorie der wärmeleitung," *Sitzungber., Wien, Akad. Mat. Natur*, Vol. 98, 1889, pp. 473–484.

[340] Stefan, J., "Ueber die Theorie der Eisbildung, insbesondere über die Eisbildung im Polarmeere," *Annalen der Physik*, Vol. 278, No. 2, 1891,

pp. 269–286. https://doi.org/10.1002/andp.18912780206, URL https://onlinelibrary.wiley.com/doi/abs/10.1002/andp.18912780206, _eprint: https://onlinelibrary.wiley.com/doi/pdf/10.1002/andp.18912780206.

[341] Bonacina, C., Comini, G., Fasano, A., and Primicerio, M., "Numerical solution of phase-change problems," *International Journal of Heat and Mass Transfer*, Vol. 16, No. 10, 1973, pp. 1825–1832. https://doi.org/10.1016/0017-9310(73)90202-0, URL https://www.sciencedirect.com/science/article/pii/0017931073902020.

[342] Meyer, G. H., "Multidimensional Stefan Problems," *SIAM Journal on Numerical Analysis*, Vol. 10, No. 3, 1973, pp. 522–538. URL https://www.jstor.org/stable/2156119, publisher: Society for Industrial and Applied Mathematics.

[343] Shamsundar, N., and Sparrow, E. M., "Storage of Thermal Energy by Solid-Liquid Phase Change—Temperature Drop and Heat Flux," *Journal of Heat Transfer*, Vol. 96, No. 4, 1974, pp. 541–544. https://doi.org/10.1115/1.3450242, URL https://doi.org/10.1115/1.3450242.

[344] Shamsundar, N., and Sparrow, E. M., "Analysis of Multidimensional Conduction Phase Change Via the Enthalpy Model," *Journal of Heat Transfer*, Vol. 97, No. 3, 1975, pp. 333–340. https://doi.org/10.1115/1.3450375, URL https://doi.org/10.1115/1.3450375.

[345] Sparrow, E. M., Patankar, S. V., and Ramadhyani, S., "Analysis of Melting in the Presence of Natural Convection in the Melt Region," *Journal of Heat Transfer*, Vol. 99, No. 4, 1977, pp. 520–526. https://doi.org/10.1115/1.3450736, URL https://doi.org/10.1115/1.3450736.

[346] Smith, R. N., Ebersole, T. E., and Griffin, F. P., "Heat Exchanger Perfor-

mance in Latent Heat Thermal Energy Storage," *Journal of Solar Energy Engineering*, Vol. 102, No. 2, 1980, pp. 112–118. https://doi.org/10.1115/1.3266128, URL https://doi.org/10.1115/1.3266128.

[347] Buddhi, D., Bansal, N. K., Sawhney, R. L., and Sodha, M. S., "Solar thermal storage systems using phase change materials," *International Journal of Energy Research*, Vol. 12, No. 3, 1988, pp. 547–555. https://doi.org/10.1002/er.4440120318, URL https://onlinelibrary.wiley.com/doi/abs/10.1002/er.4440120318, _eprint: https://onlinelibrary.wiley.com/doi/pdf/10.1002/er.4440120318.

[348] Dantzig, J. A., "Modelling liquid–solid phase changes with melt convection," *International Journal for Numerical Methods in Engineering*, Vol. 28, No. 8, 1989, pp. 1769–1785. https://doi.org/10.1002/nme.1620280805, URL https://onlinelibrary.wiley.com/doi/abs/10.1002/nme.1620280805, _eprint: https://onlinelibrary.wiley.com/doi/pdf/10.1002/nme.1620280805.

[349] Farid, M. M., and Husian, R. M., "An electrical storage heater using the phase-change method of heat storage," *Energy Conversion and Management*, Vol. 30, No. 3, 1990, pp. 219–230. https://doi.org/10.1016/0196-8904(90)90003-H, URL https://www.sciencedirect.com/science/article/pii/019689049090003H.

[350] Bellecci, C., and Conti, M., "Phase change thermal storage: transient behaviour analysis of a solar receiver/storage module using the enthalpy method," *International Journal of Heat and Mass Transfer*, Vol. 36, No. 8, 1993, pp. 2157–2163. https://doi.org/10.1016/S0017-9310(05)80146-2, URL https://www.sciencedirect.com/science/article/pii/S0017931005801462.

[351] Lacroix, M., and Duong, T., "Experimental improvements of heat transfer in

a latent heat thermal energy storage unit with embedded heat sources," *Energy Conversion and Management*, Vol. 39, No. 8, 1998, pp. 703–716. https://doi.org/10.1016/S0196-8904(97)10011-5, URL https://www.sciencedirect.com/science/article/pii/S0196890497100115.

[352] Lamberg, P., Lehtiniemi, R., and Henell, A.-M., "Numerical and experimental investigation of melting and freezing processes in phase change material storage," *International Journal of Thermal Sciences*, Vol. 43, No. 3, 2004, pp. 277–287. https://doi.org/10.1016/j.ijthermalsci.2003.07.001, URL https://www.sciencedirect.com/science/article/pii/S1290072903001303.

[353] AL-Saadi, S. N., and Zhai, Z. J., "Modeling phase change materials embedded in building enclosure: A review," *Renewable and Sustainable Energy Reviews*, Vol. 21, 2013, pp. 659–673. https://doi.org/10.1016/j.rser.2013.01.024, URL https://www.sciencedirect.com/science/article/pii/S1364032113000555.

[354] Souayfane, F., Fardoun, F., and Biwole, P. H., "Different mathematical models of convection during phase change," *2016 3rd International Conference on Renewable Energies for Developing Countries (REDEC)*, 2016, pp. 1–8. https://doi.org/10.1109/REDEC.2016.7577543.

[355] Py, X., Olives, R., and Mauran, S., "Paraffin/porous-graphite-matrix composite as a high and constant power thermal storage material," *International Journal of Heat and Mass Transfer*, Vol. 44, No. 14, 2001, pp. 2727–2737. https://doi.org/10.1016/S0017-9310(00)00309-4, URL https://www.sciencedirect.com/science/article/pii/S0017931000003094.

[356] Wu, S., Li, T. X., Yan, T., Dai, Y. J., and Wang, R. Z., "High performance form-stable expanded graphite/stearic acid composite phase change material for modular thermal energy storage," *International Journal of Heat*

and Mass Transfer, Vol. 102, 2016, pp. 733–744. https://doi.org/10.1016/j.ijheatmasstransfer.2016.06.066, URL https://www.sciencedirect.com/science/article/pii/S0017931016301909.

[357] Galazutdinova, Y., Vega, M., Grágeda, M., Cabeza, L. F., and Ushak, S., "Preparation and characterization of an inorganic magnesium chloride/nitrate/graphite composite for low temperature energy storage," *Solar Energy Materials and Solar Cells*, Vol. 175, 2018, pp. 60–70. https://doi.org/10.1016/j.solmat.2017.09.046, URL https://www.sciencedirect.com/science/article/pii/S092702481730541X.

[358] Gao, D., Chen, Z., Shi, M., and Wu, Z., "Study on the melting process of phase change materials in metal foams using lattice Boltzmann method," *Science China Technological Sciences*, Vol. 53, No. 11, 2010, pp. 3079–3087. https://doi.org/10.1007/s11431-010-4074-5, URL https://doi.org/10.1007/s11431-010-4074-5.

[359] Yang, Z., and Garimella, S. V., "Melting of Phase Change Materials With Volume Change in Metal Foams," *Journal of Heat Transfer*, Vol. 132, No. 6, 2010. https://doi.org/10.1115/1.4000747, URL https://doi.org/10.1115/1.4000747.

[360] Dukhan, N., and Bodke, S., "An improved PCM heat storage technology utilizing metal foam," *2010 12th IEEE Intersociety Conference on Thermal and Thermomechanical Phenomena in Electronic Systems*, 2010, pp. 1–7. https://doi.org/10.1109/ITHERM.2010.5501364, iSSN: 1087-9870.

[361] Lafdi, K., Mesalhy, O., and Elgafy, A., "Merits of Employing Foam Encapsulated Phase Change Materials for Pulsed Power Electronics Cooling

Applications," *Journal of Electronic Packaging*, Vol. 130, No. 2, 2008. https://doi.org/10.1115/1.2912185, URL https://doi.org/10.1115/1.2912185.

[362] Li, W. Q., Guo, S. J., Tan, L., Liu, L. L., and Ao, W., "Heat transfer enhancement of nano-encapsulated phase change material (NEPCM) using metal foam for thermal energy storage," *International Journal of Heat and Mass Transfer*, Vol. 166, 2021, p. 120737. https://doi.org/10.1016/j.ijheatmasstransfer.2020.120737, URL https://www.sciencedirect.com/science/article/pii/S0017931020336735.

[363] Palomo Del Barrio, E., Dauvergne, J. L., and Morisson, V., "A Simple Experimental Method for Thermal Characterization of Shape-Stabilized Phase Change Materials," *Journal of Solar Energy Engineering*, Vol. 131, No. 4, 2009. https://doi.org/10.1115/1.3197838, URL https://doi.org/10.1115/1.3197838.

[364] Brousseau, P., and Lacroix, M., "Numerical simulation of a multi-layer latent heat thermal energy storage system," *International Journal of Energy Research*, Vol. 22, No. 1, 1998, pp. 1–15. https://doi.org/10.1002/(SICI)1099-114X(199801)22:1⟨1::AID-ER334⟩3.0.CO;2-L, URL https://onlinelibrary.wiley.com/doi/abs/10.1002/%28SICI%291099-114X%28199801%2922%3A1%3C1%3A%3AAID-ER334%3E3.0.CO%3B2-L, _eprint: https://onlinelibrary.wiley.com/doi/pdf/10.1002/%28SICI%291099-114X%28199801%2922%3A1%3C1%3A%3AAID-ER334%3E3.0.CO%3B2-L.

[365] Okada, M., "Characteristics of a Plate-Fin Heat Exchanger with Phase Change Materials," *Journal of Enhanced Heat Transfer*, Vol. 2, No. 4, 1995. https://doi.org/10.1615/JEnhHeatTransf.v2.i4.30, URL https://www.dl.begellhouse.com/journals/4c8f5faa331b09ea,7f83fab45ff69f39,05ab23a408232810.html, publisher: Begel House Inc.

[366] Majumdar, P., and Saidbakhsh, A., "A heat transfer model for phase change thermal energy storage," *Heat Recovery Systems and CHP*, Vol. 10, No. 5, 1990, pp. 457–468. https://doi.org/10.1016/0890-4332(90)90196-Q, URL https://www.sciencedirect.com/science/article/pii/089043329090196Q.

[367] Benkaddour, A., and Faraji, M., "Numerical Investigation of a Phase Change Material Building Integrating Solar Thermal Collector PCM-BST," *Journal of Thermal Science and Engineering Applications*, Vol. 14, No. 8, 2022. https://doi.org/10.1115/1.4053057, URL https://doi.org/10.1115/1.4053057.

[368] Merlin, K., Delaunay, D., Soto, J., and Traonvouez, L., "Heat transfer enhancement in latent heat thermal storage systems: Comparative study of different solutions and thermal contact investigation between the exchanger and the PCM," *Applied Energy*, Vol. 166, 2016, pp. 107–116. https://doi.org/10.1016/j.apenergy.2016.01.012, URL https://www.sciencedirect.com/science/article/pii/S0306261916000313.

[369] Bastida, H., Ugalde-Loo, C. E., Abeysekera, M., and Jenkins, N., "Dynamic modelling of ice-based thermal energy storage for cooling applications," *IET Energy Systems Integration*, Vol. 4, No. 3, 2022, pp. 317–334. https://doi.org/10.1049/esi2.12061, URL https://onlinelibrary.wiley.com/doi/10.1049/esi2.12061.

[370] Choi, Y.-H., Kim, C.-M., Jeong, H.-S., and Youn, J.-H., "Influence of Bed Temperature on Heat Shrinkage Shape Error in FDM Additive Manufacturing of the ABS-Engineering Plastic," *World Journal of Engineering and Technology*, Vol. 4, No. 3, 2016, pp. 186–192. https://doi.org/10.4236/wjet.2016.43D022, URL http://www.scirp.org/Journal/Paperabs.aspx?paperid=71339, number: 3 Publisher: Scientific Research Publishing.

[371] Zawaski, C., and Williams, C., "Design of a low-cost, high-temperature inverted build environment to enable desktop-scale additive manufacturing of performance polymers," *Additive Manufacturing*, Vol. 33, 2020, p. 101111. https://doi.org/10.1016/j.addma.2020.101111, URL https://www.sciencedirect.com/science/article/pii/S2214860419318184.

[372] Nawaz, K., Schmidt, S. J., and Jacobi, A. M., "Effect of catalyst used in the sol-gel process on the microstructure and adsorption/desorption performance of silica aerogels," *International Journal of Heat and Mass Transfer*, Vol. 74, 2014, pp. 25–34. https://doi.org/10.1016/j.ijheatmasstransfer.2014.03.003, URL http://www.scopus.com/inward/record.url?scp=84897080819&partnerID=8YFLogxK.

[373] Kakaç, S., Shah, R. K., and Aung, W., *Handbook of single-phase convective heat transfer*, J. Wiley and sons, New York Chichester Brisbane, 1987.